Optimization of Thermoelectric Chalcogenides

by

Mohamed Oudah

A thesis
presented to the University of Waterloo
in fulfillment of the
thesis requirement for the degree of
Master of Science
in
Chemistry-Nanotechnology

Waterloo, Ontario, Canada, 2014

Declaration

I hereby declare that I am the sole author of this thesis. This is a true copy of the thesis, including any required final revisions, as accepted by my examiners.

I understand that my thesis may be made electronically available to the public.

Mohamed Oudah

Acknowledgements

I want to begin by expressing my gratitude to my research supervisor, Prof. Holger Kleinke for his guidance, support, and encouragement throughout my studies at Waterloo. His passion for research is balanced with an equal passion for running, which results in a healthy lifestyle that truly inspired me. Based on the two 5 km races we ran in the 2013 and 2014 summers, we stand even where I got better time in the former and was beaten in the later. I was able to dive into the field of solid-state chemistry during my time at the Kleinke group, and have built a solid foundation for my future research endeavours.

I would like to thank my friend, and group crystallographer, Dr. Assoud for his support and valuable advice. I am very thankful to Katja for helping me stay positive throughout my research, and for her countless help with lab work. I am grateful for all my colleagues in the Kleinke lab, former and present, Nader Farahi, Nagaraj Nandihalli, Nhi Truong, Quansheng Guo, Rafay Shams, Mathew VanZant, Yixuan Shi, Parisa Jafarzadeh, Raj Sankar, and Suk-Kyung Jeung, for their friendship.

I want to thank Prof. Linda Nazar for her guidance and valuable advice during my time in Waterloo. I am grateful to Prof. Pavle Radovanovic for helping me improve my research skills.

I thank my parents and my sister for their love and support throughout my life. I express my gratitude to the friends that supported me throughout writing this thesis.

Mohamed Oudah

Abstract

Thermoelectric (TE) materials can convert heat into electricity when a temperature gradient is applied (Seebeck effect), and can pump heat from the cold end to the hot end using electricity (Peltier effect). These materials have shown improved properties in recent years, and promising bulk materials have been uncovered by many research groups. Chalcogenide containing materials are the leading TEs today, and examples uncovered by the Kleinke group include $Tl_4(Zr,Hf)Te_4$, $Ba_3Cu_{16-x}S_{11-y}Te_y$, and $BaCu_{6-x}(S,Se)Te_6$. Initial evaluation of cold-pressed pellets of these materials showed potential for TE application, with a high figure-of-merit, zT, which relates to the efficiency of a material in converting heat into electricity. This zT is a dimensionless figure composed of heat and electrical transport properties of a material through the equation: $zT = T\alpha^2\sigma\kappa^{-1}$, where α is the Seebeck coefficient, σ the electrical conductivity, and κ the thermal conductivity, measured at a specific temperature (T). A zT value above unity is desired for a bulk material to be used for power generation. The biggest challenge in optimizing TE materials is decoupling the properties contributing to zT, and tuning the properties in a way that improves the zT overall. In this work, it is demonstrated that the zT value for a material can be improved through doping and hot pressing to close to ideal density. Adding Nb to Tl_4ZrTe_4 improved the zT compared to the ternary sample by enhancing the electrical conductivity. The zT of the samples of nominal composition "$Tl_4ZrNb_{0.04}Te_4$" and $Tl_4Zr_{1.03}Te_4$ amounted to 0.064 and 0.042 at ~500 K, respectively. Properties of undoped Tl_4HfTe_4 were also compared to those of $Tl_4Zr_{1.03}Te_4$, and Tl_4HfTe_4 had a higher zT of 0.08 at ~480 K, which is however still too low for any application. Varying the x and y values in $Ba_3Cu_{16-x}S_{11-y}Te_y$ achieved the highest zT for $Ba_3Cu_{15.1}S_8Te_3$, amounting to 0.78 at ~780 K. However, after six repeat electrical property measurements, these samples showed color change, which was confirmed, via EDX measurement, to be the result of Cu atoms migrating across the material. In contrast, $BaCu_{6-x}(S,Se)Te_6$ showed great stability after repeat measurements, which is attributed to localized mobility of Cu atoms. The properties of $BaCu_{6-x}(S,Se)Te_6$ were measured, and zT values of 0.52 at 580 K and 0.81 at 600 K were obtained for $BaCu_{5.9}STe_6$ and $BaCu_{5.9}SeTe_6$, respectively.

"To make sense of the marvelous electronic properties of the solid state, chemists must learn the language of solid-state physics . . ."

~Roald Hoffmann~

Table of Contents

List of Figures

List of Equations

List of Tables

List of Abbreviations

Abbreviation	Meaning
Å	Angstrom ($1 \cdot 10^{-10}$ meters)
$a,\ b,\ c$	Crystallographic axes
$COHP$	Crystal orbital Hamilton population
C_p	Specific heat capacity
DOS	Density of states
DSC	Differential scanning calorimetry
EDX	Energy dispersive X-ray (spectroscopy)
E_F	Fermi energy
κ_e	Thermal conductivity – electronic contribution
κ_L	Thermal conductivity – lattice contribution
LMTO	Linear muffin-tin orbital (approximation)
PGEC	Phonon Glass Electron Crystal
p-XRD	Powder X-ray Diffraction
α	Seebeck coefficient
SEM	Scanning Electron Microscopy
σ	Electrical conductivity
TE	Thermoelectric
TG	Thermogravimetry
$\propto$	Proportional to
zT	Thermoelectric figure of merit

1 Fundamentals

The field of solid-state chemistry provides a unique perspective for understanding the synthesis and properties of solids. One of the fundamentals in this field is learning to relate bonding, structure, and properties. Understanding solids as a combination of these factors allows us to predict and tune materials for different applications as desired. Furthermore, one needs to extend into the field of solid-state physics to be able to paint a complete picture of solids and their properties. The focus of this report is on the synthesis, tuning, and characterization of materials for thermoelectric (TE) applications. While the synthesis relies solely on the chemistry of solids, the tuning and characterization involve combining ideas from physics and chemistry.

Thermoelectric (TE) materials convert heat to electricity in the presence of a temperature gradient, or, alternately, can produce a temperature gradient when placed in an electrical potential. These materials are used in solid-state electrical generators, and have potential for recovering energy in the form of waste heat from various sources,[1] including automobiles. Also, they have niche applications where stability and low maintenance are vital, as demonstrated by their use in NASA spacecrafts.[2] The combination of fossil fuel depletion and environment pollution concerns raises the need for reliable and environmentally friendly electric generators, and TE generators can play an important role in fulfilling this need. Another application for TE materials is in solid-state Peltier coolers,[3] that remove heat using only electricity, without moving parts, and without releasing toxic gases to the atmosphere. This report is focused on those materials that perform best in power generation; as a result, their properties are investigated in the typical operating temperature range, from room temperature up to 800 K.

1.1 Thermoelectric Effect

The three fundamental thermoelectric effects are the Seebeck, Peltier, and Thomson effects. The Seebeck effect was discovered in 1822 by Thomas Johann Seebeck, when he observed that heating one of two dissimilar conductors in a closed loop caused the deflection of a compass needle.[4] At the time, Seebeck mistakenly interpreted his observation as a magnetic effect, but his observation still holds as the first report of this effect. In 1834, physicist and meteorologist Jean Charles Athanase Peltier noticed that a temperature difference exists at the junction of two dissimilar conductors when a current moves through them.[5] Experimentally, Peltier demonstrated the freezing of water at one junction, and upon reversing the current flow, the melting of ice at the same junction. The Peltier effect was further investigated in 1838 by Lenz, who explained that, depending on direction of current flow, heat can be generated or absorbed at the junction. The Thomson effect, also known as Kelvin relation, relates the previous two effects, and was predicted and observed in 1851 by William Thomson.[6] This effect relates current passing through a non-isothermal homogeneous conductor with the heating or cooling within the conductor. This heating and cooling is explained by the movement of charge carriers, holes and/or electrons, through the conductor in response to a temperature gradient. These effects are described in equations that include various coefficients describing the performance of a material. One of these coefficients is the Seebeck coefficient, which is proportional to the potential difference across a material when subjected to a temperature gradient. The Seebeck coefficient appears in more complex parameters used for characterizing the TE performance of materials, including the dimensionless figure of merit, zT. This zT includes other properties that are commonly measured in the examination of materials in other fields, namely electrical and

thermal conductivity. Calculating zT for a material based on properties measured in the lab allows us to predict the efficiency of this material in thermoelectric application. The theory behind zT and equations relating to it are discussed in the next section.

1.2 Figure-of-Merit (zT) and Efficiency

The theoretical performance of a TE material is usually represented by its dimensionless figure of merit, zT, which arises in the derivation of conversion efficiency of a TE generator made of such a material.[7] The higher zT, the higher is the maximum efficiency of the TE generator, which can be seen in equation 1.1 below:

1.1 TE Generator Efficiency

$$\eta = \frac{T_H - T_C}{T_H} \cdot \frac{\sqrt{1+\overline{zT}}-1}{\sqrt{1+\overline{zT}}+\frac{T_C}{T_H}}$$

where η is the efficiency, while T_H and T_C are the temperatures of the hot and cold sides of a TE generator, respectively, as shown in Figure 1-1 below. It can be seen from equation 1.1, that a greater difference between T_H and T_C will also result in higher efficiency. The value of zT for a material can be calculated using equation 1.2 below:

1.2 Dimensionless Figure-of-Merit

$$zT = \frac{\alpha^2 \sigma}{\kappa} T$$

where α is the Seebeck coefficient, σ is the electrical conductivity, κ is the thermal conductivity, and T is the temperature. In derivation of the efficiency equation above (1.1), the temperature used for calculating zT is the average of the hot and cold side temperatures. zT for each material reaches a maximum at different temperatures, and one needs to consider the zT in the range of T_H to T_C of the device when considering a material for application.

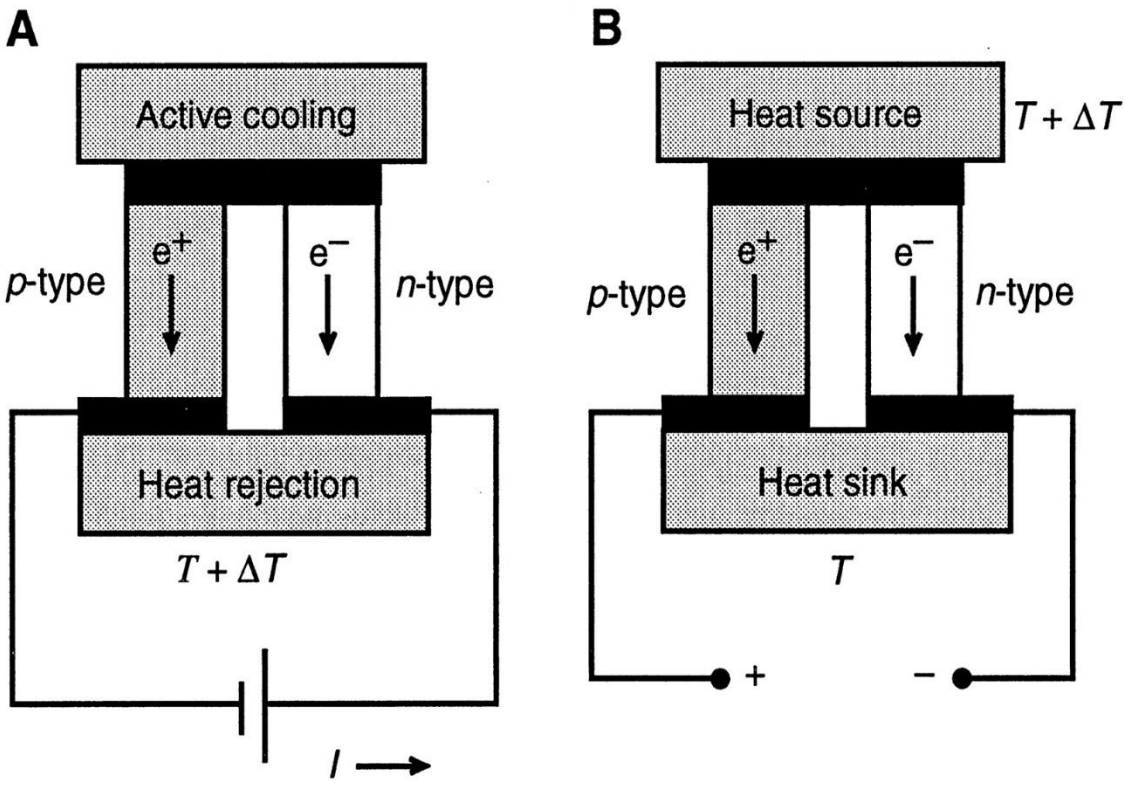

Figure 1-1 Set-up of *n*- and *p*-type thermoelectric materials in coolers (left, A) and power generators (right, B).[3]

It can be seen from equation 1.2 above that maximizing σ and α and minimizing κ would allow us to maximize zT. One factor that affects these parameters is the charge carrier concentration. The Seebeck coefficient for a material increases with decreasing carrier concentration, which

means insulating materials are favorable TEs. On the other hand, electrical conductivity increases with increasing carrier concentration, and can be described by equation 1.3 below:

1.3 Electrical Conductivity

$$\sigma = n\mu e$$

where *n* is carrier concentration, μ is the carrier mobility, and *e* is the carrier charge. The carrier mobility depends on various scattering mechanisms, which include scattering by ionized impurities and lattice vibrations. The relaxation time approximation of the Boltzmann equation for carrier mobility is shown below:[8]

1.4 Carrier Mobility

$$\mu = \frac{e\tau}{m^*}$$

where m^* is carrier effective mass, τ is the average relaxation time over all carrier energy levels, and *e* is carrier charge. The concentration of carriers and their effective mass are also related to the Seebeck coefficient in metals and degenerate semiconductors through equation 1.5 below:[9]

1.5 Seebeck coefficient (metals and degenerate semiconductors)

$$\alpha = \frac{8\pi^2 k_B^2}{3eh^2} m^* T \left(\frac{\pi}{3n}\right)^{2/3}$$

Metals have high carrier concentration, associated with high electrical conductivity (σ) and electronic contribution to the thermal conductivity (κ_e). Heat may also be transported through the material lattice via atomic vibrations (phonons), so that the total is:

1.6 Thermal Conductivity

$$\kappa_{tot} = \kappa_e + \kappa_L$$

where κ_{tot} is total thermal conductivity in a material, κ_L is the lattice contribution, and κ_e is the electronic contribution, which is proportional to the electrical conductivity and temperature according to equation 1.7 below:

1.7 Electronic Contribution to Thermal Conductivity

$$\kappa_e = L\sigma T$$

where L is the Lorenz number for a specific material. Substituting equation 1.7 into equation 1.2 for zT would result in electrical conductivity appearing in both the numerator and denominator, and this makes optimizing zT difficult. For semiconductors, the lattice component of thermal conductivity is often larger than the electronic one, and can be represented by the following equation:

1.8 Lattice Contribution to Thermal Conductivity

$$\kappa_L = \frac{1}{3}(C_v \nu_s \lambda_{ph})$$

where C_v is the heat capacity, v_s is the velocity of sound, and λ_{ph} is the phonon mean free path.[10]

The dependence of parameters appearing in equation 1.2 on carrier concentration is shown in Figure 1-2 below. Metals have high electrical conductivity, but are poor TE materials, because of their low Seebeck coefficient and high thermal conductivity. At low carrier concentration we have insulators, which are poor TE materials because of their low electrical conductivity. This leaves us with semiconductors as the materials to be used for TE applications, which can be concluded from the maximum power factor, $\alpha^2\sigma$, appearing in the semiconductor region. If we are able to reduce the thermal conductivity of a semiconducting material while keeping the power factor high, we will be able to increase the zT value.

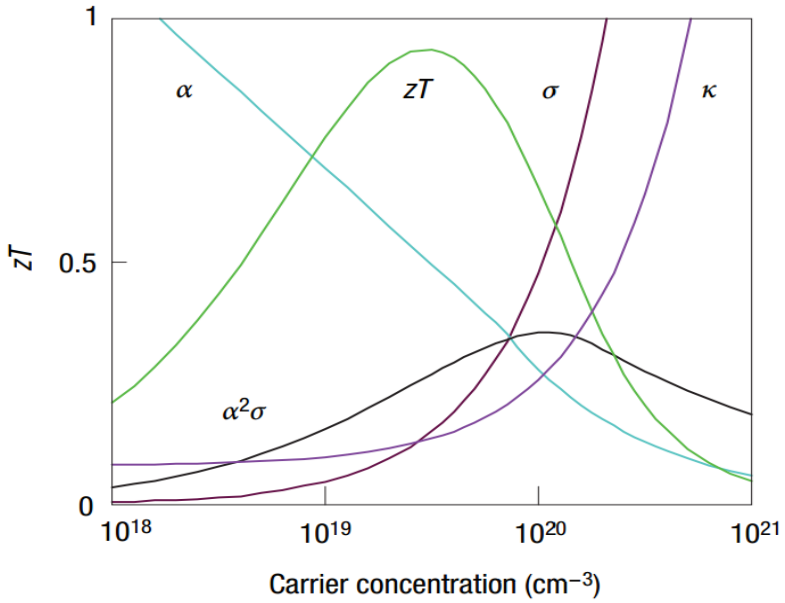

Figure 1-2 Parameters influencing zT plotted against carrier concentration.

The equations shown for the various transport properties are written in absolute charge carrier concentration and neglect the reality that in real materials two types of carriers, holes and

electrons, exist. Also, considering variations in transport properties along different crystal directions can be important when assessing properties of TE materials.

1.3 Material Requirements for Thermoelectric Application

Semiconductors, the materials of choice for TE application as explained above, can be doped with donors or acceptors to produce *n*-type and *p*-type materials, respectively. It is clear from Figure 1-1 that both types of material are required in order for TE devices to utilize the movement of both types of carriers, electrons and holes, for electricity generation and cooling purposes. The junction of *p*-type and *n*-type TE materials needs to be connected, electrically in series and thermally in parallel, such that the charge carriers move in the same direction with respect to the temperature gradient. The voltage across each junction is low, so a number of these junctions need to be connected in series to create a module, which can then be used in TE devices, as shown in Figure 1-3 below.

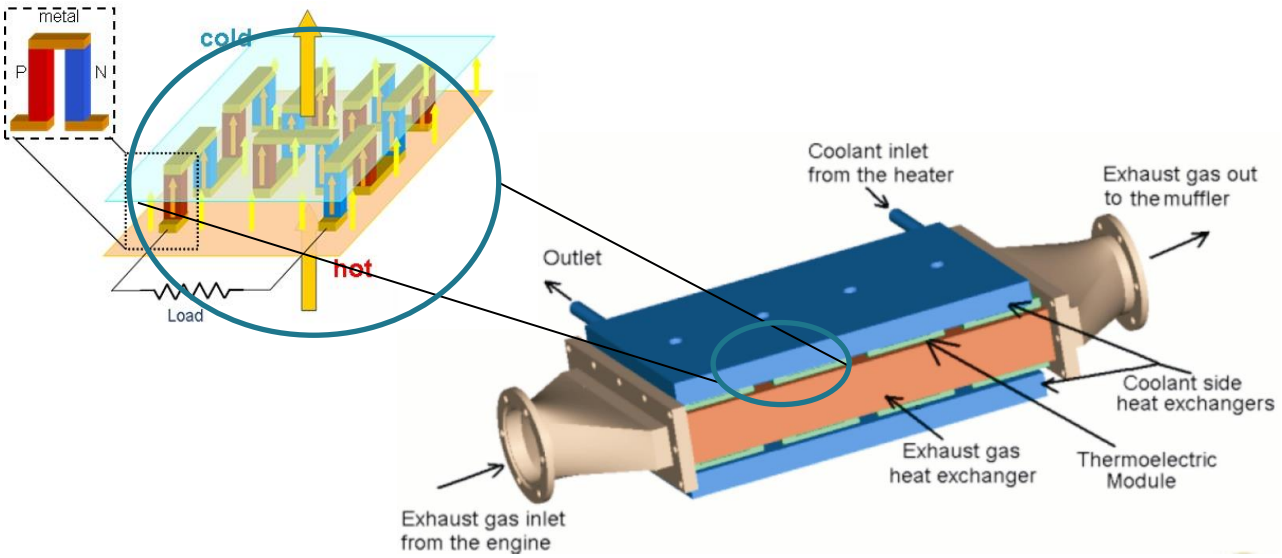

Figure 1-3 Schematic for TE generator to be used in recovering energy from automobiles.

[Dr. Jihui Yang, General Motors Research & Development Center]

Some materials can be tuned by doping into, both, *n*-type and *p*-type semiconductors, with favourable TE properties,[11] while others show favorable properties as an *n*-type[12] or a *p*-type[13] material. To be used in the same device, both, the *p*-type and *n*-type, materials need to have high zT at the operating temperatures of the device, so that the performance of one does not limit the other.

One of the commonly used models for a desirable TE material is that of a phonon glass and an electron crystal, or "PGEC."[14] This means that an ideal TE material needs to act as a crystal, with respect to electrons, and as a glass, with respect to phonons, at the same time. One should keep such a model in mind when looking for new, or simply tuning, TE materials.

The peak in power factor, as shown in Figure 1-2, is for materials with high carrier concentration, which is characteristic of highly doped semiconductors and metals. The Seebeck coefficient for metals and highly doped semiconductors is calculated using equation 1.5. Relating this to the power factor, which is proportional to the Seebeck coefficient squared, we conclude that maximizing the Seebeck coefficient by having high effective mass and low carrier concentration, within the semiconducting region, is what we really need in a TE material. Ionic compounds will give us high effective mass with low mobility, while semiconductors with small electronegativity differences have high mobility and low effective mass. The ideal situation is having high effective mass and high mobility, but this is extremely difficult to tune in a material. One has to compromise one for the other, and there are reports of compounds showing promising thermoelectric material at both ends of the spectrum. Chalcogenides (group 16

elements) and silicon-germanium show good TE properties, with the former exploiting high effective mass to achieve a high power factor and the later exploiting high carrier mobility.[9]

The optimal band gap for a thermoelectric material is greater than $6k_{\mathrm{B}}T$, and changes from one material to another depending on the mechanism of electron scattering.[15] The charge carrier concentration for such thermoelectric material is in the range of 10^{19}-10^{21} carriers/cm^3. The density of states (DOS) of a material describes the number of states available for electrons at each energy level. High complexity in the crystal structure usually contributes to lowering thermal conductivity, and usually introduces many peaks into the DOS. The Seebeck coefficient is proportional to the first derivative of the DOS around the respective energy level, so a large number of spikes around the Fermi level would contribute positively to the Seebeck coefficient,[2] as written below:

1.9 Relating Seebeck Coefficient to DOS

$$\alpha \propto \frac{1}{DOS(E)} \cdot \left. \frac{dDOS(E)}{dE} \right|_{E=E_{\mathrm{F}}}$$

The electrical conductivity is affected by the DOS around the Fermi level as well, and the larger the peaks, the greater the number of states that can be occupied by carriers in the material. This is represented with the equation below:

1.10 Relating Electrical Conductivity to DOS

$$\sigma \propto DOS(E)|_{E=E_{\mathrm{F}}}$$

Looking at the DOS gives us a different perspective that can help us in tuning a material towards the ideal PGEC model.

Typically, thermoelectric materials have a Seebeck coefficient in the range of 50 to 300 $\mu V \cdot K^{-1}$, while electrical conductivity ranges between 50 to 1000 $\Omega^{-1}cm^{-1}$. As for thermal conductivity, it normally varies between 1 to 3 $W \cdot m^{-1}K^{-1}$ for bulk thermoelectrics, with lower values found for nanostructured bulk materials.

1.4 State-of-the-Art Thermoelectrics

A variety of TE materials have been synthesized from elements across the periodic table exploiting different properties to achieve a high zT. Figure 1-4 shows the zT of state-of-the-art TE materials plotted against temperature. Bismuth telluride is well suited for room temperature applications, while lead telluride is useful for moderately high temperatures, and silicon-germanium is useful for devices operating at high temperatures.

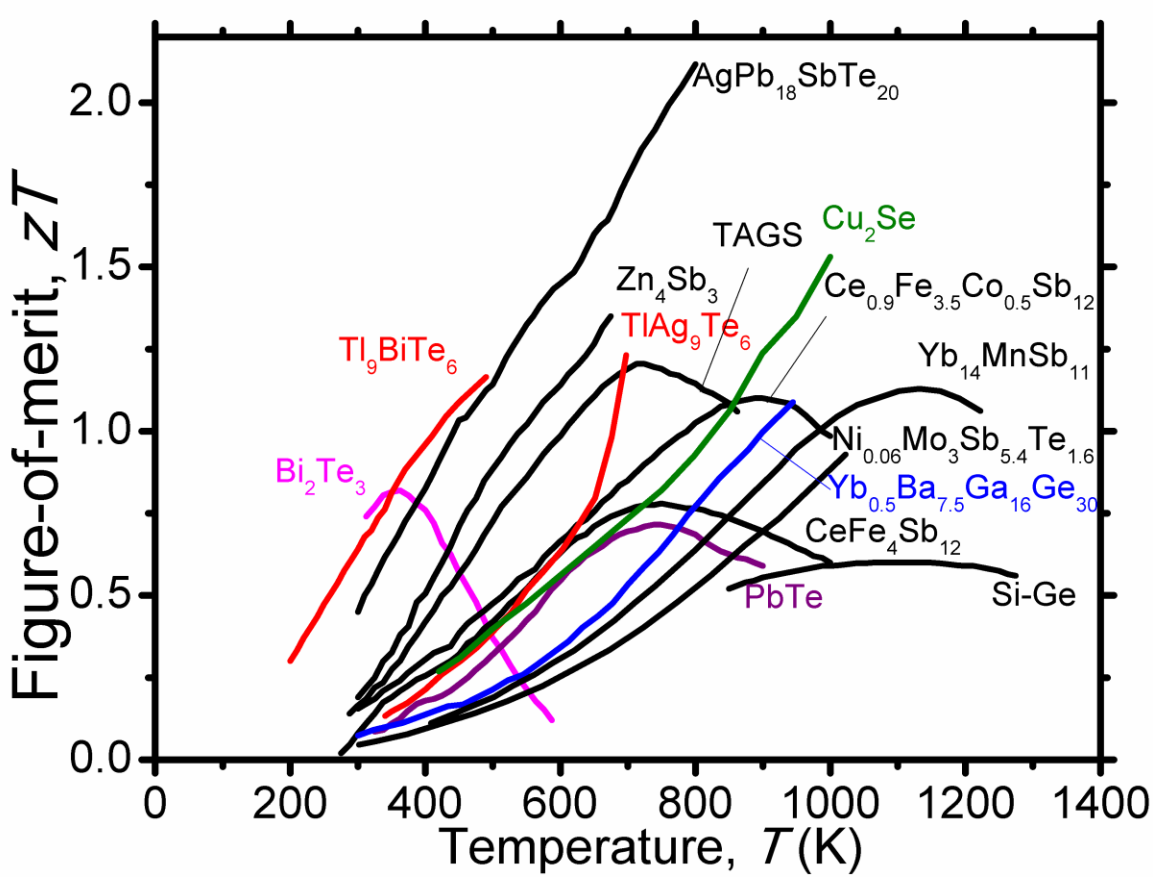

Figure 1-4 zT for state-of-the-art bulk TE material vs. temperature[16-22]

Designing an effective thermoelectric material requires us to maximize the power factor, $\alpha^2\sigma$, and to minimize the thermal conductivity, κ. Decoupling these parameters is a daunting task,

and various strategies are proposed in literature for tuning the properties of a material in a controlled fashion. Shown below, in Table 1.1, are the zT values of well-known compounds found in literature:

Table 1-1 zT for State-of-the-art Bulk TE Materials

Compound Name	Chemical Formula	Max zT @ Temperature (K)	Reference
Bismuth Telluride	**$Bi_2Te_{2.7}Se_{0.3}$**	**1.04 @ 400**	[23]
Lead Telluride	**PbTe**	**0.8 @ 773**	[24]
TAGS-85	$(AgSbTe_2)_{0.15}(GeTe)_{0.85}$	1.4 @ 750	[25]
Cs-Bismuth Telluride	$CsBi_4Te_6$	0.85 @255	[26]
Clathrate-I	**$Ba_8Ga_{16}Ge_{30}$**	**1.35 @ 900***	[27]
Sn-Thallium Telluride	$Tl_{8.05}Sn_{1.95}Te_6$	1.26 @ 685	[28]
Pb-Thallium Telluride	$Tl_{8.1}Pb_{1.90}Te_6$	1.46 @ 685	[28]
La-Skutterudite	**$LaFe_3CoSb_{12}$**	**1.40 @ 1000****	[29]
LAST	$AgPb_mSbTe_{2+m}$	1.7 @ 700	[30]
SALT	$NaPb_mSbTe_{2+m}$	1.6 @ 675	[31]
Bi-Thallium Telluride	**Tl_9BiTe_6**	**1.2 @ 500****	[21]
Ag-Thallium Telluride	**Ag_9TlTe_6**	**1.2 @ 700**	[22]
LASTT	$Ag(Sn,Pb)_mSbTe_{2+m}$	1.4 @ 700	[32]
Zinc Antimonide	β-Zn_4Sb_3	1.3 @ 660	[33]
Copper Selenide	**β-Cu_2Se**	**1.5 @ 1000**	[20]
Silicon-Germanium	$Si_{1-x}Ge_x$	0.9 @ 900	[34]
Tetrahedrite	$Cu_{12-x}Zn_xSb_4S_{13}$	0.8 @700	[35]
Mo-Antimonide	$Ni_{0.06}Mo_3Sb_{5.4}Te_{1.6}$	0.93 @ 1023	[36]

* Measured on single crystal **Extrapolated beyond the measured data

The properties of some of these materials, along with the strategies used to increase their zT, will be discussed in more detail in sections 1.4.1-5 below. Looking into the characteristics that give each material its high zT helps in understanding the materials being studied in this research. It should be noted that, through doping alone, bulk materials have reached a zT of about 1.5 during the last ten years, as seen in skutterudites, copper selenide, and thallium tellurides.[20,29,37] Recently, high zT was achieved in tetrahedrite, $Cu_{12-x}Zn_xSb_4S_{13}$, which is a natural mineral found in abundance. The zT of 0.8 achieved in $Cu_{11}ZnSb_4S_{13}$ and $Cu_{10.5}Zn_{1.5}Sb_4S_{13}$ at

about ~700 K is a step forward towards high performance and low-cost TE materials. The value for zT can be improved beyond that of the classical crystalline bulk materials by reducing the grain size to nanometer-range, which reduces the thermal conductivity of a material.[38] Complex nanostructured compounds can be synthesized using molecular beam epitaxy (MBE) and electron beam evaporation, which include thin-films (2D-material) and quantum dots. zT values for these types of nanostructured materials have surpassed those of the bulk material, reaching a zT of over 2, but their applications are still limited due to their high cost.[10] Bulk nanostructured materials can be produced through ball-milling or quenching eutectic melts, and materials produced with these techniques have shown significant improvements in zT.[38] Silicon-germanium alloys have shown high decrease in thermal conductivity through ball-milling, with zT reaching 1.3 at 1173 K for this material.[39,40] The next sections focus on some of the most important TE materials in literature, and parallels are drawn with materials discussed in this thesis.

1.4.1 Bi_2Te_3

Bismuth Telluride, Bi_2Te_3, is one of the best studied thermoelectric materials, with work dating back to the 1950's, and is the most promising thermoelectric for room temperature application. Bi_2Te_3 crystalizes in a rhombohedral crystal structure with $R\bar{3}m$ symmetry, and its semiconducting behaviour can be adjusted by element doping. Doping with selenium in the tellurium site can produce n-type bismuth telluride, with the highest zT of 1.04 found for ball-milled $Bi_2Te_{2.7}Se_{0.3}$ after hot-pressing.[23] In comparison, p-type bismuth antimony telluride, $Bi_xSb_{2-x}Te_3$ achieved a zT of 1.3 for similarly prepared samples.[39] Looking at the properties of bismuth telluride in the 300 K – 400 K range, we find both types of bismuth telluride achieve a

peak absolute Seebeck coefficient of ~200 $\mu V \cdot K^{-1}$. Their electrical conductivity, on the other hand, is low on the order of 100 $\Omega^{-1}cm^{-1}$ – 50 $\Omega^{-1}cm^{-1}$. The thermal conductivity for this material varies between 1.4 $W \cdot m^{-1}K^{-1}$ – 2.5 $W \cdot m^{-1}K^{-1}$ for hot-pressed bulk samples, which can be lower in nanocrystalline samples approaching ~1.0 $W \cdot m^{-1}K^{-1}$ without significant change in the other key properties. Anisotropic behaviour in the electronic properties of bismuth telluride may result from the same underlying causes as unconventional behaviour observed in other TE materials (further discussed in Chapter 5). Such behaviour in Bi_2Te_3 has been studied, and proven, in samples where the crystal orientation has preferred orientation in pressed pellets. Comparing the properties measured along both directions, we also find variations in the electrical and thermal conductivity, with measurements perpendicular to the pressing direction having higher conductivity values.[23]

1.4.2 PbTe

Lead telluride, PbTe, is another high zT thermoelectric suitable for mid to high temperature application that has a zT of 0.8 at 800 K prior to any optimization. Lead telluride crystallizes in the rock salt structure with the cubic space group $Fm\bar{3}m$, which can be tuned, similar to Bi_2Te_3, into an *n*-type and *p*-type thermoelectric. Lead telluride is made up of the elements Pb and Te in the 2+ and 2– oxidation states, respectively. After partial substitution of Na^{1+} for Pb^{2+}, the number of holes increases (fewer electrons), hence producing *p*-type PbTe.[41] On the other hand, substituting I^{1-} for Te^{2-} can increase the number of electrons in the material and thus produce *n*-type PbTe.[42] The zT for both, *n*- and *p*-type, of bulk PbTe has reached a value of 1.4 at ~750 K. The Seebeck coefficient for PbTe increases with temperature, reaching ~250 – 300 $\mu V \cdot K^{-1}$ at 750 K, while the electrical conductivity decreases with temperature and reaches ~300 $\Omega^{-1}cm^{-1}$

at 750 K. The thermal conductivity is lower than 1 $W \cdot m^{-1}K^{-1}$ at elevated temperatures, which, combined with the high power factor, gives PbTe its high zT. This material has been successfully used for producing electricity with high reliability using the Radioisotope Thermoelectric Generator developed by NASA.[43]

1.4.3 Clathrates/Skutterudites

Clathrates have attracted a lot of attention in recent years for their potential in thermoelectric application, mainly due to their unique structure. Clathrates of type I are made-up of a cage-like host structure, comprised of a combination of 24-atom tetrakaidecahedra and 20-atom dodecahedra, which trap a guest atom. This guest atom is typically smaller than the cage size, which allows for "rattling" within the cage. Typically, inorganic type I clathrates form in the cubic space group $Pm\bar{3}n$,[44] and have a stoichiometry of $A_8T_{16}R_{30}$ (e.g., *A* = Sr, Ba; *T* = Al, Ga; *R* = Si, Ge). These clathrates are narrow band-gap semiconductors, and their properties can be enhanced by manipulating the electrons around the Fermi level through introducing different guest atoms and cage-vacancies. Thermal conductivity in these compounds is low due to the rattling of guest atoms inside the oversized cages and is typically less than 2 $W \cdot m^{-1}K^{-1}$. Clathrates are an ideal example of a PGEC, because they have a narrow band gap varying between 0.2 – 0.6 eV, which, combined with high mobility of electrons through the cages, gives these compounds an electrical conductivity in the order of 1000 $\Omega^{-1}cm^{-1}$. Figure 1-5 (a) shows the crystal structure of a clathrate, namely $Ba_8Ga_{16}Si_{30}$.

Another family of related compounds is termed skutterudites, which are named after Skutterud, Norway, where the discovery of the aristotype $CoAs_3$ was made. The aristotype crystallizes in a

cubic structure with the space group $\bar{3}$, and, similar to clathrates, skutterudites form complex cage structures with many Sb–Sb interactions. Such Sb-Sb interactions are found in $LaFe_4Sb_{12}$,[45] shown in Figure 1-5 (b), and β-Zn_4Sb_3,[46] and both have shown promising thermoelectric properties. In contrast to clathrates, skutterudites have strong guest-host coupling that prevents any rattling effects, which gives these compounds phonon-crystal-electron-crystal behaviour rather than the PGEC.[2,47] Despite their behaviour as "phonon crystal", skutterudites can be promising thermoelectrics with some representatives achieving a zT higher than unity.

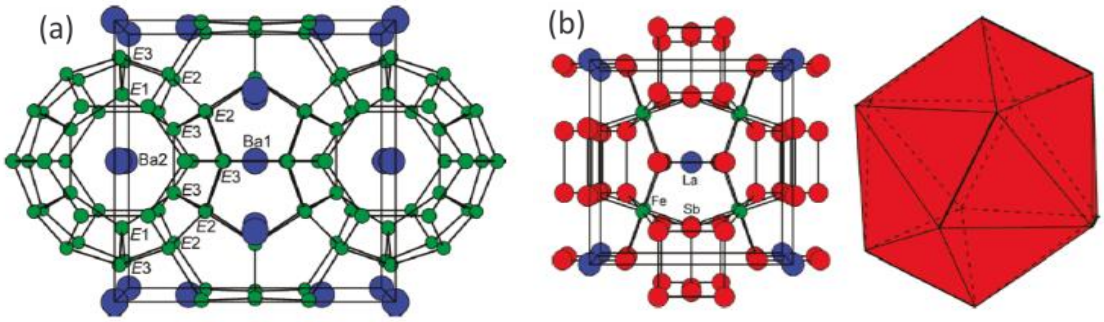

Figure 1-5 Unit cells for (a) Clathrate $Ba_8Ga_{16}Si_{30}$ (E = Ga, Si) (b) Skutterudite $LaFe_4Sb_{12}$ & $LaSb_{12}$ icosahedron[2]

1.4.4 Tl_9BiTe_6/$TlAg_9Te_6$

Heavy metal chalcogenides have shown promising TE properties with some materials achieving zT of around 1. Various thallium-containing TE materials have shown low lattice thermal conductivity. Tl_9BiTe_6 and Ag_9TlTe_5 have zT values of about 1.2 at 500 K[37] and 700 K[22,37], respectively. Tl_9BiTe_6 crystalizes in the tetragonal space group I4/mcm, and has a Seebeck coefficient of 400 $\mu V \cdot K^{-1}$ at 500 K, and the electrical conductivity reaches ~60 $\Omega^{-1}cm^{-1}$ at 500 K. On the other hand Ag_9TlTe_5 has a rhombohedral structure with the space group $R\bar{3}c$, and the Seebeck coefficient reaches a minimum of ~270 $\mu V \cdot K^{-1}$ at 650 K and climbs up to 320 $\mu V \cdot K^{-1}$ at

700 K. The electrical conductivity is on the order of about 10 $\Omega^{-1}cm^{-1}$ – 40 $\Omega^{-1}cm^{-1}$, but combined with the high Seebeck coefficient, gives this material its high power factor. The thermal conductivity values for Tl_9BiTe_6 and Ag_9TlTe_5 are ~0.39 $W \cdot m^{-1}K^{-1}$ and ~0.25 $W \cdot m^{-1}K^{-1}$, respectively, which are exceptionally low and result in the high zT for these materials.

Thallium has a higher electronegativity than most other metals and has two lone electron pairs in its Tl^+ state, which gives thallium chalcogenide semiconductors their narrow band gap and complex structures[48]. The versatility of thallium in forming both Tl^+ and Tl^{3+} allows for many different phases by modifying the binary thallium tellurides. Looking at the structure for Tl_5Te_3, we can see that tellurium atoms are surrounded by only thallium atoms, suggesting a Te^{2-} oxidation state for all tellurium atoms. To balance the charge in the compound, we must think of Tl_5Te_3 as $Tl_{10}Te_6$, with the complete charge formula having the form $(Tl^+)_8$**$(Tl^+)(Tl^{3+})$**$(Te^{2-})_6$. The two bolded thallium atoms can be thought of as two Tl atoms having an average oxidation state of 2+. Thinking of thallium telluride as such rationalizes the substitution of a pair of atoms with an oxidation state of 2+ per atom for a pair of thallium atoms, such as is the case in forming Tl_4PbTe_3 and Tl_4SnTe_3.[37] Another possibility is to substitute an atom with a 3+ oxidation state for one Tl atom, such as the case in Tl_9BiTe_6 and Tl_9SbTe_6.[37] Seeing the possibility for Tl and Te to form various structures as reported in literature, the Kleinke group was motivated to search for new ternary compounds containing these heavy elements.

1.4.4.1Motivation for $Tl_4(Zr,Hf)Te_4$

Exploration for new phases in Group IV-Tl-Chalcogenides led to the discovery of a number of new materials such as Tl_2MTe_3[49] and Tl_4MTe_4[48] with *M* = Zr, Hf. Studies of Tl_4ZrTe_4 and Tl_4HfTe_4

revealed a complex structure belonging to the $R\bar{3}$ space group, shown in Figure 1-5. Analysis of a single crystal of Tl_4ZrTe_4 has revealed the potential for doping, and cold-pressed bulk samples have a reported zT of 0.16 at 420 K prior to any optimization[48]. Although Hf doping in Tl_4HfTe_4 was not possible, the vacancy in the *M*3 position still exists, and this provides a chance for doping with other, smaller, elements. The possibility for doping, the complex structure, and the heavy atoms found in these thallium tellurides makes them ideal candidates for investigation of improvement of their thermoelectric properties. This is further discussed in Chapter 5.

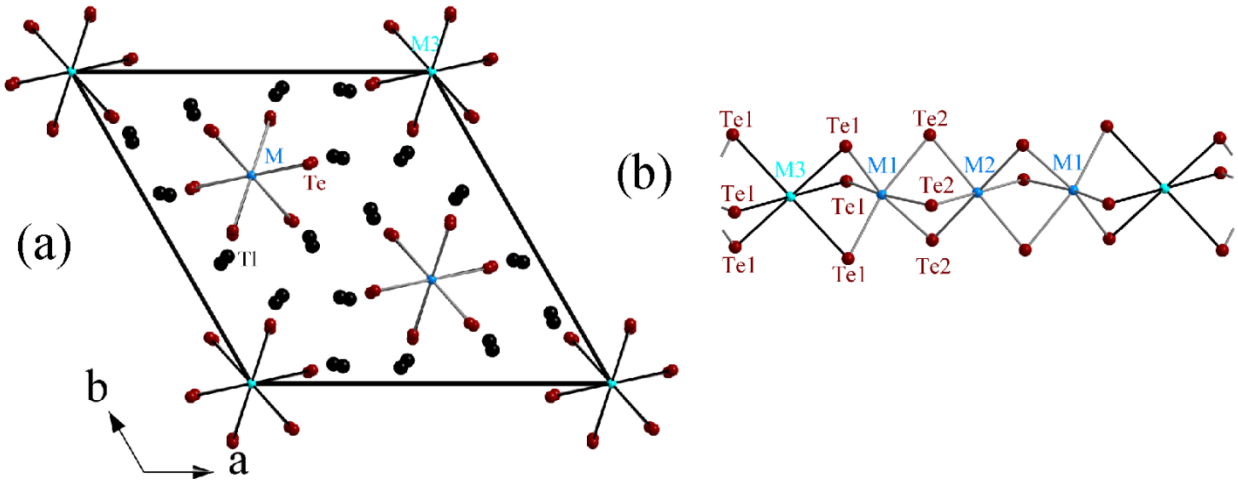

Figure 1-6 Tl_4ZrTe_4 crystal structure c-plane view (left) and $ZrTe_6$ Octahedra along c-axis (right) [Tl: Yellow, Zr: Green, Te: Blue]

1.4.5 Cu_2Se

Copper selenide, Cu_2Se, has shown exceptional properties for thermoelectric application in its high temperature phase. Cu_2Se has a monoclinic structure, α-phase, which transforms into an anti-fluorite structure, β-phase, upon heating to 420 K. The β-Cu_2Se has the selenium atoms forming an FCC lattice, while the Cu ions are able to freely move through vacancies. This high

mobility for the Cu-ions is described as “liquid-like” mobility, which is supported by the specific heat reaching values well below those expected for solid Cu_2Se at high temperature. The Seebeck coefficient for this material goes up with temperature and reaches 300 $\mu V \cdot K^{-1}$ at 1000 K, while the electrical conductivity is of the order of 100 – 1000 $\Omega^{-1}cm^{-1}$. The thermal conductivity is exceptionally low at 1000 K with a value of 0.7 $W \cdot m^{-1}K^{-1}$. The combination of these properties gives this material a zT of 1.5 at 1000 K.[20] However, the high copper ion mobility allows for the movement of Cu ions across the material when placed in a temperature gradient. This ultimately results in the material breaking down as illustrated in Figures 1-7 a, b, and c.[50] The color change across the bar shown in (a) is due to the migration of copper, (b) shows the optical image of the surface, and (c) shows copper nanowires forming at that surface.

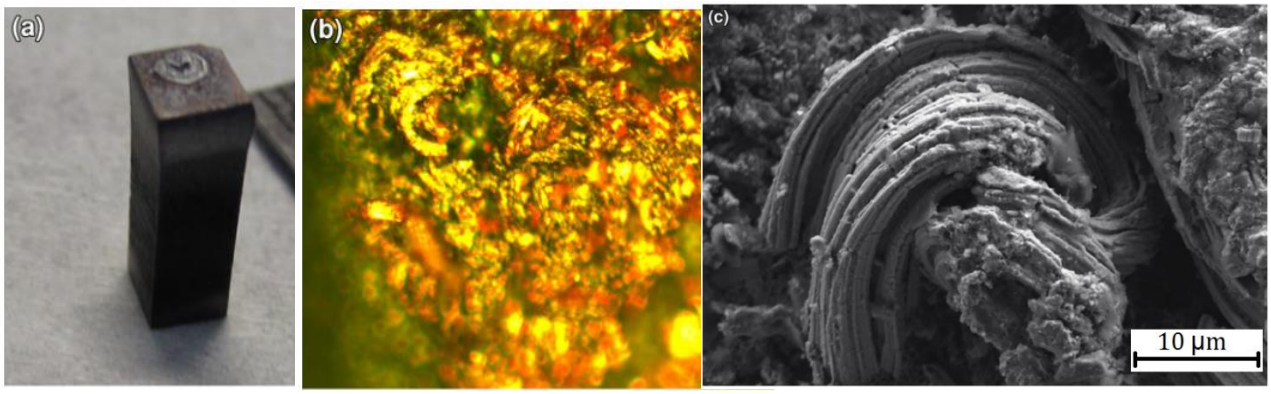

Figure 1-7 (a) Cu_2Se bar after heat cycling (b) optimal microscope image (c) Cu nanowire SEM

1.4.5.1 Motivation for $Ba_3Cu_{16-x}S_{11-y}Te_y$

Various barium copper chalcogenides were uncovered in the Kleinke group, such as $Ba_3Cu_{16-x}S_{11-y}Te_y$, which is discussed in this thesis (Chapter 6). The motivation for working on these compounds is to exploit the favourable thermoelectric properties reported for copper chalcogenides, while introducing large cations in the structure to hinder the movement of copper. Two barium copper chalcogenide structures are investigated in this report, these were

chosen based on properties measured for cold-pressed pellets and expected stability of the material.[51,52] The properties of $BaCu_6STe_6$ and $BaCu_6SeTe_6$ were investigated first, and they showed good thermoelectric properties and high stability (details are discussed in the next section). For this reason, we decided to test the properties of another barium copper chalcogenide uncovered by the Kleinke group to show the contrast in properties and stability. $Ba_3Cu_{16-x}S_{11-y}Te_y$ is isostructural to $Ba_3Cu_{16-x}Se_{11-y}Te_y$ with a rhombohedral structure when more S than Te is used, as shown in Figure 1-8 (a).[51] The properties for cold-pressed pellets show a Seebeck coefficient of ~200 $\mu V \cdot K^{-1}$ and electrical conductivity that reaches ~150 $\Omega^{-1}cm^{-1}$ at 700 K. The power factor reaches 2.38 $\mu W \cdot cm^{-1}K^{-2}$ at 700 K for $Ba_3Cu_{16}S_9Te_2$, and it was reported that high Cu ion mobility should be expected due to the 3-D network highlighted in Figure 1-8 (b). Nonetheless, we chose to measure the properties of hot-pressed pellets of this compound and compare the properties with the promising $BaCu_{6-x}(S,Se)Te_6$ discussed in the next section.

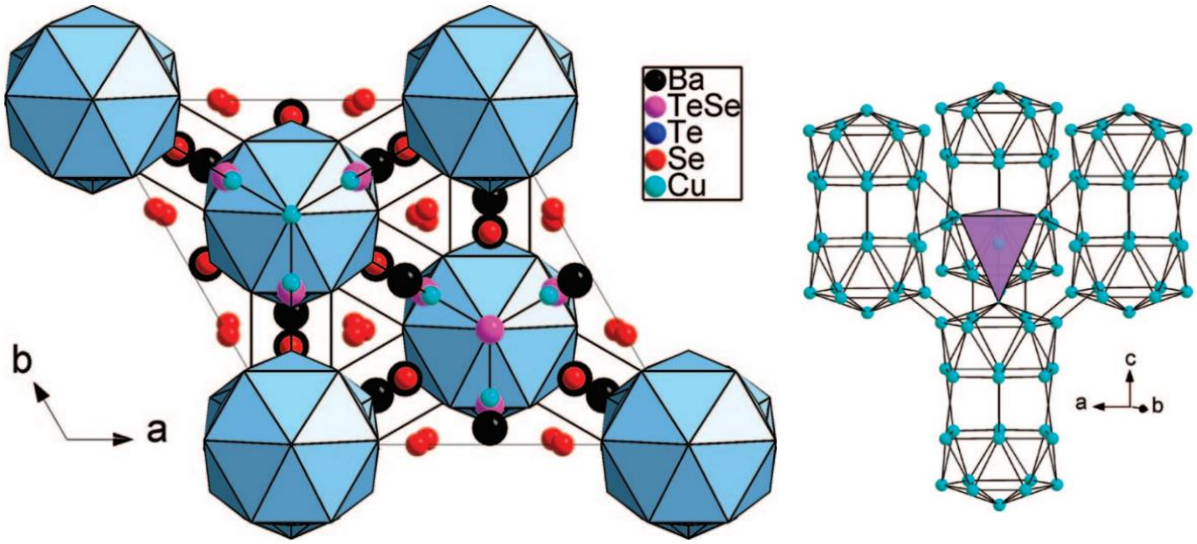

Figure 1-8 (a) $Ba_3Cu_{16-x}Se_{11-y}Te_y$ structure (c-plane) (b) Interconnected Cu_{26} polyhedra[53]

1.4.5.2 Motivation for $BaCu_{6-x}(S,Se)Te_6$

Other barium copper chalcogenides identified in the Kleinke group include $BaCu_6STe_6$ and $BaCu_6SeTe_6$, which are isostructural, and crystalize in the cubic space group $Pm\bar{3}$.[52] These compounds are different from Tl_4ZrTe_4, but offer other unique properties that can be exploited to increase zT. The crystal structure for these compounds is shown in Figure 1-9 below, with the selenium centered copper cubes emphasized. Tellurium in these compounds is found in $(Te_2)^{2-}$ pairs along the sides of the cubic unit cell, while it appears as Te^{2-} in the thallium compound. Barium in these compounds is situated within a Cu_8Te_{12} pentagonal dodecahedron as shown in Figure 1-9. Deficiency of copper is possible in this compound, which is rare for this type of cage structure.

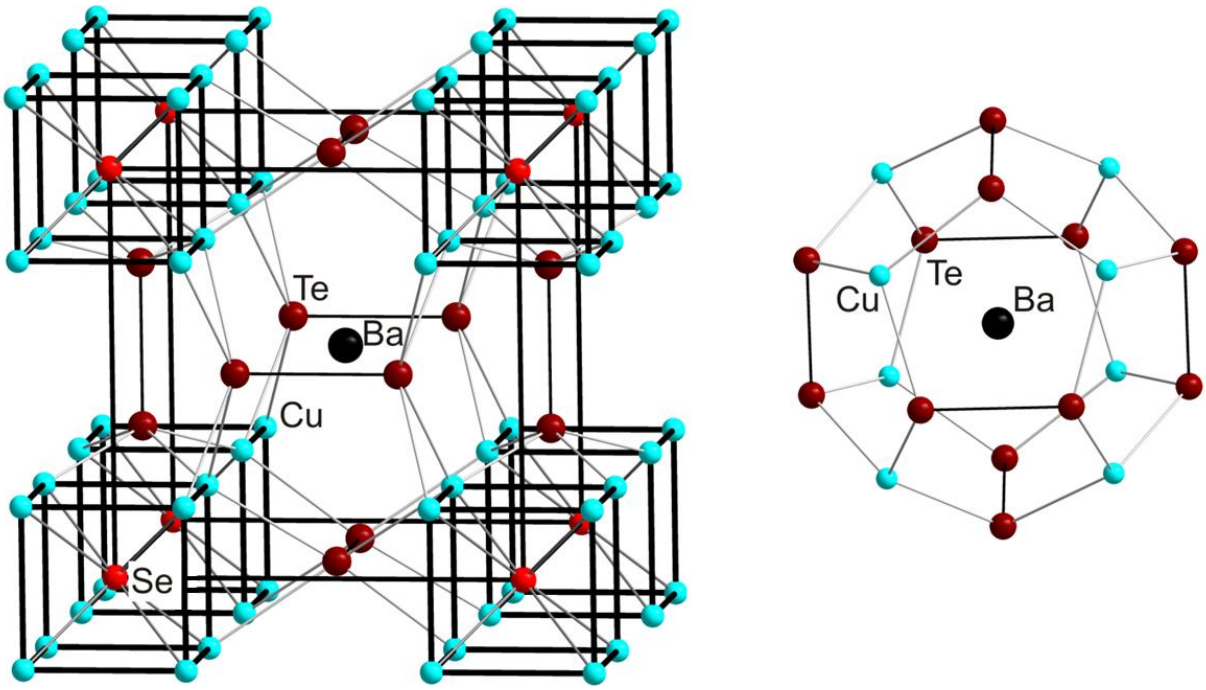

Figure 1-9 $BaCu_6SeTe_6$ crystal structure (left) and Ba-centered Cu_8Te_{12} pentagonal dodecahedron cage (right)

The charge balanced formula for this semiconducting material is $Ba^{2+}(Cu^{+})_6Se^{2-}(Te_2^{2-})_3$, which means that deficiency in copper would make this a *p*-type semiconductor, due to loss of electrons. Considering the selenium centered copper cubes and a copper deficiency of 25%, we can distribute six copper atoms at the corners of a cube in three symmetrically distinct ways. These three ways are shown in Figure 1-10 below, along with the resulting space group for the $BaCu_6SeTe_6$ crystal structure. Removing copper decreases the symmetry in the compounds, making it more complex, which contributes to the low thermal conductivity observed experimentally.[52] Copper selenide has shown potential as a TE with unique liquid-like copper ions,[20] and the same liquid-like behaviour is expected in these copper deficient compounds. However, greater stability is expected in these compounds, because of the localization of copper ion movement.

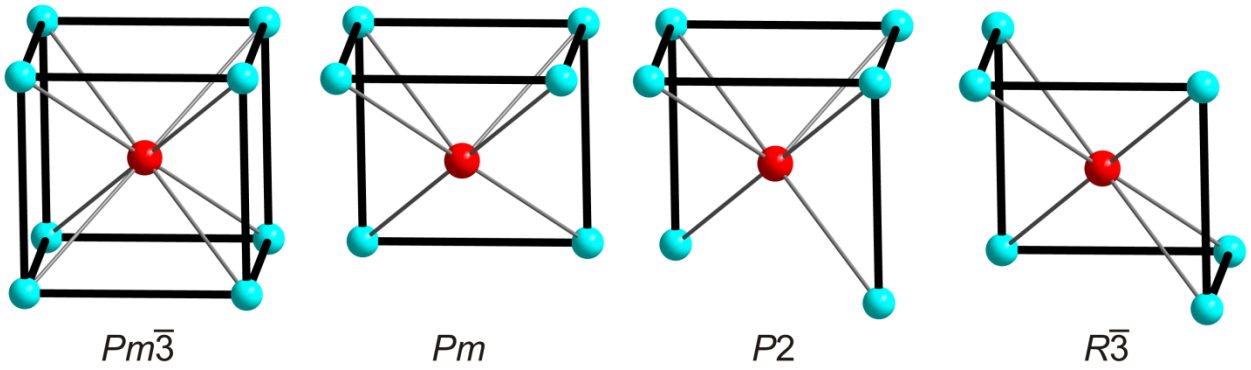

Figure 1-10 $SeCu_8$ cube (left) and three symmetrically distinct $SeCu_6$ polyhedra

2 Solid-State Chemistry and Physics

2.1 Crystal Structure and Symmetry

Materials discussed in this thesis are crystalline, so it is necessary to understand crystals and the mathematical symmetry operations used to classify them. A crystal can be defined as a solid material comprised of atoms, molecules, or ions arranged in a repeating and ordered fashion in three dimensions,[54] which can range in size, depending on growth time and technique, from nanometers to meters. The smallest 3-D unit of periodicity in a crystal is called the unit cell, with the unit cell axes a, b, and c, and angles of α, β, γ between the unit cell vectors $\vec{b}$ and $\vec{c}$, $\vec{a}$ and $\vec{c}$, and $\vec{a}$ and $\vec{b}$, respectively. There are nearly infinite combinations of patterns for atoms to pack in, but there exist only seven different crystal systems in which a unit cell can be classified (Table 2.1). Atomic positions are defined via their fractional coordinates (*x*, *y*, *z*), where a vector $\vec{r}$ points from the origin to the point (*x, y, z*) and $\vec{r} = x\vec{a} + y\vec{b} + z\vec{c}$. Each crystal system has one or more Bravais lattices (P, F, C, I) based on the atomic centering within the crystal. A primitive crystal has no unit cell centering, and is denoted P; when atoms are centered on every face such as (*x y z*); (*x*+½ *y*+½ *z*); (*x y*+½ *z*+½); (*x*+½ *y z*+½), we label it as F; in the case where only one face of the unit cell has centering, we consider it side-centered, C; lastly, when atoms at (*x y z*) have equivalent atoms at (*x*+½ *y*+½ *z*+½), we have an I, or body-centered, crystal. It should be noted that the space group for a rhombohedral unit cell can be written with an R. The seven crystal systems combined with the different centerings make up the 14 Bravais lattices in nature.

Table 2-1 Crystal systems and shapes.[55]

Bravais Lattice	Dimensions	Angles	Defining Directions
Cubic P, I, F	$a=b=c$	$\alpha=\beta=\gamma=90°$	[100][111][110]
Hexagonal P	$a=b\neq c$	$\alpha=\beta=90°$; $\gamma=120°$	[001][100][210]
Monoclinic P, C	$a\neq b\neq c$	$\alpha=\gamma=90°$; $\beta>90°$	[010]
Orthorhombic P, I, F, C	$a\neq b\neq c$	$\alpha=\beta=\gamma=90°$	[100][010][001]
Tetragonal P, I	$a=b\neq c$	$\alpha=\beta=\gamma=90°$	[001][100][110]
Triclinic P	$a\neq b\neq c$	$\alpha\neq\beta\neq\gamma$	–
Trigonal $P, (R)$	$a=b\neq c$	$\alpha=\beta=90°$; $\gamma=120°$	[001][100][210]

Crystals are described by symmetry operations, which include the ones that occur within the unit cell (point symmetry: mirror planes, rotations, inversion centres) and the ones that repeat infinitely in space (space symmetry: screw axes, glide planes, translations). These symmetry operations can be used to generate the closely-packed atoms that make up the crystal, and when repeated in three dimensions we form various crystal planes that can be used in defining a crystal system. Parallel crystallographic planes in reciprocal space can be defined using Miller indices. If a plane intersects a unit cell, the intersections along the three axes $\vec{a}$, $\vec{b}$ and $\vec{c}$ are noted. For example, in Figure 2-1 (a) we see planes running infinitely in the $\vec{y}$ and $\vec{z}$ directions and intersecting with the $\vec{a}$ at every one full unit cell, so the intersection coordinates are $(1\infty\infty)$. Taking the reciprocal of these values yields the Miller indices (100) – referring specifically to the middle plane in the diagram – or [100] for the generic lattice direction. Similarly, (110) would represent the diagonal plane in Figure 2-1 (b), which intersects the unit cell in the $\vec{x}$ and $\vec{y}$ directions, but not in the $\vec{z}$ direction. Finally, we have a case where a plane

intersects the $\vec{y}$ axis twice, at the half-cell and the full-cell, intersects $\vec{z}$ once, and never intersect the $\vec{x}$ axis, which would be called $(\frac{1}{\infty}, \frac{1}{(\frac{1}{2})}, \frac{1}{1})$ or the (021) plane.

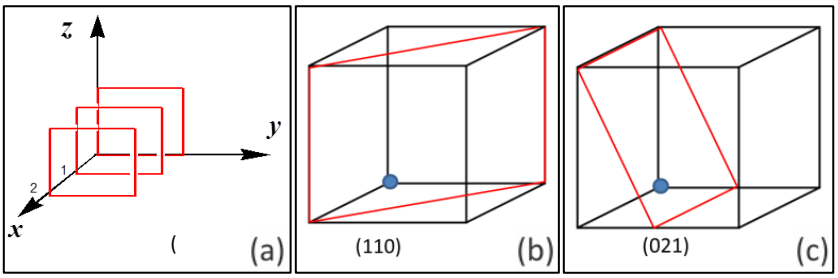

Figure 2-1 Miller Indices (a) (100) (b) (110) (c) (021)

Applying the various symmetry operations possible for the 14 Bravais lattices, we have the 230 possible space groups for all crystals. The rightmost column in Table 2-1 shows the crystal system's defining directions, which allow us to combine the crystal's setting $(P/F/I/C)$ with the appropriate symmetry operation symbol (i.e. *m*, *c*, 2_1, 4, etc.) to describe a crystal structure. For example, monoclinic $P2/m$ describes a primitive monoclinic system having a 2-fold axis parallel to the [010] direction and a mirror plane perpendicular to the [010] direction; orthorhombic $Cmmm$ therefore describes a side-centered unit cell having mirror planes (m) in the [100], [010], and [001] directions. Being familiar with space group notations can help in quickly assessing the atomic patterns expected in the unit cell without looking at the full structure.

2.2 Electronic Structure and Band Theory

The discovery of quantum mechanics in the early 1900s revolutionized the field of chemistry and gave us a better understanding of energies and shapes of atoms and electron distributions. Two key ideas that evolved from quantum mechanics are valence bond theory and molecular orbital theory,[56,57] which shaped our understanding of how molecules behave. Whereas discrete molecules have a defined shape and structure, crystalline solids extend into the infinite, while repeating atoms in a specific pattern. One way that chemists look at solids is by considering the Hückel diagrams for a series of ring molecules in increasing size as displayed in Figure 2-2. As the number of atoms in the ring increases and approaches infinity, the corresponding number of states increase and the gaps in energy between the levels decrease and eventually approaches zero. This leads to the formation of a continuous band describing the crystalline solid.

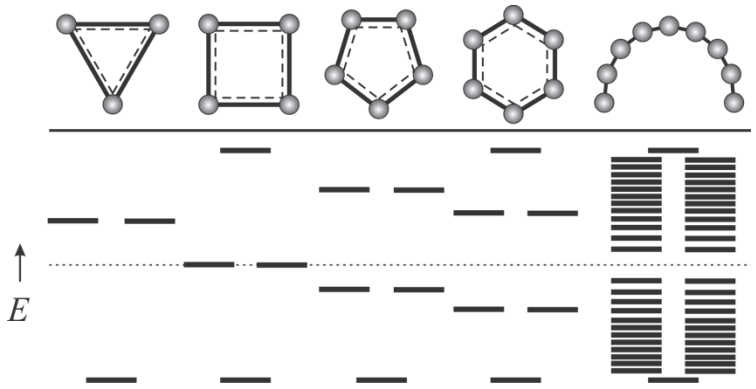

Figure 2-2 Orbital diagrams for increasingly large atomic rings.[58]

The energies of the states in such a bond are generally described by band theory, in which states are labelled according to their representation in reciprocal space. That is, by the wavevector, k. To visualize the concept of band theory, we can imagine the simplest case of a

linear chain of H atoms, and construct the bond state, or crystal orbitals, as a linear combination of H(1s) atomic orbitals, φ_n, centered at the nth site (Figure 2-3). In this case the Schrödinger equation is solved for Bloch functions, $\psi_k = \sum_n e^{ikna}\,\varphi_n$, where a is the spacing between atoms (i.e. lattice parameter) and where n=0, 1, 2, …,∞ represent each individual atomic orbital.[59] The wavevector, k, is related to the electron's direction of motion in the crystal, and has a value according to $k = \frac{2\pi}{\lambda} = \frac{2\pi p}{h}$, where λ is wavelength, *p* is momentum, and *h* is Planck's constant.[60] The lowest energy state ($E(k = 0)$) will be for the case where all orbitals are bonding, and this will be for the case where the wavefunctions describing each of the atoms are in phase for this chain of H(1s) orbitals. In the other extreme, if all atomic orbitals are out-of phase, we have the chain's highest energy state, ($E(k = {}^{\pi}/_{a})$), which represents the antibonding combination of orbitals. These two extremes are known as the first Brillouion zone, and k values are unique from $-\pi/a \leq k \leq \pi/a$, in this 1D-example. By calculating the intermediate energies for some k-points in between, we can construct the simple band diagram shown in Figure 2-3 (a).

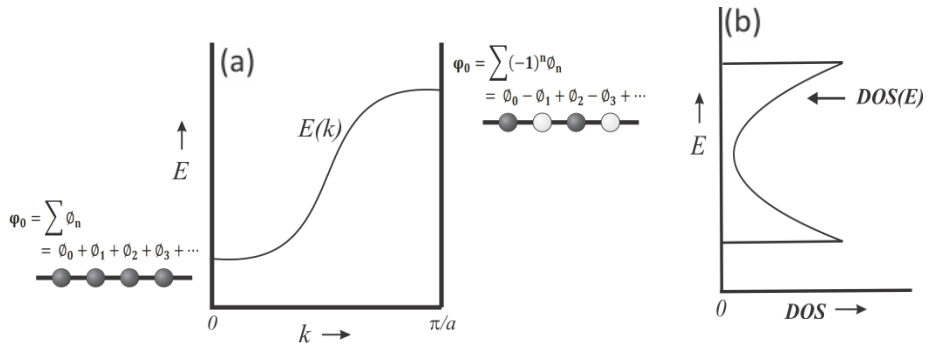

Figure 2-3 Theoretical hydrogen chain. (a) Band structure (b) *DOS.*[58]

The case mentioned above for the infinite chain of hydrogen atoms is the simplest possible, and as we have solids that extend in three dimensions, these diagrams become very complex. However, understanding the simple case for hydrogen can help us identify stable orbital contributions and their lattice direction ("uphill" or "downhill"). Along with the direction, we can evaluate the band width to identify the energy differences across the band. A perfectly flat band indicates that the energy difference between k points is zero, while a steep band means large differences in energy between k points and a change in bonding character.

One can also look at the density of states (DOS), shown in Figure 2-3 (b), which shows information from the band structures in a more compact manner. While bands can represent a nearly infinite number of orbitals, the density of states groups those orbitals into energy increments and sums up all orbitals at each level, thus the density of orbitals at each energy level. If we consider the first derivative of the bands to represent the DOS, we have $DOS(E)\,dE =$ number of energy levels between E and $(E + dE)$, so that the steepest bands contain the smallest number of orbitals and thus only contribute a small amount to the total DOS, and the flattest bands have the largest number of orbitals, thus a large contribution to the DOS.[61] As can be seen in Figure 2-4, the flatter bands at a specific energy correspond to a larger DOS at the same energy, and vice versa.

To create a slightly more complex situation than that of H atoms, we can extend an infinite chain of eclipsed square planar $Pt(CN)_4$ groups representing $K_2[Pt(CN)_4]$,[62] while using the same k points as in the previous case (i.e. Pt–Pt contacts (a-direction) of 3.3 Å). Now, if we consider

the different orbitals for Pt–Pt bonding, we can see that some will be bonding or antibonding at the k boundaries, 0 and $\pm\pi/a$, based on their in-phase/out-of-phase orientations.

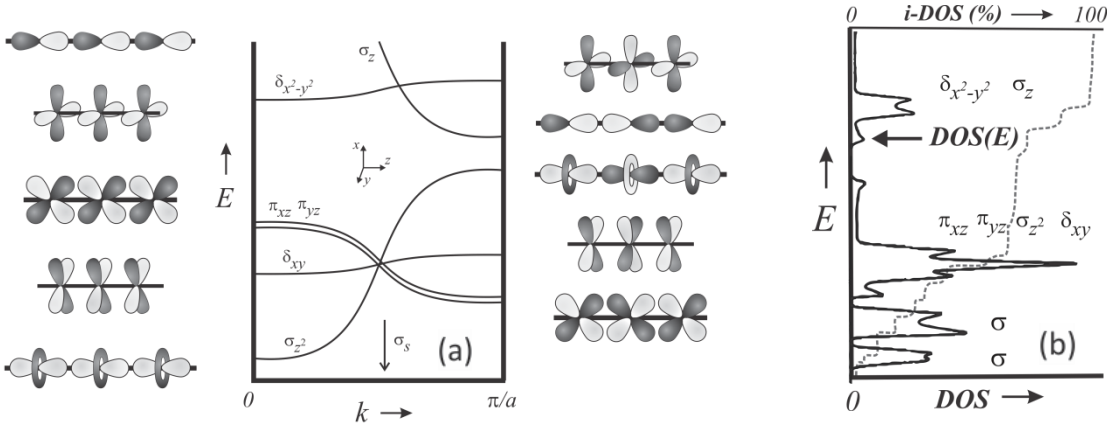

Figure 2-4 Eclipsed PtH_4 chain. (a) Band structure (b) DOS[58]

Many energy gaps may appear in the DOS, and the most interesting one for semiconductors is the one between the highest filled (valence) band and the bottom of the lowest empty (conduction) band, where it is expected to be less than 3 eV for semiconductors. Figure 2-4 shows the variations in band widths corresponding to the strength of bonding, σ vs. π vs. δ. The Fermi level is defined as the highest energy band containing electrons, and the DOS surrounding this energy level is of most interest when looking at band structures. By examining the vicinity of the Fermi level, we can describe the nature and predict the characteristic of a material, which allows us to decide on its potential application. The information provided by the DOS in Figure 2-4 (b) can quickly show us the contributing orbitals, as they correspond to the bands, and by examining the band gap size we can estimate the material's properties. Also, the location of the Fermi level, which can be in a gap, a steep DOS, or flat DOS, can provide important information, and we can see the contribution by each element or dopant to the DOS

at a specific energy level. Understanding this can help us make wise decisions about the choice of dopant in a material, and allows us to tune its properties in a controlled fashion.

Another useful plot is the Crystal Orbital Hamilton Population (*COHP*),[63] which is a variation on the DOS (Figure 2-5). The DOS only relates to the band-slope, so it does not provide information on bonding, non-bonding, or anti-bonding states. As such, we can separate the energy of bands into positive, negative, or zero overlap by multiplying the term for the DOS by the term in the Hamiltonian representing the overlap population. This results in a new DOS plot specific to the selected bonds, which will have the bonding character appear on the right side and the antibonding character on the left side, where more intense lines represent a stronger character.[64] The x-axis is plotted as "$-COHP$", since the Hamiltonian term is negative for the bonding state, and positive for the antibonding.

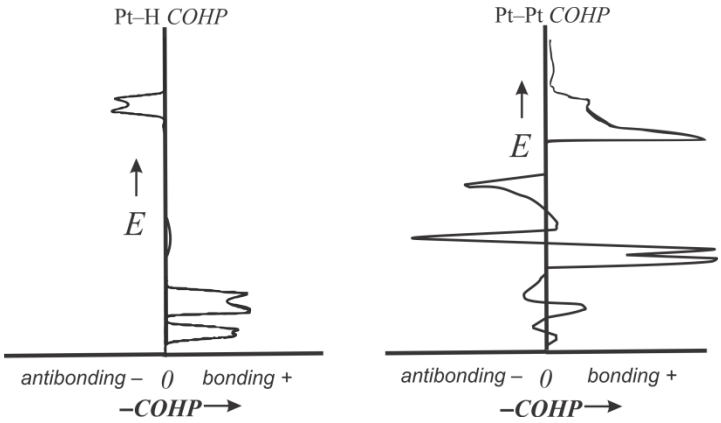

Figure 2-5 $COHP$ curves for PtH_4 chains (eclipsed)[58]

2.2.1WIEN2k

Band structures calculated for compounds presented in this report were done using the calculation package WIEN2k. This density functional theory (DFT) method solves the Kohn-Sham equation by utilizing the full-potential linearized augmented plane wave (LAPW) method for solving the Schrödinger equation.[23,24] The calculation requires a number of user inputs including: space group, lattice parameters, atomic positions, muffin-tin radii (R_{MT}) and number of k-points. The values for R_{MT}, which represent the smallest atomic sphere radius, were chosen for each atom in atomic units (a.u.). These were chosen so that the values are representative of the relative size of atoms, and R_{MT} of 2.5 was chosen for large atoms in calculations performed as part of this thesis. Also, the product $R_{MT} \times K_{Max}$ was set to a specific value, which limits the magnitude of the largest K vector used in the calculation. As for the number of k points, the initial calculation was started with only 30 k points, and then systematically increased until there was no observed change on the DOS. Below, the DOS of Tl_4ZrTe_4 resulting from different calculations are compared for different k-points used, namely, 30 k-points, 200 k-points, 1000 k-points, and 2000 k-points. It can be seen in Figure 2-6, that the smoothness of the curve changes between the first three calculations, but the DOS seems identical for the last two (1000 k-points and 2000 k-points). Convergence criteria were set at the start of each calculation, and this included the criteria for energy and charge. Typically, 10^{-4} Rydberg and 10^{-4} e were chosen as criteria for energy and charge, respectively.

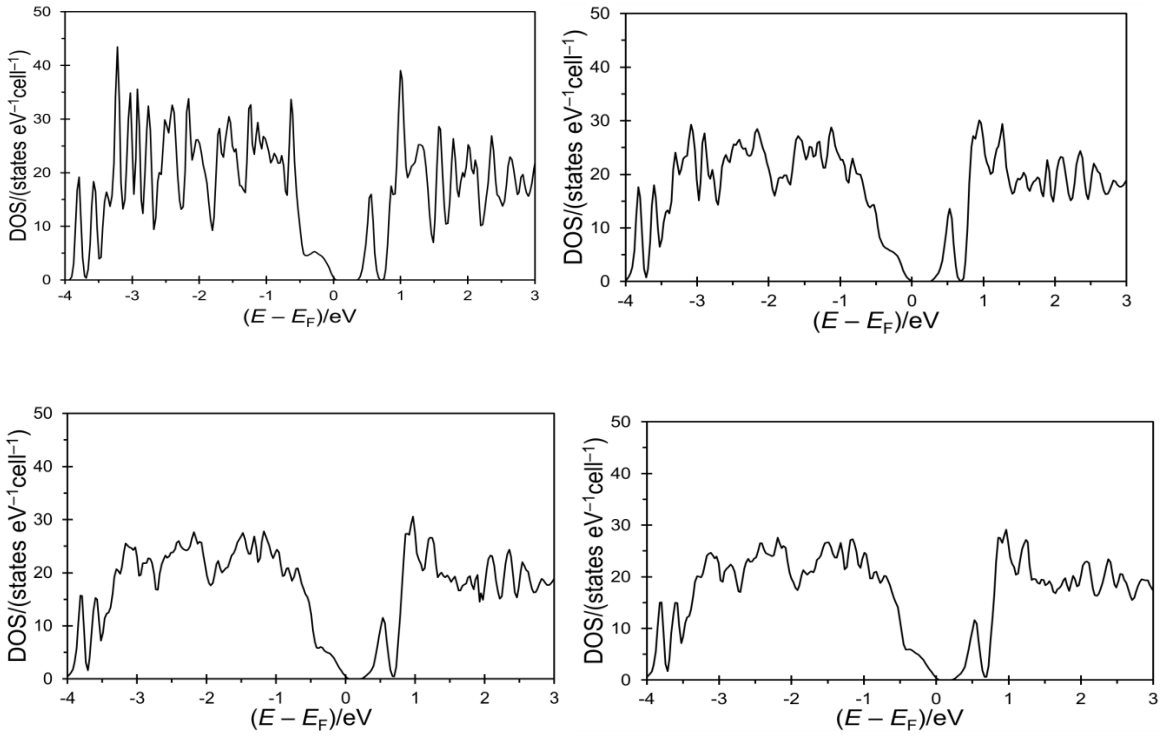

Figure 2-6 DOS plots for Tl4ZrTe4 with different number of k-points (30, 200, 1000, and 2000)

2.3 Doping and Charge Carrier Effects

The band gap in a semiconductor dictates its properties, and making minor changes to the band gap, we are able to manipulate the properties in a direction that improves its zT. One way of altering the position of the Fermi level, and hence the band gap, is through doping, which is defined as replacing some of the atoms in a crystal, typically 1 – 10%, with another that has a different electron count, but is similar in size and electronegativity. This usually affects the power factor, $\alpha^2\sigma$, by changing the number of charge carriers (illustrated in Figure 1-2). An intrinsic semiconductor can be changed into an extrinsic semiconductor through doping, which means extra energy levels are created within the band gap. These levels can be directly above the valence band, known as acceptor states, or directly below the conduction band, called

donor states.[60] Acceptor states are created when the element used for doping has fewer electrons than the original, and donor states are created when the dopant element has more electrons than the original (both cases are shown in Figure 2-6 (a)). This makes it possible to fine-tune the Fermi level of a semiconducting material.

The effects of various dopants on PbTe can be found in the literature. Particularly good properties were achieved after *p*-doping with Tl, presumably because of the occurrence of so-called resonance states stemming from the Tl-*s* orbitals. The DOS of Tl-PbTe shows a peak in the DOS just below the Fermi level, in contrast to Na-doped PbTe, which are shown as a solid-line and a dashed-line in Figure 2-7 A, respectively. The effect of this peak on the properties of PbTe is highlighted in Figure 2-7 B, where a great increase in zT above 550 K is seen resulting from 2% Tl doping in PbTe.

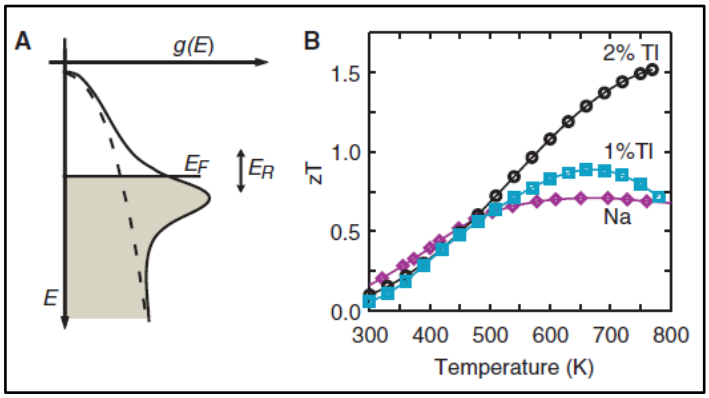

Figure 2-7 (A) Donor and acceptor states (B) Tl-PbTe DOS and resulting zT[65]

3 Syntheses

The development of solid-state compounds has attracted a lot of attention due to their various applications spanning a wide range of properties. As a result, numerous methods for synthesizing solids have been discussed in literature,[66] each with different starting materials and length of synthesis. The method used in synthesizing bulk samples reported in this thesis is the ceramic method. This method is used in industry and scientific laboratories to synthesize a wide range of materials including oxides, pnictides, nitrides, chalcogenides, intermetallics, and others. The properties presented in this report are measured for bulk samples with close to ideal density, which was achieved through hot-pressing. Factors that must be considered in going from the elements in their pure form to a dense pellet of the desired material include: starting material, reaction vessel, synthesis temperature, and hot-pressing conditions. Some considerations related to each step in the synthesis are discussed in sections 3.1-3.3.

3.1 Reaction Vessel, Starting Materials, and Equipment

Solid elements are weighed inside an argon-filled glove box according to stoichiometry and placed into a quartz tube. The solid elements used are typically of high purity >99%, and have various shapes that include, but are not limited to, powders, ingots, shavings, foils, granules, and rods. In the case where one of the elements did not melt during the synthesis, the surface area available for diffusion was considered. The ideal choice to maximize the surface area for diffusion is the powder form, ranging from 50 – 200 mesh[i]. However, fine powders tend to easily stick to various surfaces during the weighing process, which can cause deviation from the desired stoichiometry. Using starting elements in bigger chunks, we limited the surface area for

[i] Mesh refers to the size of sieve that powder can fall through. A larger mesh number corresponds to finer powder.

oxide contamination, which made these shapes desirable over the powder for certain elements. Also, for easily oxidized elements, a cleaning step was needed before using them in a synthesis, e.g by chemical transport or scraping off the surface of the starting material before placing it in the reaction vessel.

Where reaction with the tube surface was anticipated, the materials were placed into a graphite crucible, which was then placed inside the quartz tube, or carbon coating was applied on the inside of the quartz tube. The quartz tube was closed with vacuum-tight valves inside the glove-box, and then they were taken out of the glove-box and put under vacuum on a Schlenk line. The tubes were kept under vacuum until they reached a low pressure, of about 1.5 x 10^{-3} mbar, using an Edwards rotary oil pump (RV5 model) connected to an Edwards manometer. Then, the vacuum valves were closed, and the tubes were sealed using an oxygen-hydrogen torch. Programmable furnaces (Lindberg/Blue, 1373 K Box Furnace, BF51800 series) were used for the initial synthesis, because various heating and cooling rates were required depending on the melting points of reactants and products. The sealed tubes were placed inside the furnace, and the desired temperature profile was chosen (Detail in Section 3.2). After this step, the samples were usually hard solids, and they were ground, using an agate mortar and pestle, into fine powders. The powders were then analyzed via XRD to check for product formation, and were then placed back into a furnace for annealing, if needed. The latter was done using a manual furnace, if controlled heating and cooling rates were not required (Barnstead International, models: 1373 K FB1300 & FB1400).

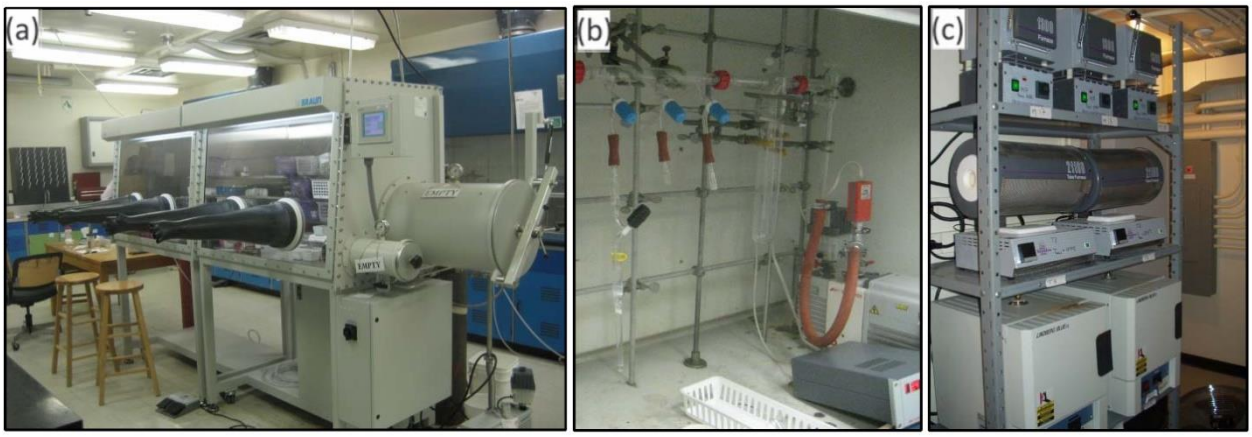

Figure 3-1 (a) Argon-filled glove box (b) Vacuum line (c) Manual furnace (top) Programmable furnace (bottom)

3.2 Phase Diagrams and Solid-State Reactions

The temperature profiles chosen for synthesizing compounds discussed in this report are all similar, and start by melting elements in a step-wise fashion. The tubes are heated to 50 degrees above the melting point of each element, and maintained at that temperature for a few hours. Considering the limits of the reaction vessel, silica's softening point in air of about 1,400 K, and the furnaces' maximum operating temperature of 1,323 K, we may not be able to melt all of the elements during the synthesis process. At the highest temperature, we may have a mixture of liquid and solid phases. It is important to consider the phases present during each step of the synthesis process, and the relative stability of side phases compared with the desired one. One example would be having an incongruent melting point, where, as we cool down the melted elements, we form solid phases with different stoichiometry than the melt; upon further cooling we would form the target phase, but other solid phases will also be present in the final product. To overcome this problem, we employ solid-state reactions, where the elements diffuse from one phase to another in the solid state, and eventually form the

most stable phase at that temperature for the specific stoichiometry of elements in the reaction vessel.

To have a successful solid-state reaction, adequate surface-surface contact and sufficient diffusion across the solids are needed (Figure 3-4 (a)). Solid-state reactions are usually used to improve the yield after initial synthesis and were utilized after grinding the products from the first synthesis into fine powder. These solid-state reactions are used in the main synthesis by keeping the furnace temperature at a high temperature, but below the melting point of the desired product, which helps us get a more homogenous product. Although the product is more stable than the reactants, these reactions are very slow at room temperature. The temperature for these reactions is chosen with Tammann's rule in mind, which suggests that a temperature around two-thirds of the melting point gives a good balance between significant reaction rate and limiting defects.[67] Solid-state synthesis has two key steps, where the first is nucleation (Figure 3-4 (a)), which refers to the desired phase forming at the solid-solid junction, and growth (Figure 3-4 (b)), which refers to the ions diffusing from the surface of the reactant to the surface of the product.[68]

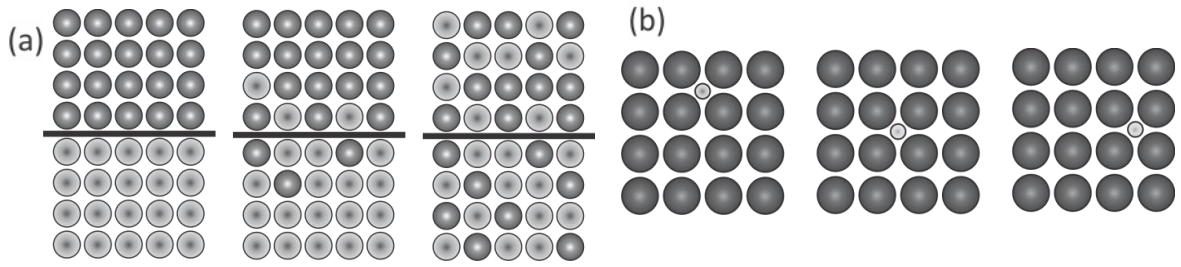

Figure 3-2 (a) Solid state diffusion process (b) Interstitial diffusion[58]

3.3 Hot-Pressed Pellets

To measure the various properties of our compounds, the ground powder of each sample was pressed into a pellet, and then measurements were done on this pellet. The density of this pellet can greatly influence the measured properties, and thus can change our zT value. Applying pressure alone, to make a pellet from powder, known as cold pressing, can produce pellets with up to 90% of the theoretical density, but this technique only works well for compounds with low melting points. To produce pellets with higher density, the powder should be heated to about 70% - 80% of the melting point, while pressure is being applied to it. This technique can produce pellets with 95-100% of the theoretical density, and is used for a wider range of materials. Accompanying the increase in density, the grain boundaries in the pellet will decrease in number, which decreases phonon scattering and increases the thermal conductivity. The electrical conductivity increases with hot-pressing due to the increase in mobility of carriers, because of the decreases in defects within the pellet. The Seebeck coefficient does not show significant change between hot-pressed and cold-pressed samples, but, overall, the zT value increases with hot-pressing. A comparison between hot-pressed and cold-pressed TE properties for various compounds is presented in Table 3-1 below.

Table 3-1 TE properties of various materials at 300K (Hot pressed material properties in bold)

Compound	σ ($\Omega^{-1}cm^{-1}$)	α ($\mu V \cdot K^{-1}$)	κ ($W \cdot m^{-1}K^{-1}$)	zT
$Re_3Ge_{0.6}As_{6.4}$	60 vs. **1090**	-88 vs. **-72**	1.5 vs. **4.2**	0.009 vs. **0.040**
$Ni_{0.06}Mo_3Sb_{5.4}Te_{1.6}$	110 vs. **1850**	75 vs. **65**	2.0 vs. **5.1**	0.009 vs. **0.046**
$In_{0.02}Pb_{0.98}Te$	20 vs. **172**	-178 vs. **-183**	1.3 vs. **1.3**	0.015 vs. **0.133**

*Unpublished results from the Kleinke group

4 Characterization Tools

Various characterization tools can be used to identify the structure and properties of the compounds synthesized. Tools used to access the purity of synthesized compounds are powder X-ray diffraction and energy dispersive X-ray spectroscopy, while differential scanning calorimetry can be used to identify phase transitions and melting points. Finally, the thermal and electrical transport properties can be measured using the thermal analysis and ZEM machines of the group.

4.1 Powder X-Ray Diffraction

Powder X-ray diffraction (XRD) is a technique used to study the crystal structure of a compound, and to determine its phase purity. X-rays are being generated in an X-ray tube by bombarding of a target (Cu in our case) with electrons. The rays emitted vary in intensity at different wavelengths, which depend on the target being used. A Ge single crystal is used as monochromator, to produce a monochromatic beam of X-rays that will be directed to hit our material, which is a polycrystalline sample composed of randomly oriented crystallites with sizes of the order of 1 μm – 500 μm. The X-ray will scatter from the electrons of the atoms in the material and will hit different positions on the detector. This scattering happens as a *Debye-Scherrer diffraction cone*, shown in Figure 4-1, named after the Dutch and Swiss physicists who first observed this in 1915. Initially, they surrounded their sample with photographic film to collect the positions for diffraction.

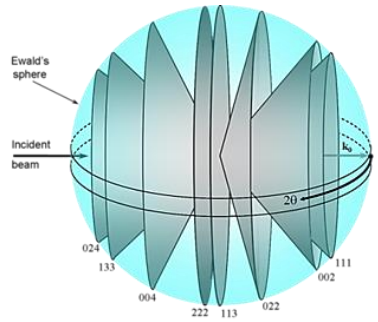

Figure 4-1 Debye-Scherrer powder diffraction cone.[69]

The film used will contain a series of lines with unique diffraction angles, 2θ, and intensity (I), which can be interpreted from the line thickness. Nowadays, detectors are typically used, instead of films, because they are more. The Ewald sphere shown in Figure 4-1 and 4-2 is a geometric representation of the interference condition, which relates to the diffraction planes in a crystal. The Ewald sphere is constructed with the centre being the origin in reciprocal space, and the radius is defined as $1/\lambda$. Shown in Figure 4-2, k_o is the incident radiation, while k_1 is the diffracted radiation, which is diffracted by a specific angle, 2θ.

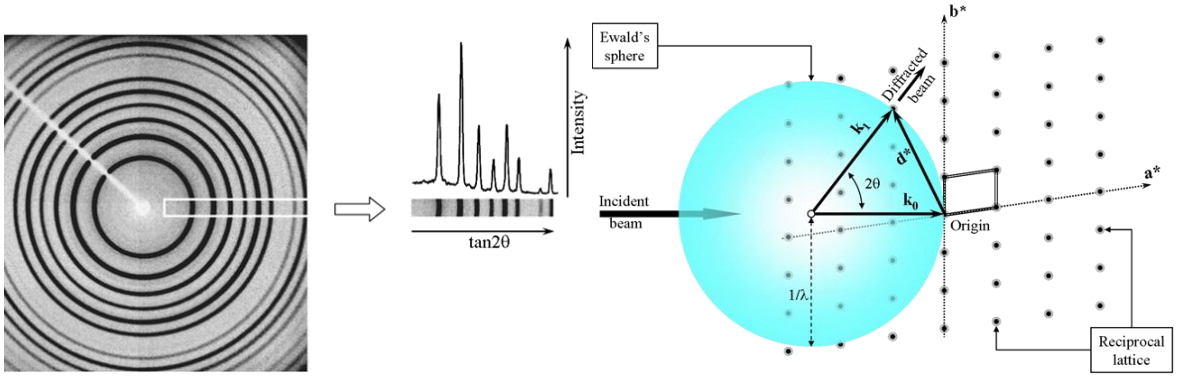

Figure 4-2 Ewald sphere: Origin of a powder diffractogram.[69]

The scattering of x-rays varies from one element to another and usually heavier elements will scatter x-rays more effectively. The difference in scattering power between different elements

allows us to identify the different elements in each crystal position, but the methods used for this are not discussed in this thesis. Thinking about diffraction in real space, it is possible to visualize the diffraction of X-rays hitting a crystal, such as in Figure 4-3 below, which shows the diffraction off of two adjacent planes, A and B.

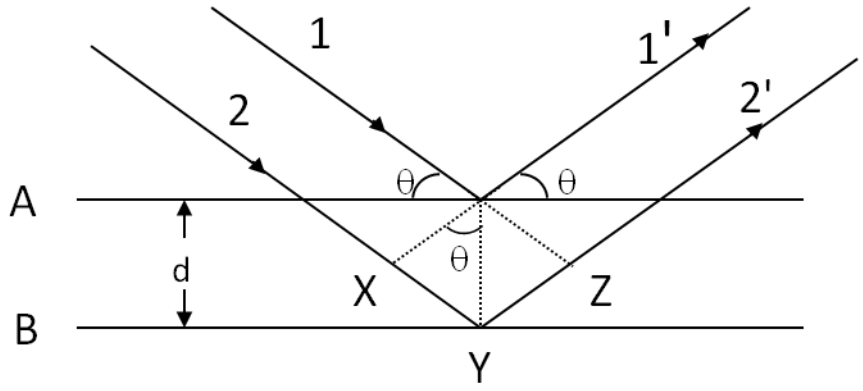

Figure 4-3 Diffraction of X-rays from parallel planes in a crystal.

Planes in a crystal are parallel with equal spacing, d, and at a certain angle, θ, the summation of XY and YZ shown in the figure will be an integer number multiple of the X-ray wavelength, and the scattered rays 1' and 2' will be in phase. These scattered X-rays will constructively interfere, which will be reflected in the intensity of X-rays detected at that angle. In using powder samples, we assume that crystals with all possible orientations exist and that the intensity varies with angle based on atomic distribution within each plane. However, in real measurements the observed scattered X-ray intensity may not match the expected pattern, which could be attributed to preferred orientations in the powder. It should be stressed that proper preparation of fine powders to be used in powder-XRD is essential to obtaining a meaningful diffraction pattern.

In preparation for data collection, the powder samples are placed on an Al-sample holder and flattened using a glass slide. The instrument used is an INEL powder diffractometer (Figure 4-4 (a)) with a position-sensitive detector (PSD). The radiation produced by the X-ray tube is reflected by a Ge single crystal through a slit, such that only Cu-$K_{\alpha 1}$ radiation reaches the sample. The sample holder is mounted in the center of the beam path, Figure 4-4 (b), and is being continuously rotated during the measurement. The Cu-$K_{\alpha 1}$ is generated in the X-ray tube on the right side, while the curved detector on the left collects diffracted radiation for 2θ angles up to 120°. Information from the detector will then be sent to a computer, where 2θ will be plotted on the x-axis, and the intensity of the peaks (I) on the y-axis.

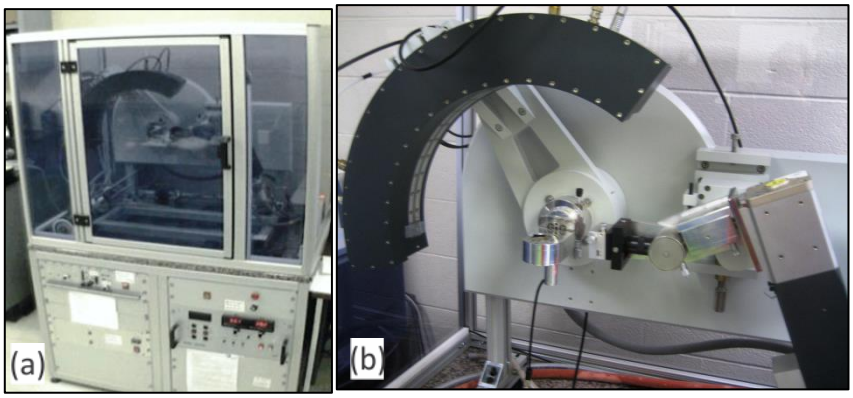

Figure 4-4 (a) INEL powder diffractometer. (b) Position sensitive detector (PSD).

4.2 Energy Dispersive X-Ray Diffraction

Energy dispersive X-ray (EDX) spectroscopy is used to determine the distribution of elements within a sample, which can be used to evaluate its homogeneity. A scanning electron microscope (SEM) is used in conjunction with this technique to observe the surface of the sample, and specific positions are chosen to be analyzed. A beam of high-energy electrons is directed at positions on the sample surface. These high energy electrons are able to eject electrons from the inner shells of the sample atoms. As a result, electrons from the outer shells fall down to the level of the ejected electrons and X-rays are emitted, proportional to the energy difference between the two shells. This difference in energy between shells is element specific, so we can identify the element depending on the wavelength of the X-ray emitted. The intensity of X-rays emitted at different wavelengths is proportional to the ratio of elements within the sample, and integrating the spectrum under expected peak positions will give us this ratio. There are overlaps in the frequency of X-rays emitted by different atoms, which means some peaks in the spectrum can be attributed to multiple atoms. This makes interpretation of the spectrum difficult at times, but using this technique, along-side other techniques, can provide valuable information about compounds. The machine used for EDX analysis by the Kleinke lab is the LEO 1530 FESEM equipped with an EDX Pegasus 1200 detector (Figure 4-5).

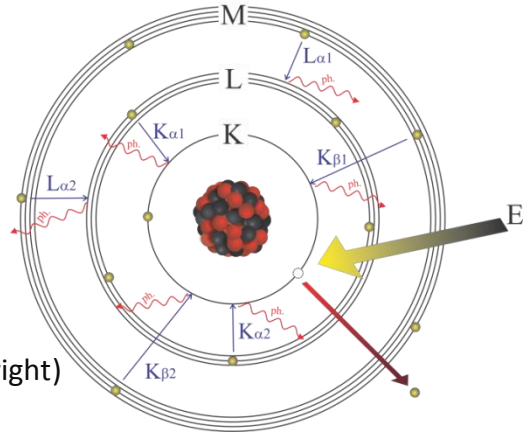

Figure 4-5 LEO 1530 FESEM (left) and Visual for EDX mechanism (right)

4.3 Differential Scanning Calorimetry

Differential Scanning Calorimetry (DSC) is a technique in which the heat-flow rate of the sample is monitored as a function of time or temperature. This technique allows us to detect physical and chemical changes in the sample, and a device was first developed by Watson and O'Neil in 1962.[70] For this technique, a reference with known heat capacity must be used, and the sample is measured relative to the reference.[71]

The specific instrument used in the Kleinke lab is a NETZSCH STA 409 PC Luxx, where measurements are usally done under a flow of argon (40 $mL \cdot min^{-1}$), and a heating rate of 5 – 20 $K \cdot min^{-1}$. The instrument measures phase changes (DSC) and mass changes (ThermoGravimetry), simultaneously. Flow rates of 50 and 80 $mL \cdot min^{-1}$ are used for argon in the balance and sample chambers, respectively. Typically, p-XRD is done on the samples after the measurement, to determine if any chemical changes occurred.

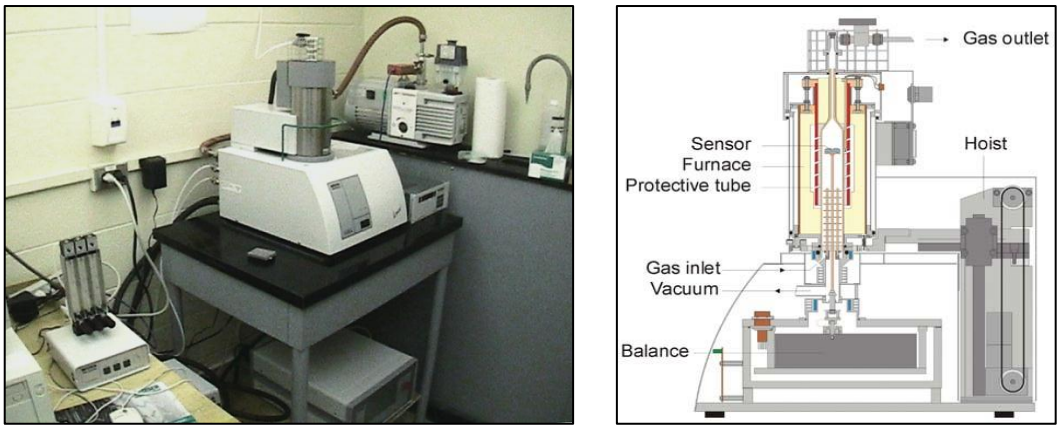

Figure 4-6 NETZSCH STA (left) and STA Schematic (right)[72]

Approximately 40 mg of powder sample is placed in an alumina or silica crucible, which is then placed on a silver sample holder, marked as sensor in Figure 4-7 (b). The reference, a sapphire

disk in this case, is also placed on the holder, and then the chamber is sealed and purged with regulated argon flow. The temperature of both sample and reference holders is measured as electrical voltage, using chromel thermocouples, and this temperature difference is converted into a heat-flow rate. The equation used is $\Phi = -k \cdot \Delta T$, where k is a constant specifically calibrated for the machine by NETZSCH. More specifically, this method is called Heat Flux DSC, which refers to having the sample and reference in the same furnace chamber, and connected by a low-resistance heat-flow path.[73] One set of thermocouples is used to monitor the difference between sample and reference crucibles, while another set measures the temperature of the furnace relative to the sensor. Also, the sample holder is balanced on a high-sensitivity scale (µg precision) that tracks the weight throughout the measurement, and provides complementary information for mass gain/loss on the same time/temperature scale.

As the measurement proceeds with constant argon flow, the heat flow reaches steady-state equilibrium and this is disturbed only by enthalpy changes in the sample, which produce a peak in the DSC curve.[74] An increase in the heat-flow rate will accompany an exothermic reaction (i.e. crystallization), while an endothermic reaction will decrease the flow rate (i.e. melting). Also, heat capacity (phase changes) can be detected from sudden drops in the baseline. The TG curve can be used to observe mass changes in the sample throughout the measurement, and it should be flat where mass change is not expected. The heat flow, Φ, is directly proportional to time (t), which is proportional to temperature. This allows us to plot DSC and TG curves against t or T as desired.[74]

4.4 Thermal Conductivity: Flash line 3000

The thermoelectric figure-of-merit, zT, includes the thermal conductivity, which shows up in the denominator, and has lattice and electronic contributions. In the Kleinke group, a Flash Line 3000 thermal diffusivity instrument is used to measure the diffusivity of samples, which utilizes the flash method under argon atmosphere. The diffusivity data can then be used to calculate thermal conductivity values for each sample (Figure 4-8 left). This method involves firing a laser at the sample, and has shown reproducible results over a wide temperature range, up to 1073 K.[75]

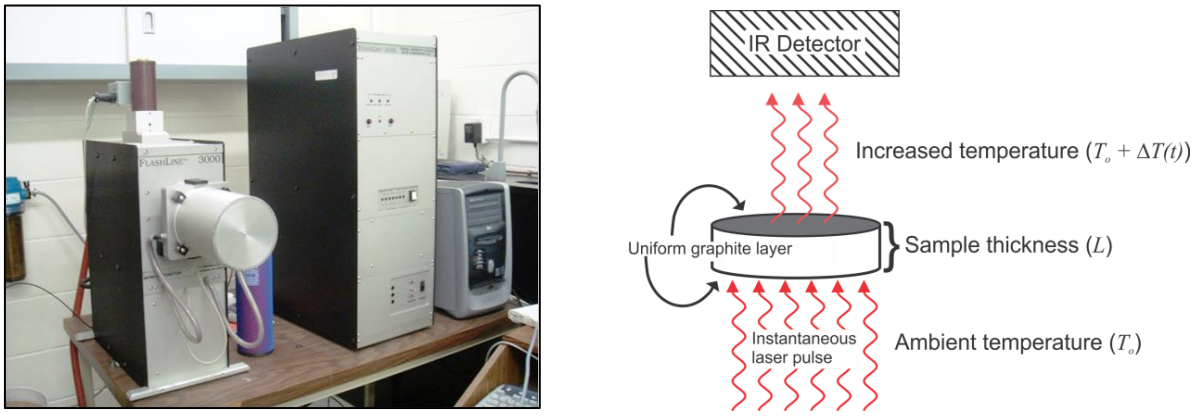

Figure 4-7 Flash Line 3000 (left) and Flash method (right)[58]

With this flash method, we can measure the thermal diffusivity values, D, at each desired temperature, which when combined with pellet density, ρ, and the material's specific heat, C_p, can give us κ as shown in Equation 4.2 (a). The density and specific heat are best determined experimentally, but this is not easily done. The pellet density, after hot-pressing, is measured using Archimedes' method, which depends on the weight of the pellet in air, and weight of the pellet in a fluid with known density according to the equation 4.1 below:

4.1 Archimedes' Method for Calculating Density

$$\rho = \frac{w_a - w_f}{w_a}\,\rho_f$$

where w_a is the weight in air, w_f is the apparent weight in fluid, and ρ_f is the density of fluid.

Ideally, the specific heat, C_p, is measured using a DSC, but the accuracy of the DSC setup in the Kleinke lab is insufficient for measuring the specific heat. The C_p is instead estimated as the average C_p for elements in the material based on the Dulong-Petit law (Equation 4.2(c)), with the gas constant, R, and average molar mass, M_{avg}. It is possible to estimate C_p more accurately, based on binary compounds that add up to the appropriate composition of the phase of interest (when available). Thermal diffusivity depends on sample thickness, L, and halftime, $t_{1/2}$, which is the time it takes for the opposite side to reach half of the maximum rise in temperature (Equation 4.2 (b)).

4.2 (a) Thermal conductivity (b) Thermal diffusivity (c) Specific heat capacity

$$\text{(a) } \kappa = D\rho C_{\text{p}} \qquad \text{(b) } D = 0.1388\frac{L^2}{t_{1/2}} \qquad \text{(c) } C_p = \frac{3R}{M_{\text{avg}}}$$

The samples are coated with graphite prior to the measurement, to ensure even heating across the entire surface, and placed on a sample holder with capacity for three samples with a diameter of 12.7 mm. The measurement setup starts with evacuating, followed by introducing an argon flow through the chamber; liquid nitrogen is used to cool down the InSb detector. The diffusivity is measured three times for each sample and temperature, and the average is used

for calculating the thermal conductivity. Comparing the measurements from the Kleinke group with other labs during a round-robin study, we can see that variations of $\pm$5% –10% are expected with this technique from one lab to the next.[76]

4.4.1 Lorenz Number Calculation

The electronic contribution to thermal conductivity can be calculated, using Wiedemann-Franz's law, from the electrical conductivity, Lorenz number, and temperature, as shown in equation 1.7. The temperature and electrical conductivity are experimentally measured, while the Lorenz number is estimated from the Seebeck coefficient. For semiconductors, the Lorenz number can range from 1.50×10^{-8} V^2 K^{-2} for intrinsic semiconductors to 2.44×10^{-8} V^2 K^{-2} for degenerate semiconductors.[77] Two methods were found in literature for estimating the Lorenz number, one is based on a Single Kane Band (SKB) model,[78] and the other is based on a Single Parabolic Band (SPB) model[79]. The method based on the SPB model requires only the Seebeck coefficient as input, while the method based on the SKB model requires other parameters, like temperature and band gap, for the calculation. The SKB-based method is more demanding than the SPB one, requiring longer calculation time, but the Lorenz numbers calculated from both methods were compared for several examples during this work, and these were within 99.9% of each other.

As such, the SPB was used for Lorenz number calculations presented in this thesis. The SPB model and the acoustic phonon scattering (λ = 0) assumption was used for Lorenz number calculations as follows:

4.3 SPB model: (a) Seebeck coefficient (b) Fermi integral (c) Lorenz Number

$$\text{(a)}\ \alpha = \frac{k_B}{e}\left\{\frac{(2+\lambda)F_{1+\lambda}(\eta)}{(1+\lambda)F_{\lambda}(\eta)} - \eta\right\} \qquad \text{(b)}\ F_j(\eta) = \int_0^{\infty} \frac{x^j}{1+e^{x-\eta}}\, dx$$

$$\text{(c)}\ L = \left(\frac{k_B}{e}\right)^2 \left\{\frac{(1+\lambda)(3+\lambda)F_{\lambda}(\eta)F_{2+\lambda}(\eta) - (2+\lambda)^2 F_{1+\lambda}^2(\eta)}{(1+\lambda)^2 F_{\lambda}^2(\eta)}\right\}$$

where α is the Seebeck coefficient, $F_j(\eta)$ is a Fermi integral of order j, η [= $E_F/(k_BT)$] is the reduced Fermi energy with E_F being the Fermi energy. The experimental α was used to calculate the value of η using equations 4.3 (a) and 4.3 (b) in the Maple 14 software. The value for η was then used to calculate the L corresponding to each α, and then the electrical conductivity at the same temperature was used to calculate the κ_e using Equation 1.7. Finally, the lattice contribution to the thermal conductivity, κ_L, was calculated from the difference between the measured κ_{tot} and the calculated κ_e.

4.5 Power Factor: ZEM-3 Instrument

The other components of the zT are the Seebeck coefficient and the electrical conductivity, which show up in the numerator as $\alpha^2\sigma$, also called the Power Factor (*P.F.*). In the Kleinke group, these two properties are measured using the ULVAC-RIKO ZEM-3 instrument, (Figure 4.8 (a)) simultaneously, over the desired temperature range. To avoid machine contamination from melts or vapours, materials are measured up to 100 K below their melting point.

In preparation for a ZEM measurement, a bar between 6 mm and 10 mm length is cut from the pellet used for thermal diffusivity measurement, which is then polished using sand paper (600-1000 grit) to ensure smoothness of the surface. A four probe method is used for our ZEM measurements; conceptual representation of the instrument's setup, with four points of contact, is shown in Figure 4-8 (b), where the separation between the horizontal probes (V_2 & V_3) can be 3, 5, or 8 mm as desired. The bar dimensions were measured using a Vernier calliper, while the exact separation between the probes was measured using a digital microscopic camera.

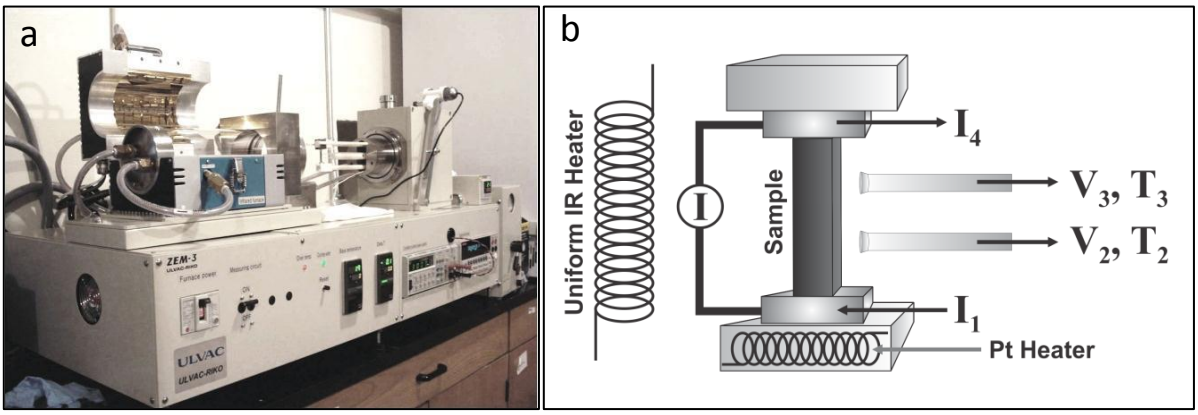

Figure 4-8 (a) ULVAC ZEM-3 (left) (b) ZEM schematic (right)[58]

The Seebeck coefficient is defined as $\frac{\Delta V}{\Delta T}$, so this value is measured by creating a temperature gradient across the bar and measuring the temperature difference, ΔT, and voltage difference, ΔV, across the same platinum-iridium thermocouples. The temperature difference across the bar is created by setting the platinum heater, shown below the bar, to a value higher than the ambient temperature. In this case, the platinum bar is set to 10 K, 15 K, and 20 K above the ambient, leading to ~1-1.5, ~1.5-2.0, and ~2.0-2.5 degree differences between the probes. The three measurements, corresponding to different ΔT's, are then averaged out into one experimental α, at each temperature.

A four-point probe method (Figure 4-10) is used to measure the electrical conductivity, where a current (I) is passed, in alternating directions, through the vertical electrodes, and V is measured across the horizontal probes used to measure α. Maintaining a constant current flow over the area (A) through the pellet, we can measure the potential difference between V_1 and V_2 across the physical length (L) between the probes, and calculate the material's resistance (R), Equation 4.3(a). The electrical conductivity can then be calculated using Equation 4.3(b) using the pellet dimensions and probe spacing.

4.3 (a) Ohm's Law (b) Specific conductivity

$$\text{(a) } R = \frac{V}{I} \qquad \text{(b) } \sigma = R^{-1} \cdot \frac{L}{A}$$

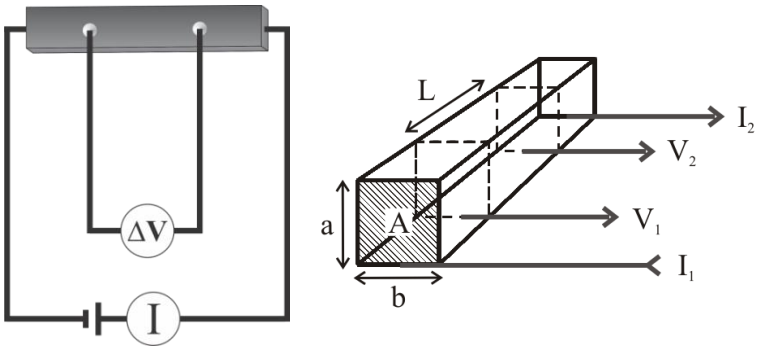

Figure 4-9 Four-point probe method.[58]

An international round-robin study on Bi_2Te_3 among seven labs, including the Kleinke lab, showed the reproducibility of multiple measurements within each lab, and compared the results between the different labs. The Seebeck coefficient measurement was highly reproducible between labs, and the scatter of data was $\pm$4 % in the 323 K to 498 K range.[80] On the other hand, the electrical conductivity measurement had a wider spread of up to $\pm$12.5 % over the same temperature range, which was mainly attributed to errors in measuring the probe separation, and bar dimensions.

5 $Tl_4(Zr,Hf)Te_4$

5.1 Introduction

The worldwide demand for energy is higher than ever and this forces us to look for new reliable and efficient methods for converting and producing energy. Thermoelectric materials can play an important role in satisfying some of this demand, by converting waste heat energy into electricity. Typical thermoelectric materials are inorganic semiconductors, where a balance between electrical conductivity and Seebeck coefficient, the voltage generated as a result of temperature gradient, allows for a high power factor. Currently, leading materials are heavily doped heavy metal chalcogenides, where low thermal conductivity has been observed along with a sufficient power factor.[2,75,81,82] The three properties mentioned above are used to evaluate the performance of a material through the thermoelectric figure-of-merit, $zT = T\alpha^2\sigma\kappa^{-1}$, where α is the Seebeck coefficient, σ the electrical conductivity and κ the thermal conductivity at a temperature T. The efficiency of a thermoelectric device is related to the zT of the materials used in it, such that a higher zT results in a more efficient generator. A common strategy for increasing zT in bulk materials is through nanostructuring and optimizing the pressing conditions to lower the thermal conductivity without changing the electrical conductivity and Seebeck coefficient.[17,83]

Materials containing thallium, Tl, and tellurium, Te, have attracted much attention for thermoelectric applications, mainly due to Tl being a heavy metal and its potential for structural complexity; resulting from the presence of a lone electron-pair on Tl combined with Te-Te bonding in these materials. Promising thermoelectric properties have been found for Tl_9SbTe_6,[21] Tl_9BiTe_6,[37] $Tl_{10-x}Sn_xTe_6$,[84] $TlBiTe_2$,[85] $TlSbTe_2$,[86] and $TlAg_9Te_5$.[22] To exploit these

advantages, the Kleinke group began exploring Tl-based ternary and quaternary chalcogenides incorporating a group 4 metal atom. During this process, the structures and physical properties of Tl_2MTe_3[49] and Tl_4MTe_4[48] with *M* = Zr, Hf were successfully determined. Initial investigation of structure and properties of cold-pressed $Tl_4Zr_{1.03}Te_4$ and Tl_4HfTe_4, showed a maximum zT of 0.16 at 420 K for $Tl_4Zr_{1.03}Te_4$, and a chance to improve the electrical conductivity through increasing the amount of Zr by partial occupation of the *M*3 site, to connect $ZrTe_6$ octahedra highlighted in Figure 5-1. This was not possible with the Hf-containing compound as highlighted in a previous study.[48] Now, we attempted to occupy this metal position and connect the MTe_6 octahedra through Nb-doping, and the properties of $Tl_4ZrNb_xTe_4$ (x = 0.02, 0.04, 0.06) after hot-pressing to more than ~95% relative density are reported in this chapter.

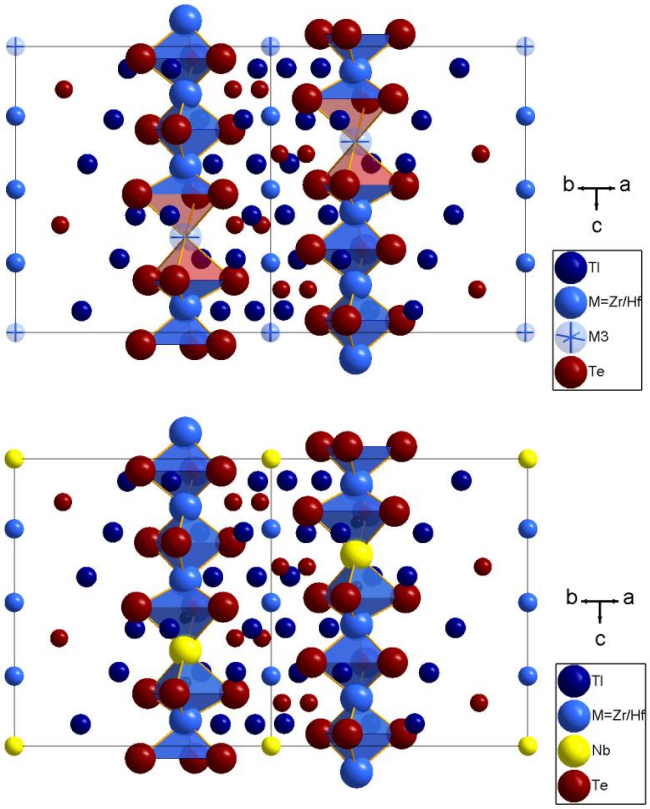

Figure 5-1 Unit cell of Tl_4MTe_4 (a) and Nb-doped Tl_4MTe_4 (b), MTe_6 octahedra highlighted.

5.2 Experimental

5.2.1 Synthesis and Analysis

The target compositions were synthesized from the constituent elements stored in an argon-filled glove box (Tl granules: 99.9%, Alfa Aesar; Zr pieces: 98.5%, Alfa Aesar; Hf pieces: 99.9% Alfa Aesar; Nb powder: -325 mesh, 99.8%, Alfa Aesar; Te broken ingots: 99.99%, Strem Chemicals). The Tl was purified from surface oxides prior to use. The elements were loaded in the required stoichiometry into quartz ampoules and sealed under vacuum. Various cooling rates and dwelling conditions were tested, and the conditions reported below were deemed appropriate for producing the desired phase with a significant yield. These ampoules were heated slowly to 1073 K in a resistance furnace, and then allowed to remain at 1073 K for 50 hours. Next, the ampoules are cooled down to 773 K at a rate of 1.5 K per hour, then kept at 773 K for 100 h, and then, finally, the furnace was switched off to cool down to room temperature. All tubes contained microcrystalline powder, from which single crystals were successfully extracted for the structure determination of the Tl_4ZrTe_4 compound. Zr and Hf-containing compounds both showed a silvery metallic color.

Pure samples were thoroughly ground, and then hot-pressed into round disk pellets with a diameter of 12.7 mm and a thickness of ~2 mm under a flow of argon in a graphite die using the FR-210-30T model hot-press from Oxy-Gon industries. The pressing conditions for the Zr and Hf-containing compounds were 62 MPa and 503 K for 1.5 hours. The densities for the pressed pellets were determined via the Archimedes method, which yielded ~90% and ~95% relative density for the Zr-and Hf-containing compounds, respectively.

Phase purity was verified for the samples using powder X-ray diffraction experiments, which were performed using an INEL powder diffractometer with position-sensitive detector and Cu-$K_{\alpha 1}$ radiation. The powder-XRD patterns for the $Tl_4Zr_{1.03}Te_4$ and Tl_4HfTe_4 samples after synthesis are shown in Figure 5-2 and Figure 5-3, respectively. The additional peaks at ~23° and ~31° observed in these samples may be due to Tl_5Te_3 side product, and the peak observed at ~27° for $Tl_4Zr_{1.03}Te_4$ may originate from $ZrTe_3$ side product.

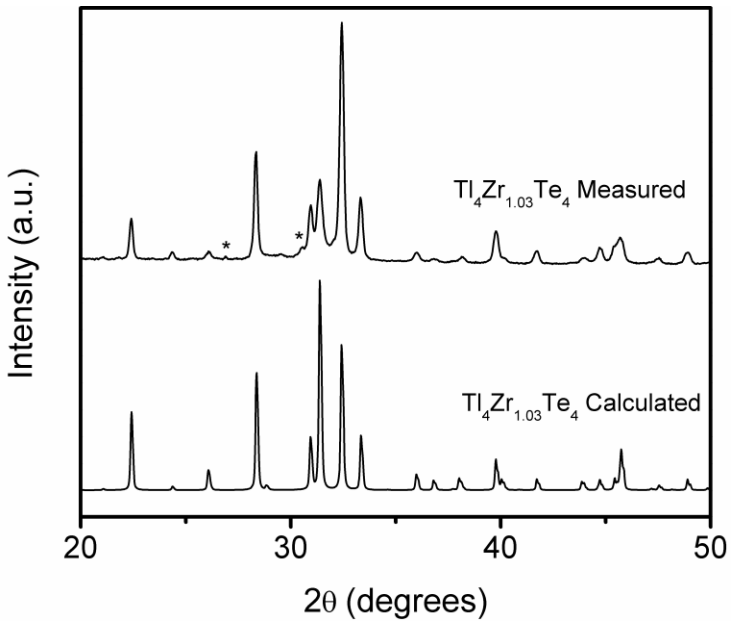

Figure 5-2 Experimental (top) and calculated (bottom) powder diagrams of $Tl_4Zr_{1.03}Te_4$.

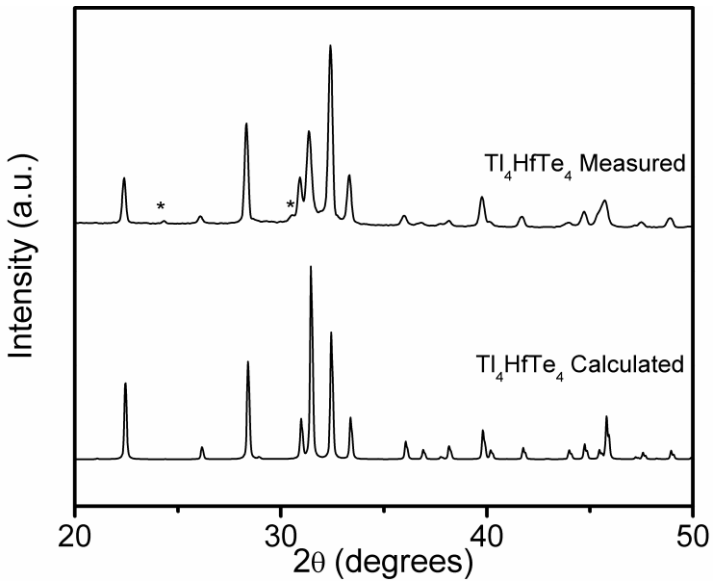

Figure 5-3 Experimental (top) and calculated (bottom) powder diagrams of Tl_4HfTe_4

Energy dispersive X-ray spectroscopy (EDX) was performed on selected spots of the pellet surface using Scanning Electron Microscope (SEM) image (Zeiss Ultra SEM/EDAX Team). The acceleration voltage was 25 kV under high dynamic vacuum, and the ratio of elements was confirmed from the observed spectrum. No impurities from the reaction container (Si, C) or atmosphere (O) were detected. Also, the element ratios were homogenous in both samples and within error of the theoretical values of 44 : 11 : 44 (in atomic-%) for $Tl_4Zr_{1.03}Te_4$ and 44 : 11 : 44 for Tl_4HfTe_4. The Tl : Zr : Te ratio for one of the Zr-containing samples was 47 : 12 : 41, while the Tl : Hf : Te ratio for the Hf-containing sample was 47 : 11 : 41. The EDX results from a pellet of a Hf-containing sample, to confirm homogeneity, is presented in Figure 5-4 (SEM image) and Table 5-1 (ratio of elements at each spot).

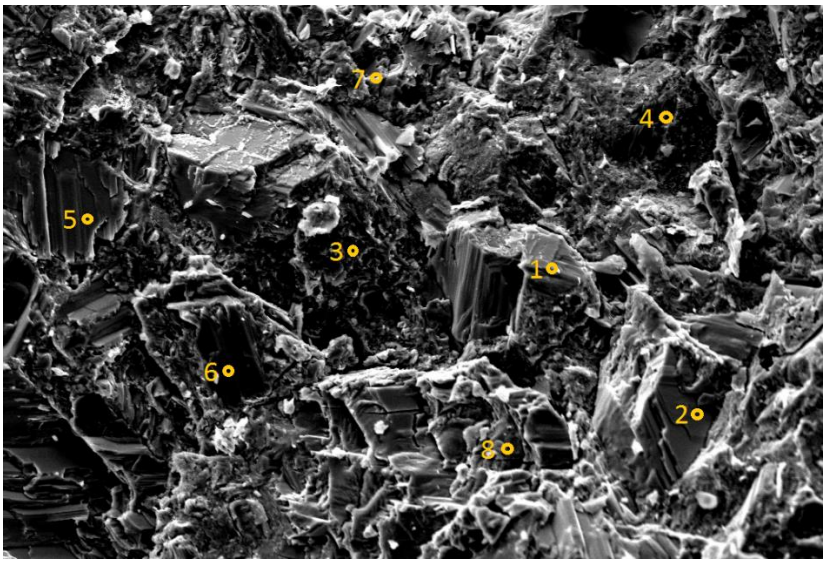

Figure 5-4 SEM of a Tl_4HfTe_4 pellet and EDX on various spots

Table 5-1 Ratio of elements at each spot on the Tl_4HfTe_4 pellet shown in Figure 3

	1	2	3	4	5	6	7	8	Average	Area	Expected
Tl	45.6	52.9	69.3	49.3	46.3	47.3	50.0	47.4	51	47.3	44.4
Hf	10.5	12.1	11.6	11.7	11	11.4	12.3	11.1	11.5	11.3	11.1
Te	43.9	35.0	19.1	39	42.7	41.3	37.7	41.4	37.5	41.4	44.4

5.2.2 Electronic Structure Calculation

The WIEN2k package was used for electronic structure calculations; it employs the density functional theory (DFT) via the full-potential linearized augmented plane wave (FP-LAPW) method.[23,24] The generalized gradient approximation (GGA), developed by Perdew et al., was used for exchange and correlation energies.[25] The various variables used in WIEN2k calculation were defined in section 2.2.1. The muffin-tin radii (R_{MT}) used for Tl, Zr, Hf, and Te in this calculation were 2.5 Bohr. The product of $R_{MT} \times K_{Max}$ was fixed to a value of 7. A 1000 *k* mesh was selected in an improved tetrahedron method for self-consistent energy calculations. The limit for energy convergence for self-consistency was set to 10^{-4} Ry. Furthermore, the WIEN2k

package allows for relativistic spin orbit (SO) coupling effect consideration for heavy atoms (i.e. Tl, Hf, Te), but these effects were not included in the calculations presented here.

5.2.3Physical Property Measurements

The pellets produced by hot-pressing were polished using 1000 grit sandpaper and coated with carbon in preparation for measurement of the thermal diffusivity, α, using the Anter Flashline 3000 (now TA Instruments), which utilizes a flash method under a flow of argon. Thermal conductivity, κ, was calculated via $\kappa = D\rho C_{\mathrm{p}}$, where ρ is the experimentally determined density, D is the measured diffusivity, and C_{p} is the specific heat capacity estimated as the Dulong-Petit limit for each compound.

Rectangular pellets, approximately 10 x 2 x 2 mm, were cut out of the disks and electrical transport measurements were carried out on these under helium over the temperature range of 305-620 K. The Seebeck coefficient and the electrical conductivity were measured as a function of temperature by a four-probe method, using the ULVAC-RIKO ZEM-3.

5.3 Discussion

5.3.1Crystal Structure

The tellurides Tl_4MTe_4 with *M* = Zr, Hf are isostructural, crystallizing in the trigonal system in the $R\bar{3}$ space group. The MTe_6 distorted octahedra run along the *c*-axis as shown in Figure 5-1. The previous report on these tellurides included the crystallographic information for Tl_4HfTe_4, while the single crystal analysis of the Zr-containing compound revealed extra Zr in the *M3* position such that the refined formula was $Tl_4Zr_{1+x}Te_4$ with x ≥ 0.3. Here, the crystallographic

information for a single crystal with the formula Tl_4ZrTe_4 is reported, as shown in Table 5-2, and the atomic positions for Tl_4ZrTe_4 are presented in Table 5-3.

Table 5-2 Crystallographic details of Tl_4ZrTe_4.

Refined formula	Tl_4ZrTe_4
T of measurement [K]	296(2)
Wavelength [Å]	0.71073
Crystal system	Trigonal
Space group	$R\bar{3}$
a [Å]	14.6003(8)
c [Å]	14.1424(10)
V [Å^3]	2610.8(3)
Z	9
ρ_{calcd} [g/cm^3]	8.123
*R*1 / *wR*2 (I > 2σ (I))[a]	0.0448 / 0.0558

Table 5-3 Atomic positions of Tl_4ZrTe_4.

Atom	Wyckoff site	*x*	*y*	*z*	U_{eq} / Å^2
Tl1	18f	0.44062(2)	0.38883(2)	0.42257(2)	0.03542(10)
Tl2	18f	0.40808(2)	0.13705(2)	0.75722(2)	0.03508(11)
Te1	6c	0.49138(3)	0.19395(3)	0.45768(3)	0.01753(13)
Te2	3b	0.51962(4)	0.37650(4)	0.68331(4)	0.02342(14)
Zr1	18f	2/3	1/3	0.59018(8)	0.0181(3)
Zr2	18f	2/3	1/3	1/3	0.0186(5)

The *M* atoms are surrounded by Te atoms in an octahedral arrangement and these octahedra share faces that connect along the *c*-direction. In the case where the *M3* position is not filled, every third of the Te_6 octahedra is empty. Previous studies indicated that Zr can occupy the *M3* position as reported for $Tl_4Zr_{1.03}Te_4$, however, not for the Hf-only compound. The *M1*–Te and

M2-Te bond lengths range from 2.83 to 3.00 Å, while the *M*3-Te bonds are slightly longer at about 3.30 Å. These bond lengths are similar to those found in other compounds with octahedrally coordinated Zr, such as $Zr_{1+x}Te_2$,[87] where three Zr-Te distances are 2.89 Å and three 2.91 Å. The Te-Te distances are relatively long in Tl_4MTe_4, with ~4.0 Å being the shortest distance, which indicates the lack of Te-Te interaction in these structures. The *M1*-*M2* distances are 3.63 Å and 3.61 Å for the Zr and Hf compounds, respectively. The *M3*-*M1* distance is about 3.46 Å, with the *M3* atom sitting between two *M*1 atoms. These distances are longer than typical *M*-*M* distances found in other elemental metals and metal-rich tellurides and antimonides. The Tl atoms sit between the MTe_6 channels, which cause the distortion in the channels. The Tl-Te polyhedra are irregular with the Tl1 atom surrounded by seven Te atoms. The Tl1-Te distances vary from 3.32 Å to 3.35 Å in the Zr case and from 3.32 Å to 3.89 Å in the Hf case. In contrast, the Tl2 atom is coordinated by five Te atoms with distances between 3.21 to 3.32 Å for the Zr case, and similar distances found for the Hf case. The shorter distances of Tl2-Te are similar to those found Tl-Te in Tl_2Te (3.30-3.42), while the Tl1-Te distances are comparable with those found for Tl-Te in $Tl_6Si_2Te_6$ between 3.27 Å and 3.67 Å.[88]

The vacancy in the *M*3 position presented a chance to incorporate another atom into the structure to alter its properties, and after initially examining the properties of hot-pressed Tl_4HfTe_4 and $Tl_4Zr_{1.03}Te_4$, we attempted to synthesize $Tl_4MNb_xTe_4$ (x=0.02, 0.04, 0.06) to place Nb into the *M*3 position. At this point, the $Tl_4ZrNb_xTe_4$ synthesis was successful, while the synthesis for the Hf variant resulted in reactions with the silica tube. Successfully adding Nb atoms in the *M*3 positon for the Zr-containing compound should increase the electron count.

5.3.2Electronic Structure

The DOS curves for Tl_4ZrTe_4 and Tl_4HfTe_4, without spin-orbit contribution, are shown in Figure 5-5. The previous LMTO electronic structure calculations suggest an indirect band gap of 0.3 eV for both Tl_4ZrTe_4 and Tl_4HfTe_4. However, the band structure obtained from WIEN2k shows smaller band gaps of 0.08 eV and 0.22 eV for Tl_4ZrTe_4 and Tl_4HfTe_4, respectively. The band gap for Tl_4ZrTe_4 is smaller than the minimum band gap of 6 $k_B T$ = 0.16 eV, at T = 300 K, suggested for thermoelectric materials.[2]

The Zr-Zr interactions were investigated through crystal orbital Hamilton population (*COHP*) curves, which were generated for all Zr-Zr interactions < 3.7 Å, and it was concluded that significant bonding interaction exists between the Zr atoms within that distance (i.e. the distance between the *M* atoms along the octahedral channels). The Tl-Tl interaction was previously investigated by means of integrated *COHP* (*ICOHP*) for distances in the range of 3.49 Å to 4.03 Å,[48] which showed significant interaction. The *ICOHP* for Tl-Tl for these compounds show similar behaviour to those found in Tl_5Te_3 and $Tl_6Si_2Te_6$.[88]

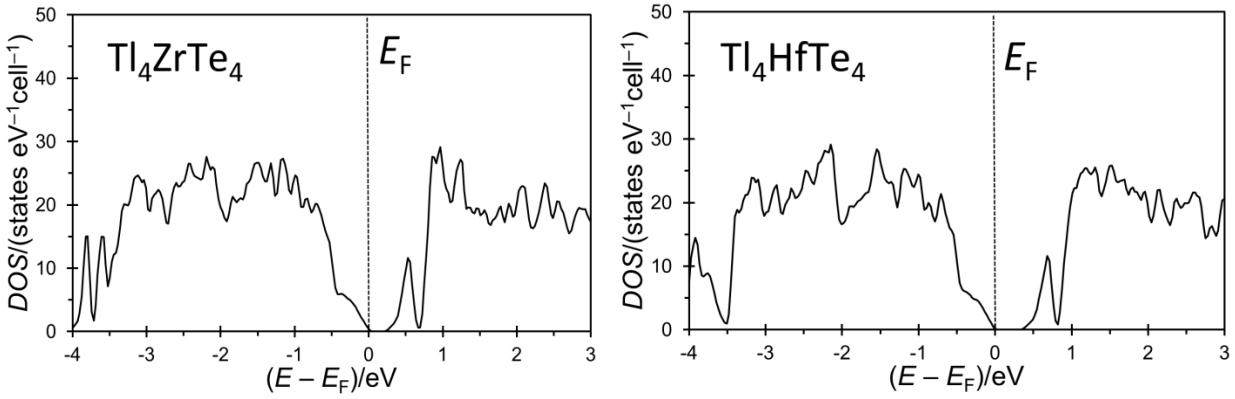

Figure 5-5 Calculated DOS for Tl_4ZrTe_4 (left) and Tl_4HfTe_4 (right).

5.3.3Physical Properties

Two different samples for each of the Zr and Hf containing compounds were characterized, namely $Tl_4Zr_{1.03}Te_4$-I, $Tl_4Zr_{1.03}Te_4$-II, Tl_4HfTe_4-I, and Tl_4HfTe_4-II. The electrical conductivity, shown in Figure 5-6, in the $Tl_4Zr_{1.03}Te_4$ samples is indicative of, possibly, extrinsic semiconductors, where the electrical conductivity, σ, decreases with temperature until the intrinsic carriers become significantly activated at about 450 K. The Tl_4HfTe_4 samples show a similar slight decrease in conductivity with temperature, however, the samples break down at approximately 550 K, before an increase could be observed.

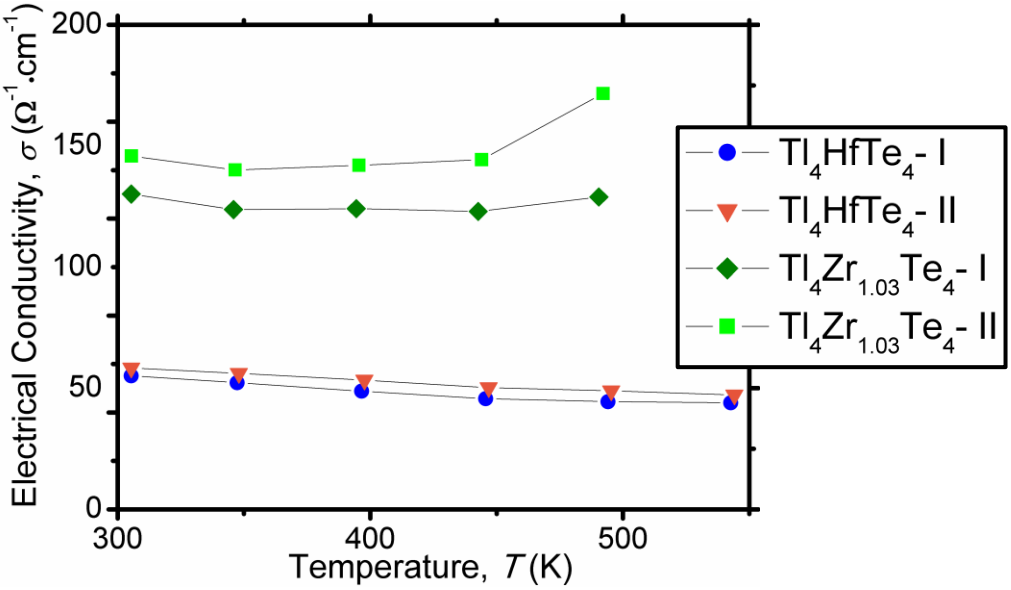

Figure 5-6 Electrical conductivity of $Tl_4Zr_{1.03}Te_4$ and Tl_4HfTe_4.

The higher σ values in $Tl_4Zr_{1.03}Te_4$-II over $Tl_4Zr_{1.03}Te_4$-I are possibly the result of minor weighing errors of Zr in sample II relative to sample I. Even with an experimental error of 5%, the difference between the samples is significant. At 490 K, the Zr-I sample has a σ of ~130 $\Omega^{-1}cm^{-1}$, while the Zr-II sample has ~170 $\Omega^{-1}cm^{-1}$. The two Hf-containing samples show almost identical σ with values of ~45 $\Omega^{-1}cm^{-1}$, which are well below the values found in the Zr compounds.

Much higher values are expected for these compounds when considering the small band gap calculated from the DOS, which would imply little energy is needed for carriers to be promoted from the valence band to the conduction band. This lower-than-expected value may be due to the presence of both types of charge carriers, holes and electrons, in these compounds. However, the smaller band gap calculated for the Zr-containing compound and the possibility for filling the *M*3 position support the higher σ measured in these compounds. These results are summarized in Table 5-4.

Table 5-4 Thermoelectric properties of $Tl_4Zr_{1.03}Te_4$ and Tl_4HfTe_4. The power factor was calculated via *P.F.* = $\alpha^2\sigma$ The Lorenz number, L, was calculated from the Seebeck coefficient, α, and used to derive the lattice thermal conductivity, κ_L, from the total thermal conductivity κ via $\kappa_L = \kappa - L\sigma T$. Finally, the figure-of-merit, zT, was calculated via $zT = T\alpha^2\sigma\kappa^{-1}$.

property	$Tl_4Zr_{1.05}Te_4$-I	$Tl_4Zr_{1.05}Te_4$-II	Tl_4HfTe_4-I	Tl_4HfTe_4-II
T	300 K \ 490 K	300 K \ 490 K	300 K \ 490 K	300 K \ 490 K
σ [$\Omega^{-1}cm^{-1}$]	130 \ 128	146 \ 172	58 \ 49	55 \ 45
α [$\mu V \cdot K^{-1}$]	43 \ 48	39 \ 43	69 \ 117	72 \ 113
P.F. [$\mu W \cdot cm^{-1}K^{-2}$]	0.24 \ 0.30	0.22 \ 0.33	0.28 \ 0.67	0.29 \ 0.57
L [10^{-8} V^2 K^{-2}]	2.27 \ 2.23	2.23 \ 2.28	2.11 \ 1.86	2.11 \ 1.86
κ [$W \cdot m^{-1}K^{-1}$]	0.38 \ 0.36	0.38 \ 0.38	0.46 \ 0.37	0.52 \ 0.42
κ_L [$W \cdot m^{-1}K^{-1}$]	0.29 \ 0.22	0.28 \ 0.18	0.42 \ 0.32	0.50 \ 0.38
zT	0.019 \ 0.042	0.017 \ 0.044	0.016 \ 0.081	0.015 \ 0.069

The temperature dependence of the Seebeck coefficient, α, is shown in Figure 5-7. The $Tl_4Zr_{1.03}Te_4$ samples show a flat trend in the temperature range measured, with a maximum

that appears at around 445 K for both samples. The Tl_4HfTe_4 samples show a steady increase with temperature, reaching a maximum of ~130 $\mu V \cdot K^{-1}$ at ~545 K. The measurements of the two samples of each of the two compounds, $Tl_4Zr_{1.03}Te_4$ and Tl_4HfTe_4, show high reproducibility of the Seebeck results. Also, repeat measurements on the Hf-containing samples, show high stability. The band gap, E_{gap}, approximation popularized by Goldsmid can be used for the Zr-containing compounds. The method utilizes the maximum α and the corresponding temperature via $E_{gap} = 2e\alpha_{max}T_{max}$, with e = electron charge.[89] Using α_{max} = 50 $\mu V \cdot K^{-1}$ and T_{max} = 443 K, we calculate E_{gap} = 0.05 eV for $Tl_4Zr_{1.03}Te_4$. This is comparable with the band gap of 0.08 eV from the DOS calculation. This method cannot be used for the Hf-containing compound as no clear maximum is reached prior to the compound breaking down.

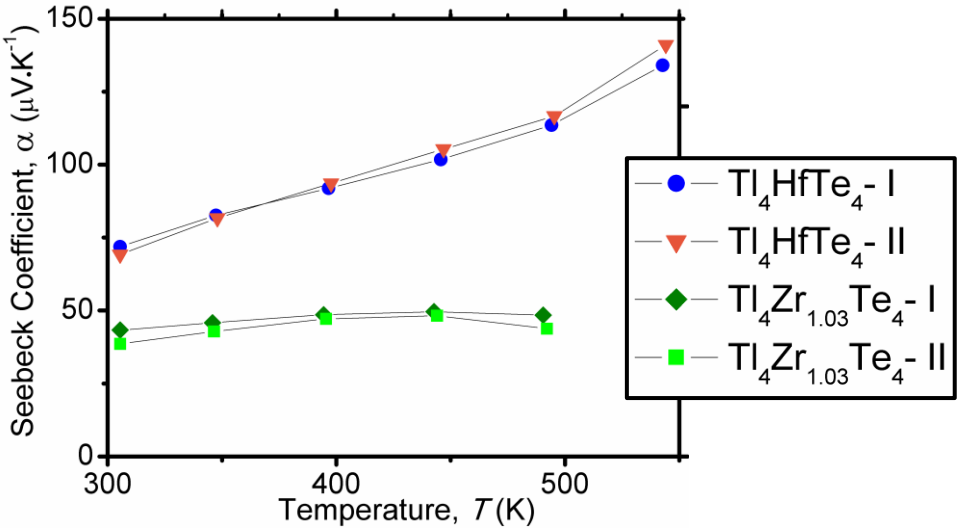

Figure 5-7 Seebeck coefficient of $Tl_4Zr_{1.03}Te_4$ and Tl_4HfTe_4.

The power factor, $P.F. = \alpha^2\sigma$, is usually used to evaluate the electrical performance of thermoelectric materials. The *P.F.* values for all samples, shown in Figure 5-8, are too low for TE

applications, and the Zr-containing compounds exhibit lower values than the Hf variant. The highest *P.F.* is for the Tl_4HfTe_4-II sample, which amounts to 0.94 $\mu W \cdot cm^{-1}K^{-2}$ at 545 K.

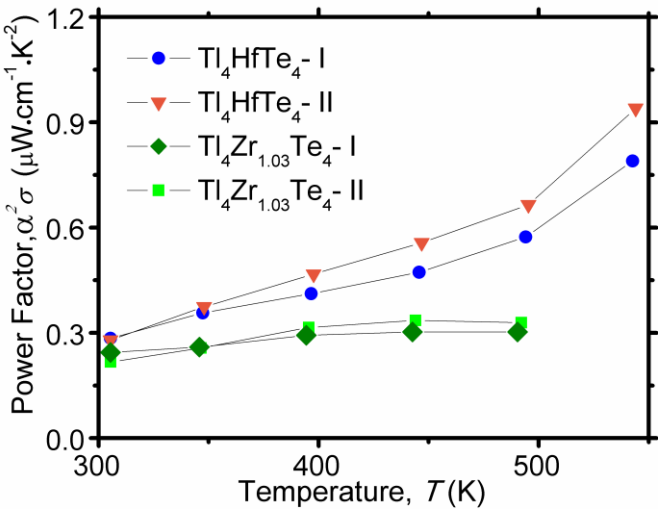

Figure 5-8 Power factor of $Tl_4Zr_{1.03}Te_4$ and Tl_4HfTe_4.

The thermal conductivity, κ, data for all compounds are presented in Figure 5-9. The values are consistently below 0.55 $W \cdot m^{-1}K^{-1}$ for all samples. The electronic contribution to the thermal conductivity is related to σ through $\kappa_e = L\sigma T$, where L is the Lorenz number. L was calculated from the experimental Seebeck coefficient by utilizing the single parabolic band and elastic carrier scattering assumption,[90] with acoustic phonon and/or alloying scattering (both resulting in the scattering parameter λ being 0).[91] Subtracting κ_e from the total thermal conductivity yields the lattice thermal conductivity, $\kappa_L = \kappa - \kappa_e$. The Lorenz numbers and resulting lattice thermal conductivity values are reported in Table 5-4 for selected temperatures. The exceptionally low thermal conductivity measured for these compounds is typical for thallium tellurides, such as for Tl_9BiTe_6[37] and Ag_9TlTe_5 [22] with ~0.39 $W \cdot m^{-1}K^{-1}$ and ~0.25 $W \cdot m^{-1}K^{-1}$, respectively.

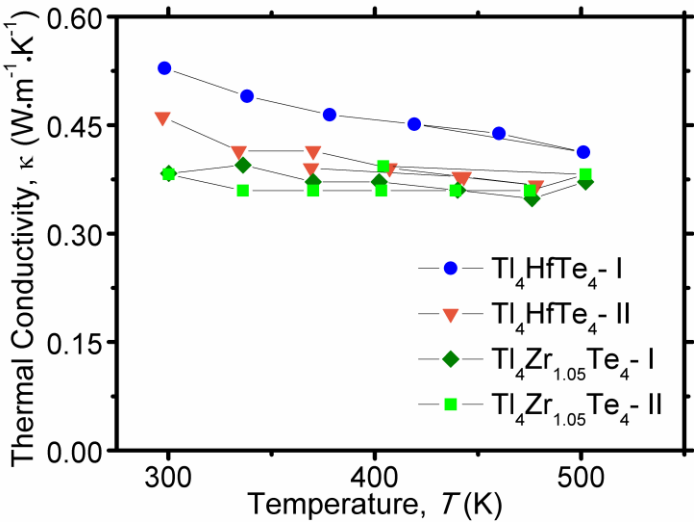

Figure 5-9 Thermal conductivity of $Tl_4Zr_{1.03}Te_4$ and Tl_4HfTe_4.

The thermoelectric figure-of-merit, zT, was calculated from the thermal conductivity data and fits to the experimental power factor data, which has a wider temperature range encompassing the κ measurements. The data are presented in Figure 5-10 and the Hf-containing compounds have a maximum zT of about 0.08 at ~480 K, while the Zr-containing compounds have a maximum zT of 0.04 at ~500 K. The zT values for the Zr compound show lower values from the value of 0.16 at 420 K reported for cold-pressed pellets, which is mainly due to the large Seebeck coefficient values measured for those cold-pressed samples. The Hf-containing sample on the other hand has about the same zT as reported for the cold-pressed one.

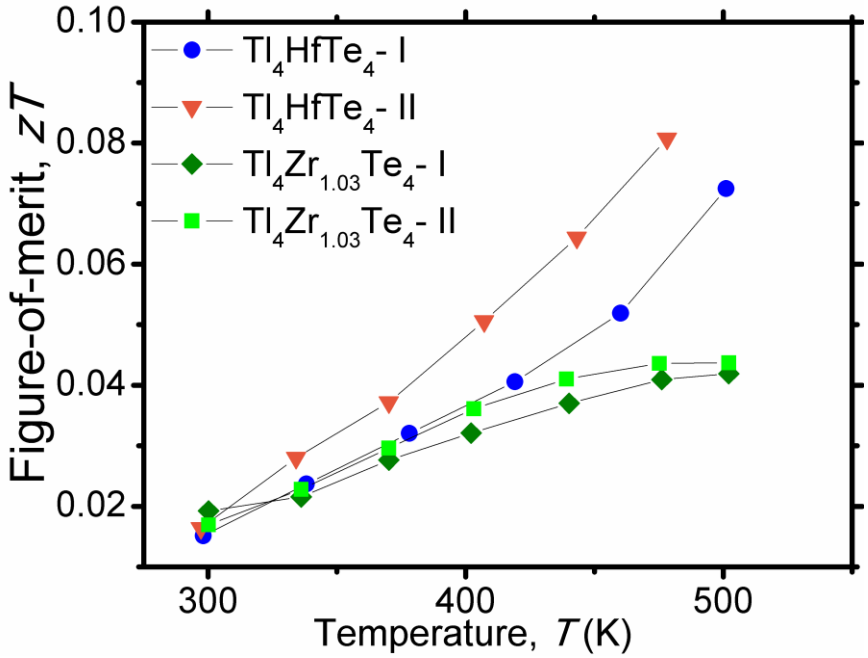

Figure 5-10 Thermoelectric figure-of-merit of $Tl_4Zr_{1.03}Te_4$ and Tl_4HfTe_4.

The properties for $Tl_4ZrNb_xTe_4$ (with x = 0.02, 0.04 and 0.06) samples are shown below, in Figures 5-11 through 5-15. The Nb-doped samples have higher electrical conductivity, across the measured temperature range, than the undoped sample, as shown in Figure 5-11. Furthermore, a trend can be seen within the doped samples, where the electrical conductivity increases as the dopant concentration increases. Namely, the highest electrical conductivity is for the $Tl_4ZrNb_{0.06}Te_4$ sample, which amounts to ~580 $\Omega^{-1}cm^{-1}$ at ~300 K and ~390 $\Omega^{-1}cm^{-1}$ at ~490 K. The charge balanced formula of the undoped compound is $(Tl^+)_4Zr^{4+}(Te^{2-})_4$. This compound may be viewed as $(Tl^+)_4(Zr^{4+})_{1.03}(Te^{2-})_4(e^-)_{0.12}$ (with e = electron), which suggests electrons as the dominant charge carriers, and *n*-type semiconductor behaviour. However, a positive Seebeck coefficient was measured for the Zr-containing samples, suggesting a *p*-type semiconductor. Doping Tl_4ZrTe_4 with Nb, in the *M*3 position, was expected to increase the number of electrons. For each increment of 0.02 for x, we expect to add about $3.4x10^{20}$carriers

per cm^3 per formula unit. The increase in electrical conductivity with increased of Nb content, of this *p*-type material, suggests that the number of holes in these compound increased, rather than the number of electrons. A possible factor contributing to the increase in electrical conducting is the measured increase in the relative density of Nb-doped samples, which would result in an increase in the mobility as well. The *p*-type semiconducting behaviour observed in $Tl_4Zr_{1+x}Te_4$, where x>0, can be explained by Anderson localization of electrons on the Zr atoms.[48] In the case where Nb atoms are not occupying the *M*3 position, undetected side products, such as Nb_3Te_4 and Tl_2Te, may be causing the target phase to have lower (Tl+Zr):Te ratio than intended. This would result in Tl/Zr vacancies, and thus explain the *p*-type doping as observed.

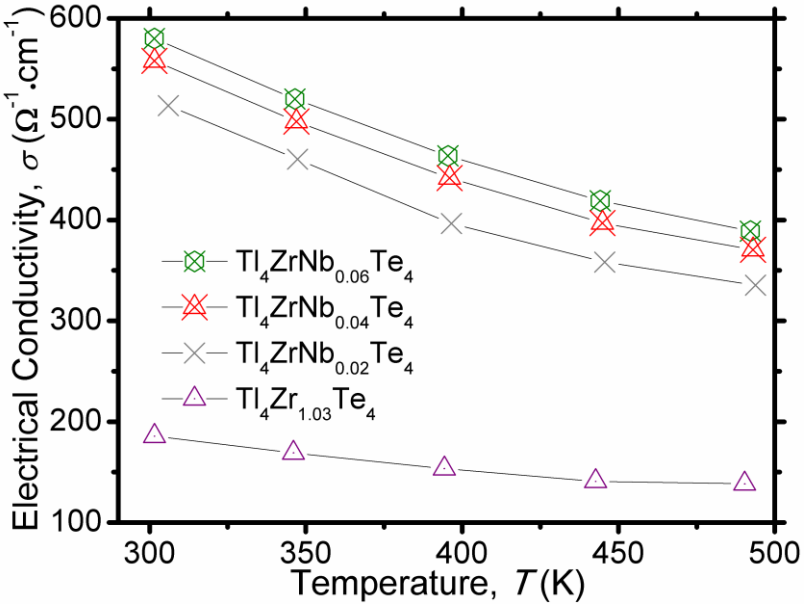

Figure 5-11 Electrical conductivity of $Tl_4ZrNb_xTe_4$ and $Tl_4Zr_{1.03}Te_4$.

The Seebeck coefficient, presented in Figure 5-12, shows slightly lower values for all Nb-containing samples than for the ternary material, but no significant differences between the

samples with different dopant levels. However, the latter may be due to measurement limits, and considering an error of 3% for the Seebeck measurement, we may have the reverse order as was observed in the electrical conductivity measurement. The Seebeck coefficient for the doped samples shows the same increasing trend as the undoped sample within the presented temperature range. The positive value observed for the Seebeck coefficient suggests *p*-type semiconductor behaviour, and doping with Nb lowers the value of the Seebeck coefficient, which points towards an increase in the number of holes and/or increase in mobility. This ambiguity in the effect of Nb-doping may be attributed to the presence of both types of carriers in these complex materials. A Hall measurement can shed light on the type of carriers and their mobility, which can help clarify the unusual effects of Nb doping in this compound. The higher density in the Nb-doped samples will increase the mobility of all carriers in these samples, and will result in a lower Seebeck coefficient. Calculating the Boltzmann transport properties along different directions, using a program like WANNIER90,[92] may help explain the transport properties measured in these samples. The values for the doped samples range between ~23 $\mu V \cdot K^{-1}$ at 300 K to ~40 $\mu V \cdot K^{-1}$ at 490 K for all three samples. Measuring the transport properties parallel and perpendicular to hot-pressing direction may reveal anisotropic behaviour in $Tl_4Zr_{1+x}Te_4$, because of its pseudo 1-D structure. Furthermore, a parallel may be drawn to the anisotropic behaviour in Bi_2Te_3, where the Seebeck coefficient calculated along different crystallographic directions differs with different number of carriers, holes and electrons, and with different temperatures.[93]

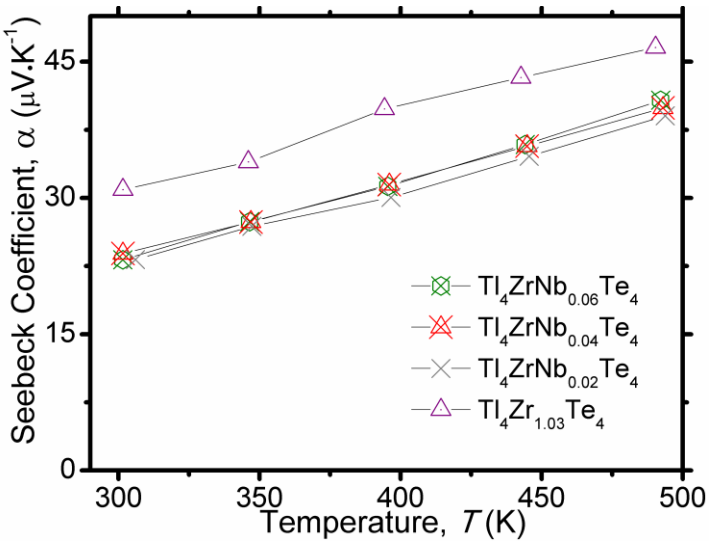

Figure 5-12 Seebeck coefficient of $Tl_4ZrNb_xTe_4$ and $Tl_4Zr_{1.03}Te_4$.

The power factor, $P.F. = \alpha^2\sigma$, is used to measure the electrical performance of a TE material, and the power factors for these samples are compared in Figure 5-13 below. The same trend can be seen here as the one for the electrical conductivity of these samples. As the Seebeck coefficient for all Nb samples showed similar values, the trend is dominated by the difference in electrical conductivity, and the highest power factor is for the sample with the highest Nb content. More specifically, the "$Tl_4ZrNb_{0.06}Te_4$" sample has a power factor of 0.65 $\mu W \cdot cm^{-1}K^{-2}$ at ~490 K.

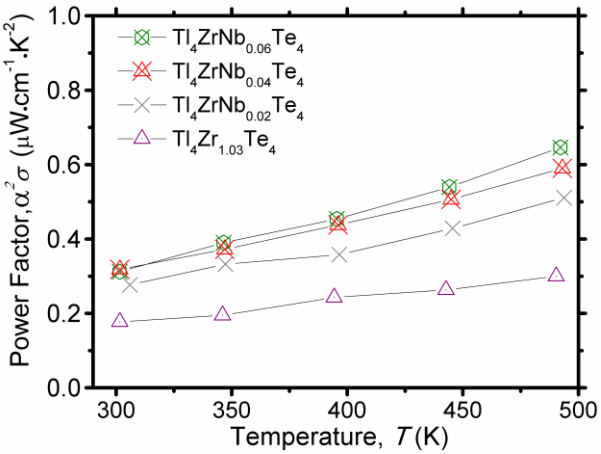

Figure 5-13 Power factor of $Tl_4ZrNb_xTe_4$ and $Tl_4Zr_{1.03}Te_4$.

The thermal conductivity (Figure 5-14) shows the same trend as the electrical conductivity, with the sample with the highest Nb content having the highest thermal conductivity. Increase in electrical conductivity will increase the electronic contribution to the thermal conductivity, which explains the consistency in the trend. The thermal conductivity for the $Tl_4ZrNb_{0.06}Te_4$ sample is 0.56 $W{\cdot}m^{-1}K^{-1}$ at ~500 K, while the Nb-free sample has a value of 0.37 $W{\cdot}m^{-1}K^{-1}$ at ~500 K.

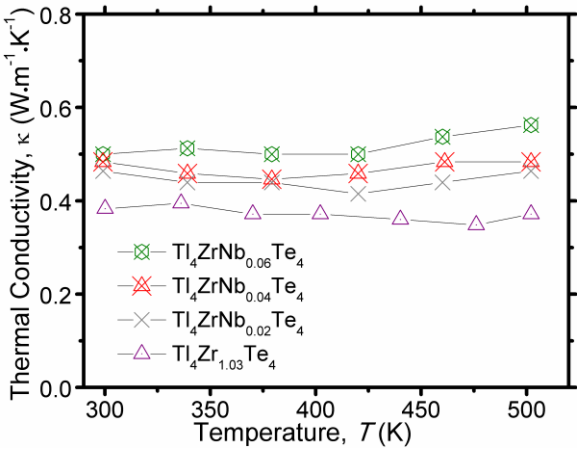

Figure 5-14 Thermal Conductivity of $Tl_4ZrNb_xTe_4$ and $Tl_4Zr_{1.03}Te_4$.

The thermoelectric figure-of-merit, zT, was calculated from the thermal conductivity data and fits to the experimental power factor. The best zT calculated is 0.064 at ~500 K for the $Tl_4ZrNb_{0.04}Te_4$ sample, which is due to the significant increase in the power factor without as large an increase in the thermal conductivity. However, the zT values for the various Nb samples are within experimental error of each other. As such, we can say that the Nb samples show significant increase in zT over the undoped sample, but variations between the zT values of the different doped samples are not significant.

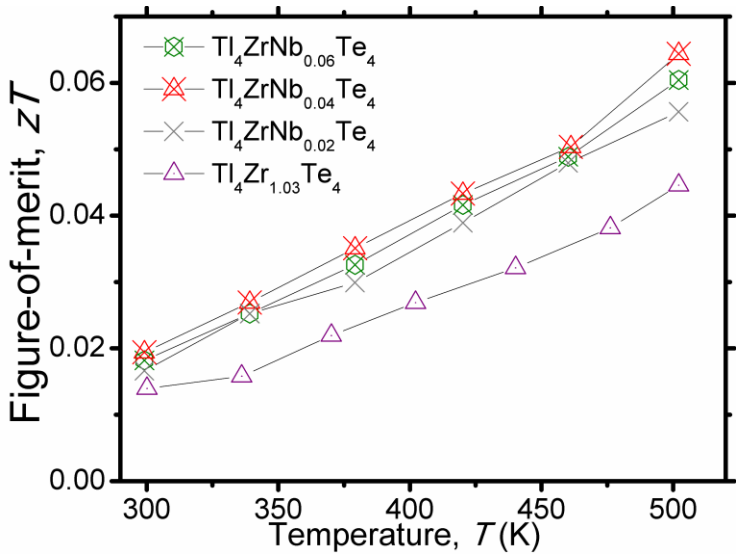

Figure 5-15 Thermoelectric figure-of-merit of $Tl_4ZrNb_xTe_4$ and $Tl_4Zr_{1.03}Te_4$.

5.4 Conclusion

The thermoelectric properties of Tl_4HfTe_4, $Tl_4Zr_{1.03}Te_4$, and $Tl_4ZrNb_xTe_4$ (x = 0.02, 0.04, 0.06) were measured and presented. The properties of Tl_4HfTe_4 and $Tl_4Zr_{1.03}Te_4$, measured for two samples of each compound, are compared, and the thermal conductivity for the two compounds are similar in the measured temperature range. The Hf-containing compound has a higher Seebeck coefficient than the Zr-containing one, which, even when combined with the

lower electrical conductivity, results in the higher power factor for Tl_4HfTe_4 over $Tl_4Zr_{1.03}Te_4$. This results in a higher zT value for Tl_4HfTe_4, reaching a value of 0.08 at ~490 K. Next, the effect of Nb additions to Tl_4ZrTe_4 is highlighted by comparing the various properties to those of $Tl_4Zr_{1.03}Te_4$. The doped samples show systematically higher electrical and thermal conductivity, while their Seebeck coefficient is slightly lower, and has about the same value for all three Nb samples. The power factor shows the same trend as the electrical conductivity, but the zT values for all three Nb samples are very close to each other. The highest zT was found for the $Tl_4ZrNb_{0.04}Te_4$ sample, which amounted to 0.064 at ~500 K. One can conclude that Nb additions result in improved thermoelectric performance of $Tl_4Zr_{1.03}Te_4$, but one cannot pick the ideal level of dopant from the current study. Finally, it should be mentioned that the zT values for compounds in this study are far below state-of-the-art thermoelectrics, and, even with further optimization, it is unlikely they will be suitable for commercial application.

6 $Ba_3Cu_{16-x}S_{11-y}Te_y$

6.1 Introduction

Typically, advanced thermoelectric materials are narrow-band gap semiconductors, and many are heavily doped heavy metal chalcogenides, such as bismuth, thallium, and lead tellurides.[2,21,75,81,82,94] Another class of materials that achieve low thermal conductivity are ones with cation mobility, mobile copper ions for example. The case for $Cu_{2-x}Se$ is well documented in literature, and the material has a very low thermal conductivity, contributing to a high zT of 1.5 at 1000 K.[20] The Cu ion conductivity, however, results in well-documented stability issues, constraining the use of such material in an actual devices, because the Cu ions move with the temperature gradient.[50] We have been investigating new metal chalcogenides in recent years, and many new phases were discovered in the barium copper chalcogenide system. It was hoped, that the 6th period barium ions would impede the Cu paths, and, also, contribute to low thermal conductivity. Several new *p*-type semiconducting materials were discovered, including $Ba_3Cu_{14-x}Te_{12}$,[95] $Ba_{6.76}Cu_{2.42}Te_{14}$,[96] $Ba_2Cu_{4-x}Te_5$ and $Ba_2Cu_{4-x}Se_yTe_{5-y}$,[97] $Ba_2Cu_{6-x}STe_4$ and $Ba_2Cu_{6-x}Se_yTe_{5-y}$,[98] $BaCu_{6-x}STe_6$ and $BaCu_{6-x}Se_{1-y}Te_{6+y}$,[52] and $Ba_3Cu_{16-x}Se_{11-y}Te_y$.[53] Other materials are $Ba_2Cu_{7-x}Te_6$[99] and $Ba_3Cu_{17-x}S_{11.5-y}Te_y$,[51] which exhibit one and three-dimensional metallic properties, respectively. Various Cu clusters (with Cu–Cu bonds) are found in all of these materials, as well as Cu atom deficiencies, and hence they are of *p*-type character.[100] In most cases, the Cu atom network is infinitely extended in at least one direction, which results in possible diffusion paths of the Cu atoms across the material. $Ba_{6.76}Cu_{2.42}Te_{14}$ and $BaCu_{6-x}STe_6$

and $BaCu_{6-x}Se_{1-y}Te_{6+y}$ showed localized Cu atom clusters, but the first has very low electrical conductivity because of the high barium content. Here we further investigate the properties and stability of $Ba_3Cu_{16-x}S_{11-y}Te_y$, with y < 5.5, which demonstrated relatively good thermoelectric properties for cold-pressed pellets.

6.2 Experimental

6.2.1Synthesis and Analysis

The constituent solid elements, stored in an argon-filled glove box, were used to synthesize the title compounds (Ba pieces: 99.7%, Strem Chemicals; Cu powder: 99.5%, Alfa Aesar; S flakes: 99.98%, Aldrich; Te broken ingots: 99.99%, Strem Chemicals). To reduce contamination with oxygen, we scraped off the surface of the barium pieces. Four samples were prepared at this point, namely $Ba_3Cu_{16}S_8Te_3$, $Ba_3Cu_{16}S_9Te_2$, $Ba_3Cu_{15.1}S_7Te_4$, and $Ba_3Cu_{15.1}S_8Te_3$. The elements were loaded in the desired stoichiometric ratios into carbon-coated silica tubes, which were then evacuated up to ~10^{-3} mbar. The silica tubes were then sealed with a hydrogen-oxygen flame, and then placed into a programmable resistance furnace for the heat treatment. The furnace was programmed to reach 1073 K within 12 hours, and then stay at 1073 K for 6 hours. Next, the furnace was cooled down to 873 K over 100 hours, and maintained at 873 K for 100 more hours, before being turned off to cool the samples down to room temperature. Cooling slowly through the 1073 K - 873 K range is ideal to crystallize the target materials, as the melting point of $Ba_3Cu_{16}S_7Te_4$ is about ~940 K, as determined by a DSC measurement.[52] The isothermal step at 873 K serves as an annealing step to ensure homogeneity of the samples. The purities after the synthesis were confirmed via powder X-ray diffraction on the group's INEL

powder diffractometer, and are presented in Figure 6-1 for $Ba_3Cu_{16}S_8Te_3$, along with the temperature profile used in the synthesis. The high number of peaks in the diffraction pattern expected for this compound makes it difficult to identify impurities, as they may be masked by the strong diffraction of the target compound.

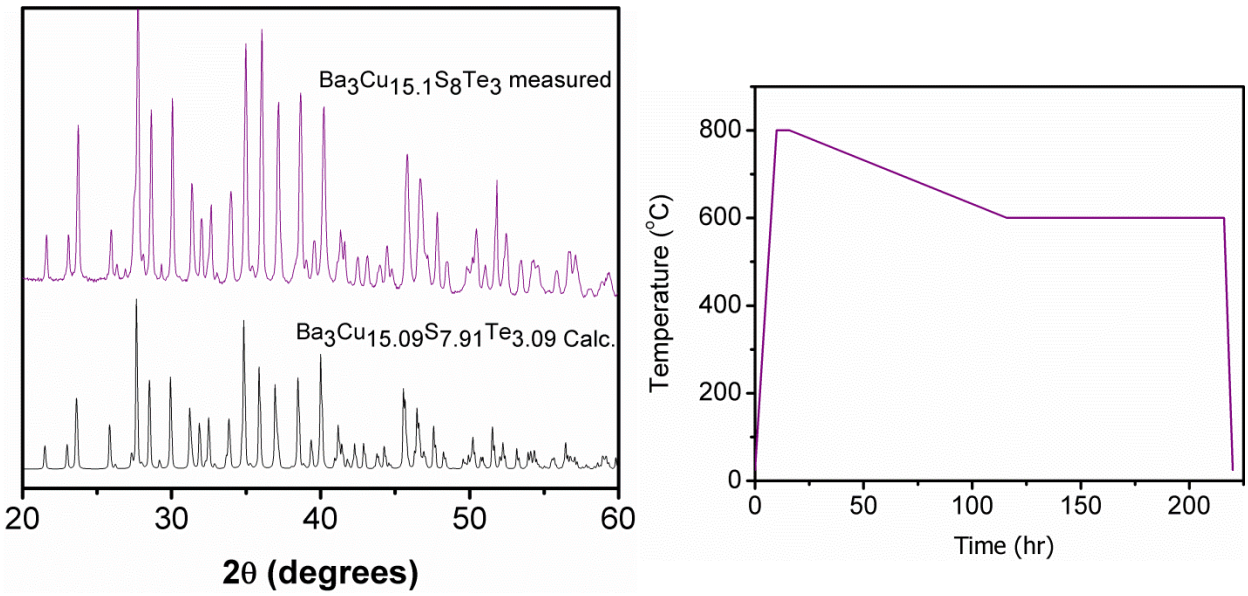

Figure 6-1(a) Experimental (top) and calculated (bottom) powder diagrams of $Ba_3Cu_{15.1}S_8Te_3$. (b) Temperature profile for the $Ba_3Cu_{16-x}S_{11-y}Te_y$ synthesis.

The two pure samples were hot-pressed into round disk pellets with a diameter of 12.7 mm and a thickness of ~1.7 mm in a graphite die under an argon flow using the FR-210-30T hot press (Oxy-Gon Industries). The optimized pressing conditions for these compounds were 62 MPa at 853 K for two hours, which resulted in highly dense pellets without causing noticeable decomposition. Archimedes' method was used to determine the densities of pressed pellets, which yielded >96% of the theoretical maximal values for both samples presented here.

Energy dispersive X-ray spectroscopy (EDX) was performed on selected spots of the pellet surfaces after the ZEM measurement, using the Zeiss Ultra SEM and EDAX Team software. The

measurement was done under high dynamic vacuum with an acceleration voltage of 25 kV, and the elemental ratios were determined from the resulting spectrum. The ratios of elements, Ba : Cu : S : Te, are expected to be 10.1 : 52.9 : 26.9 : 10.1 for $Ba_3Cu_{16}S_8Te_3$, and these were compared to the experimental EDX result. These results are presented in the next section, and discussed to assess the stability of samples.

6.2.2Physical Property Measurements

The hot-pressed pellets were polished using 1000 grit sandpaper and spray-coated with carbon to prepare them for the thermal diffusivity, α, measurements up to 620 K, using the Anter Flashline 3000 (now TA Instruments), which utilizes a flash method under an argon flow. Thermal conductivity, κ, was then calculated via $\kappa = D\rho C_{\mathrm{p}}$, where ρ is the experimental density, D is the measured thermal diffusivity, and C_{p} is the specific heat capacity estimated for the compound as the Dulong-Petit limit. The Dulong-Petit limit is a good approximation where experimental heat capacity data are unavailable.[76]

Rectangular pellets, with approximate dimensions of 10 x 2 x 2 mm, were cut from the disks, in preparation for the electrical transport measurements. The Seebeck coefficient, α, and the electrical conductivity, σ, were both measured, simultaneously, as a function of temperature up to 770 K under helium. This was done using the ULVAC-RIKO ZEM-3, which utilizes a four-probe method.[80] The measurements were repeated on the same pellets to check for reproducibility of the results for all samples, and six measurements in total were done for the $Ba_3Cu_{16}S_8Te_3$ sample.

6.3 Discussion

6.3.1 Crystal Structure

The unit cells of these polychalcogenides are large, as expected for a structure of a material with a complex formula containing four different elements, with a 3-D network of Cu-centered polyhedra. $Ba_3Cu_{16-x}S_{11-y}Te_y$ crystallizes in a rhombohedral unit cell for y < 5.5, and is isostructural to the previously reported $Ba_3Cu_{16-x}Se_{11-y}Te_y$.[53] The compounds adopt the $R\bar{3}m$ space group, and feature interconnected Cu_{26} clusters forming a 3-D network.[51]

When these compounds have sixteen Cu atoms per formula unit, the charge balanced formula is obtained according to $(Ba^{2+})_3(Cu^{+})_{16}(S^{2-})_{11-y}(Te^{2-})_y$. The highest amount of Cu per cell experimentally obtained was 15.7, which gives these compounds their extrinsic *p*-type semiconductor behaviour. The slight deficiency in Cu for all compounds synthesized, along with the 3-D network of Cu sites within bonding distance, allows for the migration of Cu atoms, beyond the unit cell, and hence, across the material. This is expected to result in the material to break down under heat cycling, as documented for Cu_2Se.[50] The deficiency of Cu atoms in our samples can be confirmed by carefully examining the p-XRD pattern below 30 degrees and through EDX. Another method for identifying the ration of elements in our samples, and confirm the Cu content, is using electron probe micro-analyzer (EPMA).

6.3.2 Physical Properties

Four samples of nominal compositions $Ba_3Cu_{16}S_8Te_3$, $Ba_3Cu_{16}S_9Te_2$, $Ba_3Cu_{15.1}S_7Te_4$, and $Ba_3Cu_{15.1}S_8Te_3$ were characterized, and the electrical conductivity data are presented in Figure 6-2 below. The electrical conductivity data are typical for an extrinsic semiconductor in the case of $Ba_3Cu_{15.1}S_8Te_3$ and $Ba_3Cu_{16}S_8Te_3$, where the conductivity, σ, decreases at first as temperature

increases, and then begins to increase, once intrinsic carriers gain enough energy to cross the band gap in significant numbers. The conductivity for $Ba_3Cu_{16}S_9Te_2$, in contrast, shows much lower values and increases slightly with increasing temperature, typical for an intrinsic semiconductor. These results can be explained with less copper atoms in the $Ba_3Cu_{16}S_8Te_3$ sample than the expected 16, resulting in a higher number of holes for the $Ba_3Cu_{16}S_8Te_3$ compound than the $Ba_3Cu_{16}S_9Te_2$ sample. Also, the higher S content may result in slightly lower mobility of charge carriers, due to the higher electronegativity compared to Te. $Ba_3Cu_{15.1}S_7Te_4$ shows similar values to those observed for $Ba_3Cu_{16}S_8Te_3$, and the reason for this is not understood at this point. Comparing results for more samples with various S:Te ratio and Cu content can clarify these trends.

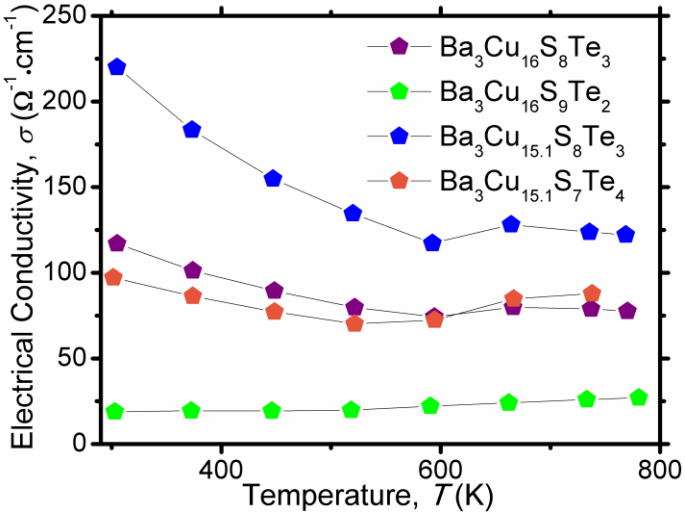

Figure 6-2 Electrical conductivity of $Ba_3Cu_{16-x}S_{11-y}Te_y$ samples.

The electrical conductivity for the $Ba_3Cu_{16}S_8Te_3$ sample varies from ~120 $\Omega^{-1}cm^{-1}$ at 300 K to ~75 $\Omega^{-1}cm^{-1}$ at ~770 K, while the conductivity of $Ba_3Cu_{16}S_9Te_2$ is ~20 $\Omega^{-1}cm^{-1}$ for the whole temperature range. The electrical conductivity for the $Ba_3Cu_{15.1}S_8Te_3$ sample varies from ~220 $\Omega^{-1}cm^{-1}$ at 300 K to ~125 $\Omega^{-1}cm^{-1}$ at ~770 K, and the electrical conductivity for the

$Ba_3Cu_{15.1}S_7Te_4$ sample varies from ~100 $\Omega^{-1}cm^{-1}$ at 300 K to ~88 $\Omega^{-1}cm^{-1}$ at ~740 K. The Seebeck coefficient results are presented in Figure 6-3 below, and these show the opposite trend, where $Ba_3Cu_{16}S_9Te_2$ has the highest values and the $Ba_3Cu_{15.1}S_8Te_3$ sample shows the lowest values. All compounds show an increasing Seebeck coefficient with increasing temperature, and the highest values for $Ba_3Cu_{15.1}S_8Te_3$ and $Ba_3Cu_{16}S_9Te_2$ at ~770 K are ~200 $\mu V\ K^{-1}$ and ~280 $\mu V\ K^{-1}$, respectively. The higher number of charge carriers is expected to result in higher electrical conductivity and lower Seebeck coefficient, which is seen here, with the exception of the $Ba_3Cu_{15.1}S_7Te_4$ sample. The results for these samples are summarized in Table 6-1 below.

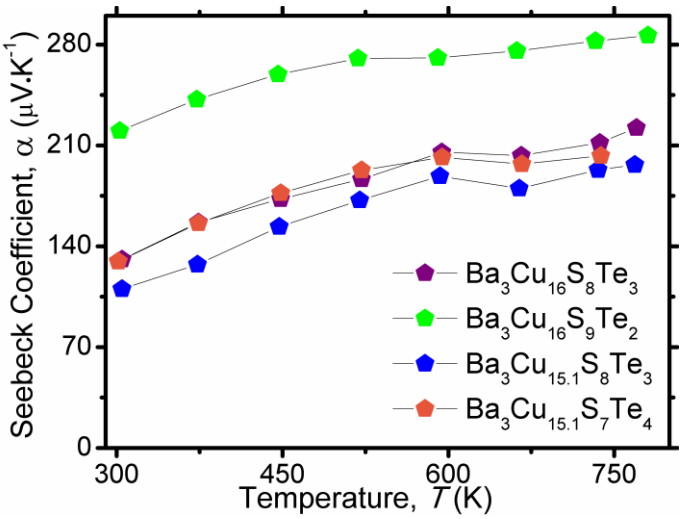

Figure 6-3 Seebeck coefficient of $Ba_3Cu_{16-x}S_{11-y}Te_y$ samples.

Table 6-1 Thermoelectric properties of $Ba_3Cu_{16-x}S_{11-y}Te_y$ samples. The power factor was calculated via *P.F.* = $\alpha^2\sigma$ The Lorenz number, L, was calculated from the Seebeck coefficient, α, and used to derive the lattice thermal conductivity, κ_L, from the total thermal conductivity κ via $\kappa_L = \kappa - L\sigma T$. Finally, the figure-of-merit, zT, was calculated via $zT = T\alpha^2\sigma\kappa^{-1}$.

property	$Ba_3Cu_{16}S_9Te_2$	$Ba_3Cu_{16}S_8Te_3$	$Ba_3Cu_{15.1}S_8Te_3$	$Ba_3Cu_{15.1}S_7Te_4$
T	320 K \ 685 K	320 K \ 685 K	320 K \ 685 K	320 K \ 685 K
σ [$\Omega^{-1}cm^{-1}$]	24 \ 26	113 \ 79	162 \ 117	88 \ 87
α [$\mu V \cdot K^{-1}$]	219 \ 277	140 \ 206	128 \ 194	143 \ 188
P.F. [$\mu W \cdot cm^{-1}K^{-2}$]	1.1 \ 2.0	2.2 \ 3.4	2.6 \ 4.4	1.8 \ 3.1
L [$10^{-8}\ V^2\ K^{-2}$]	1.59 \ 1.54	1.75 \ 1.61	1.80 \ 1.63	1.75 \ 1.64
κ [$W \cdot m^{-1}K^{-1}$]	0.39 \ 0.37	0.47 \ 0.47	0.47 \ 0.47	0.48 \ 0.52
κ_L [$W \cdot m^{-1}K^{-1}$]	0.38 \ 0.34	0.41 \ 0.38	0.38 \ 0.34	0.43 \ 0.42
zT	0.09 \ 0.38	0.15 \ 0.49	0.18 \ 0.63	0.12 \ 0.41

The power factor, *P.F.* = $\alpha^2\sigma$, appearing in the numerator of zT, serves as a good measure of a material's electrical performance. As shown in Figure 6-4, the power factor increases with temperature between 300 K and 770 K for all compounds. The *P.F.* reaches a maximum of ~4.7 μW $cm^{-1}K^{-2}$, ~3.9 μW $cm^{-1}K^{-2}$ and ~2.2 μW $cm^{-1}K^{-2}$ at ~770 K for $Ba_3Cu_{15.1}S_8Te_3$, $Ba_3Cu_{16}S_8Te_3$ and $Ba_3Cu_{16}S_9Te_2$, respectively. As we decrease the S:Te ratio and decrease the Cu content, we increase the electrical conductivity and bring down the Seebeck coefficient, but the effect on the electrical conductivity is greater than on the Seebeck coefficient. This results in an overall increase in the *P.F.*, which is seen for these samples, with the exception of the $Ba_3Cu_{15.1}S_7Te_4$ sample.

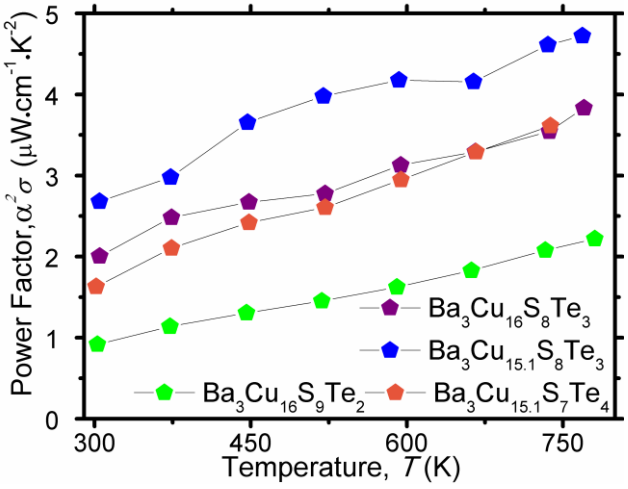

Figure 6-4 Power factor of $Ba_3Cu_{16-x}S_{11-y}Te_y$ samples.

The thermal conductivity, κ, data for all compounds are presented in Figure 6-5. The values are very low, consistently below 0.6 W $m^{-1}K^{-1}$, which is even lower than values for β-Cu_2Se (1.04 W $m^{-1}K^{-1}$ at 420 K; 0.98 $Wm^{-1}K^{-1}$ at 600 K).[20] The values show little fluctuation across the measured temperature range, where κ for both $Ba_3Cu_{16}S_8Te_3$ and $Ba_3Cu_{15.1}S_8Te_3$ is ~0.50 W $m^{-1}K^{-1}$ for the whole measurement, and κ for $Ba_3Cu_{15.1}S_7Te_4$ and $Ba_3Cu_{16}S_9Te_2$ is ~0.43 W $m^{-1}K^{-1}$

and ~0.40 W $m^{-1}K^{-1}$, respectively. For the $Ba_3Cu_{15.1}S_8Te_3$ sample, a sudden increase in thermal conductivity is observed at ~690 K, which is likely due to measurement error, and this is reflected in a sudden decrease in zT at the sample temperature. Repeating this measurement on another $Ba_3Cu_{15.1}S_8Te_3$ sample would help confirm the origin of this suspicious data point.

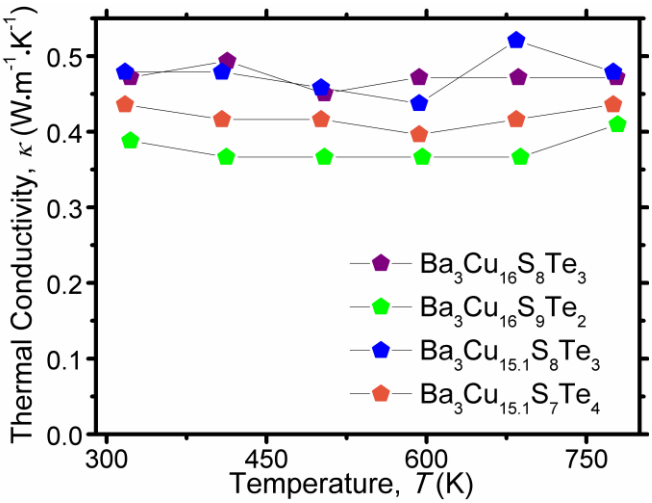

Figure 6-5 Thermal conductivity of $Ba_3Cu_{16-x}S_{11-y}Te_y$ samples.

Finally, the thermoelectric figure-of-merit, zT, was computed from the thermal conductivity data and fits to the experimental power factor data that encompass the temperature range of the κ measurements. The data, up to 770 K, are presented in Figure 6-6 below. As typical for doped semiconductors, the zT values increase with increasing temperature. The sulfide-telluride samples reach their maximum zT at ~770 K, and values of 0.78, 0.65 and 0.42 are calculated for $Ba_3Cu_{15.1}S_8Te_3$, $Ba_3Cu_{16}S_8Te_3$ and $Ba_3Cu_{16}S_9Te_2$, respectively. $Ba_3Cu_{15.1}S_7Te_4$ reaches a zT of 0.55 at ~685 K.

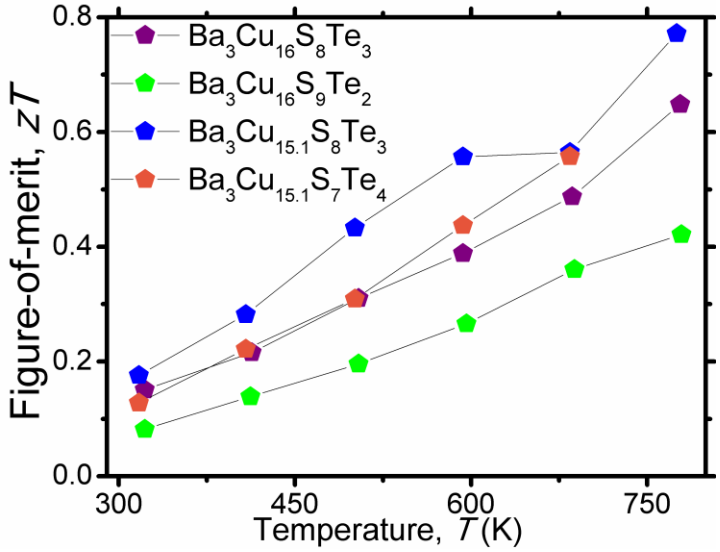

Figure 6-6 Thermoelectric figure-of-merit of $Ba_3Cu_{16-x}S_{11-y}Te_y$ samples.

The stability of the electrical transport measurements was of interest for these compounds, so the ZEM measurement was repeated six times for the $Ba_3Cu_{16}S_8Te_3$ sample, and the results are compared in Figure 6-7 for the electrical conductivity and Seebeck coefficient measurement. These results show high reproducibility of the electrical transport properties, and the measurements can be considered equivalent with an estimated error of 5% and 3% for σ and α, respectively.

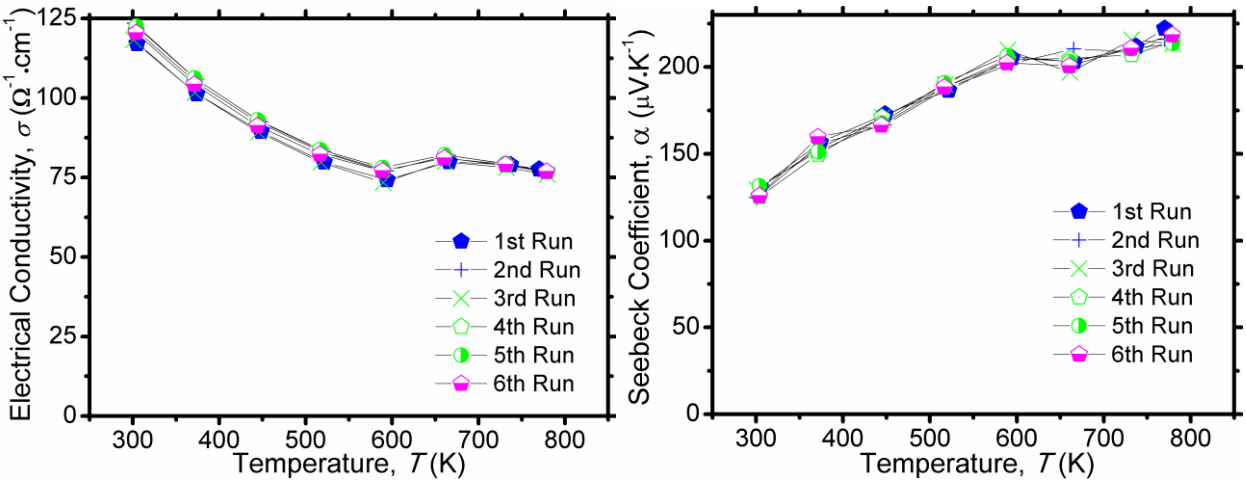

Figure 6-7 Six repeat ZEM measurements for $Ba_3Cu_{16}S_8Te_3$ (σ and α) [6 runs]

However, after the repeat measurements, the bar showed a physical change between the probes used to measure voltage (2 & 3 in Figure 6-8). This suggested the material began to deteriorate during the measurement, and the elemental ratios were investigated for an area at each of the points 1, 2, 3, and 4 using EDX. The results are summarized in Table 6-2 below, and this shows higher Cu concentration at the top of the bar, point 1. This leads us to conclude that these compounds are not stable under measurement conditions, which makes them less than ideal for TE application.

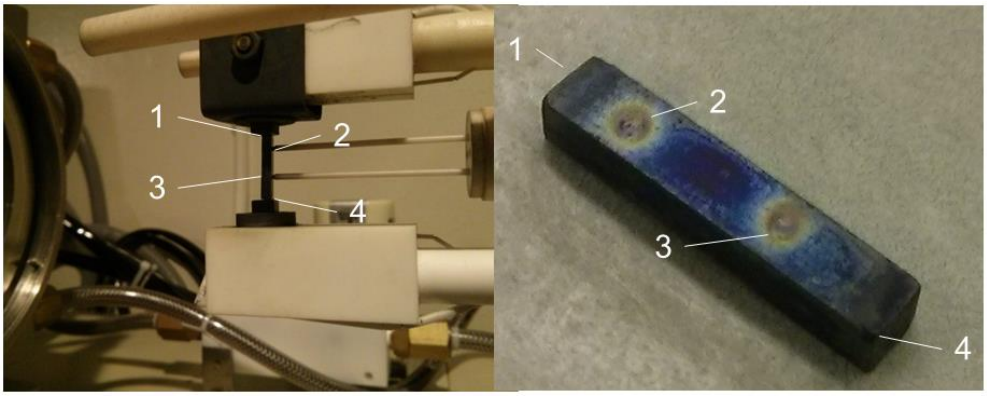

Figure 6-8 The $Ba_3Cu_{16}S_8Te_3$ bar used for ZEM measurements, points of contact highlighted (1: top, 4: bottom)

Table 6-2 Element ratio from EDX analysis performed on spots highlighted in Figure 6-8

Atom%	Ba	Cu	S	Te
1	0.4	99.6	0	0
2	13.5	65.6	8.9	11.9
3	12.7	37.9	33.4	16.1
4	10.0	50.6	29.9	9.5
Expected	10.1	52.9	26.9	10.1

6.4 Conclusion

The thermoelectric properties of the barium copper chalcogenides, $Ba_3Cu_{16-x}S_{11-y}Te_y$, were presented, and the stability of $Ba_3Cu_{16}S_8Te_3$ was tested over multiple measurements. The maximum zT achieved is for the $Ba_3Cu_{15.1}S_8Te_3$ sample, which amounts to 0.78 at ~780 K. After six electrical transport measurements, the $Ba_3Cu_{16}S_8Te_3$ bar showed a change in color between measurement probes. Higher Cu concentration at the colder side of the bar was identified via EDX analysis, and this suggests the migration of Cu through 3-D network found in the structure, which makes this material a poor choice for thermoelectric application.

7 $BaCu_{6-x}(S,Se)Te_6$

7.1 Introduction

Thermoelectric materials can convert waste heat into electricity, and are thus of increasing importance in today's society, given the growing need for alternative energy sources. Many advanced thermoelectric materials are based on narrow gap semiconductors formed by heavily doped heavy metal chalcogenides including thallium, bismuth, and lead tellurides.[2,21,75,81,82,94] The heavy metal atoms from the 6th period Tl, Bi and Pb contribute to low thermal conductivity, κ, an important criterion for thermoelectrics: increasing the thermoelectric figure-of-merit, zT, occurs with increasing efficiency, and zT is inversely proportional to κ. Other important criteria are a high Seebeck coefficient, α, and high electrical conductivity, σ, according to the definition of $zT = T\alpha^2\sigma\kappa^{-1}$ (with T = absolute temperature).

Another way to achieve low thermal conductivity may lie in cation mobility, such as mobile copper ions. This was demonstrated in case of $Cu_{2-x}Se$, which exhibits very low thermal conductivity, culminating in a high zT value of 1.5 at 1000 K.[20] The Cu ion conductivity, on the other hand, causes well-documented stability issues, inhibiting the use of this material in actual thermoelectric devices, as the ions move with the temperature gradient.[50] We have been investigating new barium copper chalcogenides for several years, aiming to find materials with localized Cu ion conductivity, where the 6th period barium ions would impede the Cu paths as well as contribute to low thermal conductivity. This research led to the discovery of several new *p*-type semiconducting materials, including $Ba_3Cu_{14-x}Te_{12}$,[95] $Ba_{6.76}Cu_{2.42}Te_{14}$,[96] $Ba_2Cu_{4-x}Te_5$ and $Ba_2Cu_{4-x}Se_yTe_{5-y}$,[97] $Ba_2Cu_{6-x}STe_4$ and $Ba_2Cu_{6-x}Se_yTe_{5-y}$,[98] $BaCu_{6-x}STe_6$ and $BaCu_{6-x}Se_{1-y}Te_{6+y}$,[52] and $Ba_3Cu_{17-x}Se_{11-y}Te_y$.[53] One and three-dimensional metallic properties were found in Ba_2Cu_{7-}

$_x$Te$_6$[99] and Ba$_3$Cu$_{17-x}$S$_{11.5-y}$Te$_y$,[51] respectively. All of these materials exhibit Cu clusters (with Cu–Cu bonds) as well as Cu atom deficiencies (hence the *p*-type character).[100] In most cases, the Cu atom network is infinite in at least one direction, possibly leading to infinite diffusion paths of the Cu atoms. Notable exceptions are Ba$_{6.76}$Cu$_{2.42}$Te$_{14}$, and BaCu$_{6-x}$STe$_6$ and BaCu$_{6-x}$Se$_{1-y}$Te$_{6+y}$, with the first exhibiting very low electrical conductivity because of its high barium content. With this contribution, we present the thermoelectric properties of BaCu$_{6-x}$STe$_6$ and BaCu$_{6-x}$Se$_{1-y}$Te$_{6+y}$.

7.2 Experimental

7.2.1Synthesis and Analysis

The title compounds were synthesized from the constituent elements stored in an argon-filled glove box (Ba pieces: 99.7%, Strem Chemicals; Cu powder: 99.5%, Alfa Aesar; S flakes: 99.98%, Aldrich; Se pellets: 99.9%, Alfa Aesar; Te broken ingots: 99.99%, Strem Chemicals). The surface of the barium pieces was scraped off to reduce contamination with oxygen. Three samples were prepared, namely one BaCu$_{5.9}$STe$_6$ and two BaCu$_{5.9}$SeTe$_6$ samples, because according to our earlier experiments, we can only obtain phase-pure samples with 5.9 Cu atoms per formula unit. The elements were loaded in the desired stoichiometric 1 : 5.9 : 1 : 6 ratios into carbon-coated silica tubes, which were then evacuated up to ~10^{-3} mbar. The silica tubes were then sealed with a hydrogen-oxygen flame, and then placed into a programmable resistance furnace for the heat treatment. The furnace was programmed to reach 773 K within 24 hours, followed by cooling down to 673 K over 200 hours, and finally down to room temperature by turning off

the heating. Cooling slowly through the 773 K - 673 K range led to incomplete crystallizing of the target materials, as the melting point of $BaCu_{5.9}SeTe_6$ is an incongruent one at 718 K, as determined by a DSC measurement.[52] Thus these samples were ground and then annealed at 663 K for 240 hours to achieve homogeneity. After the annealing step, the samples were phase pure according to their powder patterns obtained from the ground samples on an Inel powder diffractometer, which is equipped with a position-sensitive detector and utilizes Cu-$K_{\alpha 1}$ radiation.

The three pure samples were hot-pressed into round disk pellets with a diameter of 12.7 mm and a thickness of ~2 mm under a flow of argon in a graphite die using the FR-210-30T hot press (Oxy-Gon Industries). The optimized pressing conditions for the Se-containing compound were 47 MPa at 628 K for 1.5 hours, while the S-containing compound required slightly higher pressure and temperature, namely 54 MPa and 653 K, to reach a comparable density. The densities for the pressed pellets were determined via the Archimedes method, which yielded >97% of the theoretical maximal values in all cases presented here.

The purities after the property measurements were confirmed via powder X-ray diffraction as well. No changes were found in the patterns after hot-pressing and after the final property measurements, indicative of sufficient stability of these chalcogenides under those conditions. With the exceptions of a few minor, highlighted peaks (Figure 7-1), all identified peaks belonged to the target compound.

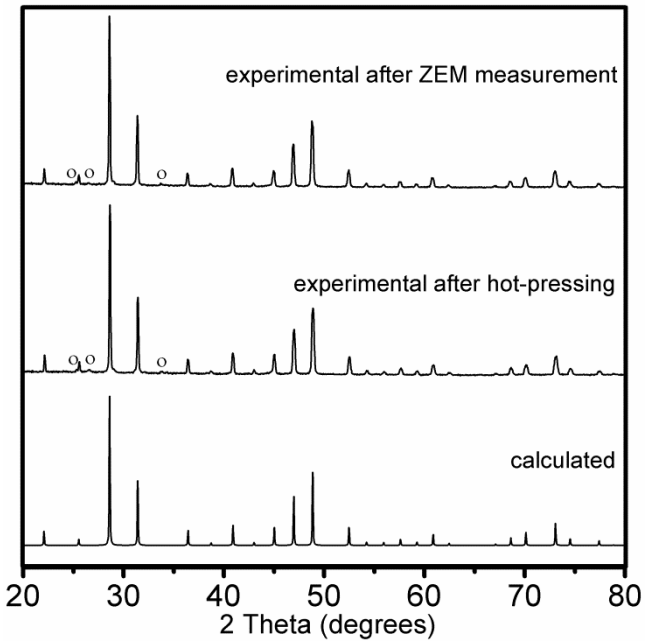

Figure 7-1 Experimental (top and center) and calculated (bottom) powder diagrams of $BaCu_{5.9}SeTe_6$.

Energy dispersive X-ray spectroscopy (EDX) was performed on selected spots of the pellet surfaces of the S and the first Se sample using the Zeiss Ultra SEM and EDAX Team software. The acceleration voltage was 25 kV under high dynamic vacuum, and the ratios of elements were determined from the observed spectrum. The ratios of the elements were consistent in both samples and reasonably close to the expected values. The Ba : Cu : Se : Te ratio for the first Se-containing sample was 8 : 42 : 5 : 45 in atomic-%, while the Ba : Cu : S : Te ratio for the S-containing sample was 9 : 44 : 8 : 41. Both compare reasonably well to the expected at-% of 7.2 : 42.4 : 7.2 : 43.2, considering that concentrations below 10% are difficult to quantify with this method. No impurities from the reaction container (C, Si, or O) were detected. EDX mapping, which shows the elemental distribution across the scanned area of the sample with different colors assigned to different elements, was done on a Se-containing pellet to confirm

homogeneity (Figure 7-2), with the top left part (labeled SEI) displaying the secondary electron image.

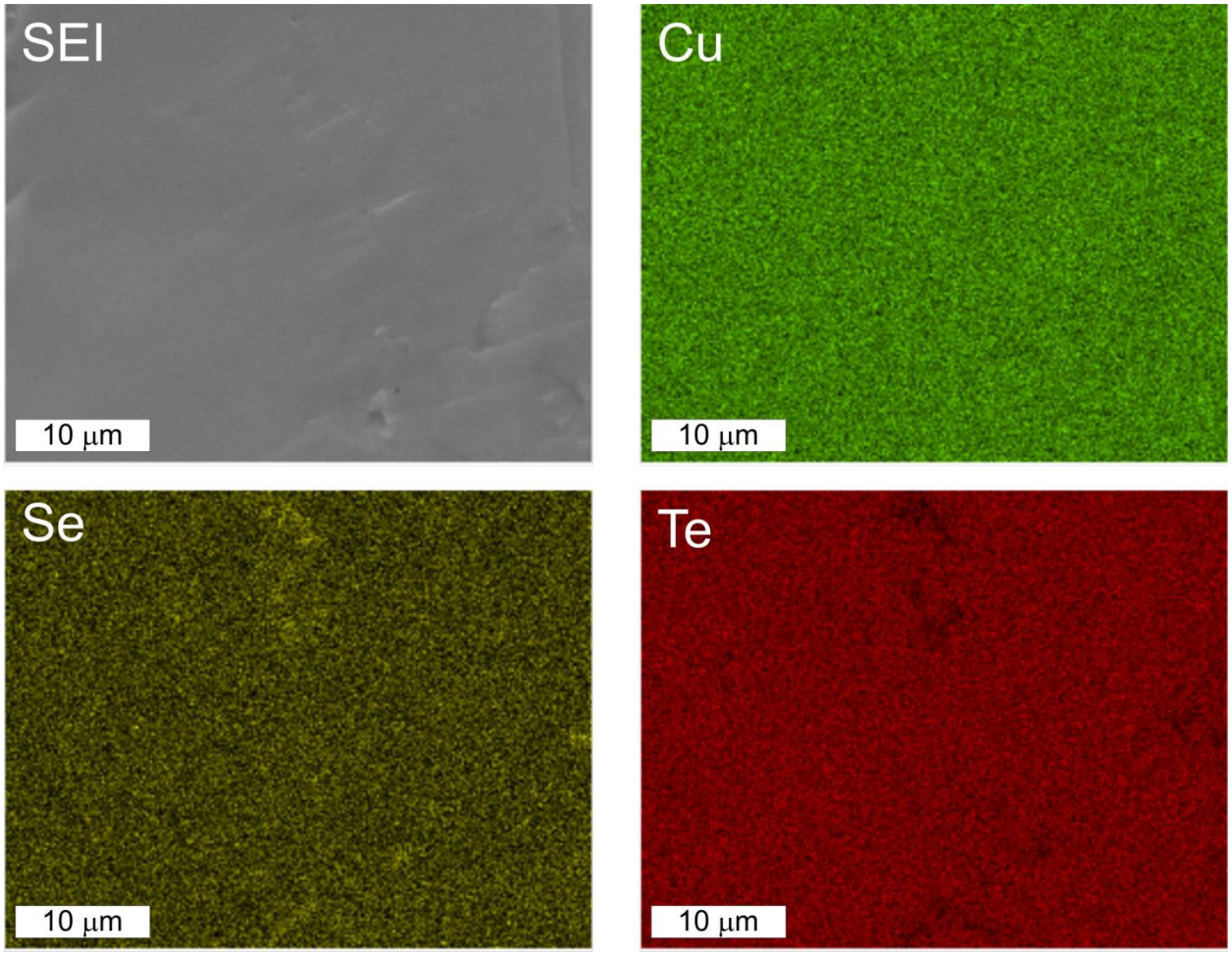

Figure 7-2 EDX maps of a $BaCu_{5.9}SeTe_6$ pellet. Top left: secondary electron image, SEI; top right: Cu map; bottom left: Se; bottom right: Te.

7.2.2Physical Property Measurements

The pellets produced via hot-pressing were polished using 1000 grit sandpaper and spray-coated with carbon in preparation for the thermal diffusivity, D, measurements up to 620 K using the Anter Flashline 3000 (now TA Instruments) , which utilizes a flash method under a

flow of argon. Thermal conductivity, κ, was calculated via $\kappa = D\rho C_{\mathrm{p}}$, where ρ is the experimentally determined density, D the measured diffusivity, and C_{p} the specific heat capacity estimated as the Dulong-Petit limit for each compound. The Dulong-Petit limit serves as a good approximation due to the lack of reliable experimental heat capacity data.[76]

For the electrical transport measurements, rectangular pellets, with dimensions of approximately 10 x 2 x 2 mm, were cut out of the disks previously used. The Seebeck coefficient, α, and the electrical conductivity, σ, were measured under helium as a function of temperature up to 620 K by a four-probe method, using the ULVAC-RIKO ZEM-3.[80] The measurements were repeated on the same pellets to check for stability of both materials, $BaCu_{5.9}STe_6$ and $BaCu_{5.9}SeTe_6$, and the results can be found in the appendix. Finally, the materials were ground after the ZEM measurements, and their X-ray patterns determined (see discussion above, and Figure 7-1).

7.3 Discussion

7.3.1 Crystal Structure

The unit cells of these isostructural polychalcogenides are surprisingly small, considering the complex formula containing four different elements, in particular in comparison with the other barium copper chalcogenides.[100] Only one formula unit occurs per cubic unit cell, with a lattice parameter of the order of *a* = 6.9 Å. The Cu atoms, located on Wyckoff position 8*i*, form a cube centered around the S or Se atom located in the origin (1*a*). The Te atoms (6*f*) cap the edges of the Cu cubes, and form Te_2^{2-} dumbbells. The Ba atom (1*b*) is placed in the center of the unit cell, and is thus surrounded by a Cu_8Te_{12} pentagonal dodecahedron.

The Cu site is statistically occupied to 5.9/8 = 74% in $BaCu_{5.9}SeTe_6$; roughly two Cu atoms are missing per unit cell (or cube). With direct Cu–Cu contacts of 2.7 Å - 2.8 Å within the cube, the Cu atoms are likely locally mobile within each cube. The path from cube to cube, on the other hand, is obstructed by the Ba and Te atoms. This is demonstrated in Figure 7-3, wherein two Cu atoms per cube are shown in a lighter color to demonstrate possible positions of the vacancies. Therefore, the Cu atoms cannot move throughout the crystal, and thus do not cause a deterioration of the properties during cycling (as far as determined).

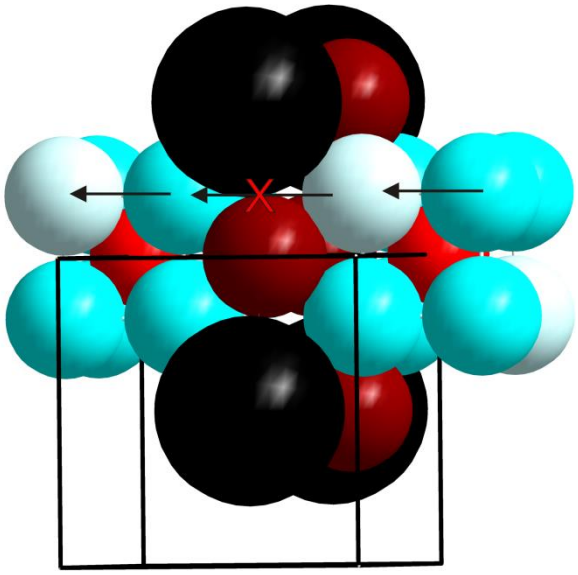

Figure 7-3 Part of the $BaCu_{5.9}SeTe_6$ unit cell. Large, black: Ba; blue: Cu; bright red: Se; dark red: Te. Bright blue: Cu vacancies. The atoms are scaled according to their Slater radii.

These materials would be intrinsic semiconductors with six Cu atoms per unit cell, according to the formula $(Ba^{2+})(Cu^{+})_6Se^{2-}(Te_2^{2-})_3$, as confirmed via DFT calculations.[52] We have not been able to synthesize such a compound; the highest amount of Cu per cell experimentally obtained was

5.93(2). The material should be an extrinsic *p*-type semiconductor with 5.9 Cu atoms per cell, nominally with 3×10^{20} carriers per cm^3 if no other defects were present.

7.3.2Physical Properties

Two different samples of equivalent stoichiometry, called $BaCu_{5.9}SeTe_6$ - I and $BaCu_{5.9}SeTe_6$ - II, as well as one $BaCu_{5.9}STe_6$ sample were characterized. The electrical conductivity data are indicative of extrinsic semiconductors, as the conductivity, σ, decreases at first with increasing temperature, and then begins to increase, once the intrinsic carriers have enough energy to cross the band gap. This turnaround in σ happens around 500 K in all three samples (Figure 7-4).

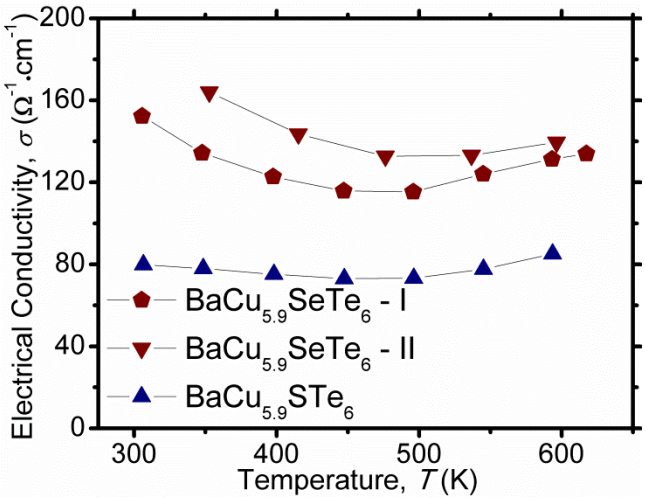

Figure 7-4 Electrical conductivity of $BaCu_{5.9}STe_6$ and $BaCu_{5.9}SeTe_6$.

The selenide sample II exhibits slightly larger σ values than sample I, while the sulfide exhibits much lower values, for example 78 $\Omega^{-1}cm^{-1}$ compared to the 133 $\Omega^{-1}cm^{-1}$ of selenide sample I and 164 $\Omega^{-1}cm^{-1}$ of selenide sample II around 350 K. With estimated experimental errors of 5%, the differences are significant. The lower conductivity of the sulfide may be a consequence of

its more ionic character, which decreases mobility. The fact that the two selenide samples are slightly different, is likely a consequence of minor weighing errors, which impact the carrier concentration. These numbers, summarized in Table 7-1, are relatively low for advanced thermoelectric materials. For example, β-Cu_2Se shows σ = 540 $\Omega^{-1}cm^{-1}$ at 420 K, and continuously decreases throughout the analyzed temperature range, down to 320 $\Omega^{-1}cm^{-1}$ at 600 K and 130 $\Omega^{-1}cm^{-1}$ at 1000 K.[20]

Table 7-1 Thermoelectric properties of $BaCu_{5.9}STe_6$ and $BaCu_{5.9}SeTe_6$. The power factor was calculated via *P.F.* = $\alpha^2\sigma$ The Lorenz number, L, was calculated from the Seebeck coefficient, α, and used to derive the lattice thermal conductivity, κ_L, from the total thermal conductivity κ via $\kappa_L = \kappa - L\sigma T$. Finally, the figure-of-merit, zT, was calculated via $zT = T\alpha^2\sigma\kappa^{-1}$.

property	**$BaCu_{5.9}STe_6$**	**$BaCu_{5.9}SeTe_6$ - I**	**$BaCu_{5.9}SeTe_6$ - II**
T	350 K \ 560 K	350 K \ 560 K	350 K \ 560 K
σ [$\Omega^{-1}cm^{-1}$]	78 \ 80	133 \ 126	164 \ 136
α [$\mu V \cdot K^{-1}$]	223 \ 201	201 \ 216	190 \ 228
P.F. [$\mu W \cdot cm^{-1}K^{-2}$]	3.9 \ 3.2	5.4 \ 5.9	5.9 \ 7.0
L [10^{-8} V^2 K^{-2}]	1.59 \ 1.62	1.62 \ 1.60	1.64 \ 1.58
κ [$W \cdot m^{-1}K^{-1}$]	0.58 \ 0.37	0.64 \ 0.51	0.67 \ 0.56
κ_L [$W \cdot m^{-1}K^{-1}$]	0.53 \ 0.30	0.57 \ 0.39	0.58 \ 0.44
zT	0.24 \ 0.49	0.30 \ 0.65	0.31 \ 0.70

The temperature dependence of the Seebeck coefficient, α, is presented in Figure 7-5. All curves are rather flat, with comparable α values of the order of 175 $\mu V \cdot K^{-1}$ - 230 $\mu V \cdot K^{-1}$. Some of these values are equivalent within the estimated experimental error of 3%. For comparison,

α increases steadily in case of β-Cu_2Se from 110 μV·K^{-1} at 420 K to 170 μV·K^{-1} at 600 K and 300 μV·K^{-1} at 1000 K.[20] In case of a clear maximum, as found in the sulfide-telluride, one can use the band gap, E_{gap}, approximation popularized by Goldsmid from the maximum α and the corresponding temperature via $E_{gap} = 2e\alpha_{max}T_{max}$, with e = electron charge.[89] Using α_{max} = 223 μV·K^{-1} and its T_{max} = 349 K, we calculate E_{gap} = 0.16 eV for the sulfide. With α_{max} = 223 μV·K^{-1} and T_{max} = 447 K, one obtains E_{gap} = 0.20 eV for selenide I, and with 228 μV·K^{-1} and 447 K, E_{gap} = 0.24 eV (selenide II). Because of the broad maxima in the case of the selenides, these values are less reliable, but are in the same range as the sulfide, and in line with the results of the electronic structure calculations.

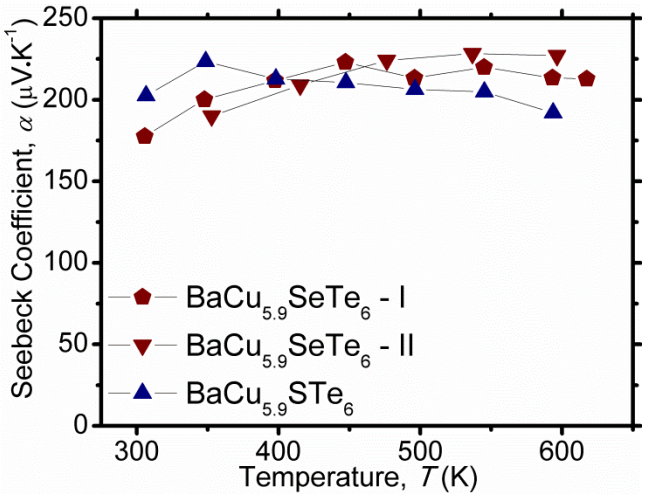

Figure 7-5 Seebeck coefficient of $BaCu_{5.9}STe_6$ and $BaCu_{5.9}SeTe_6$.

The nominator of the thermoelectric figure-of-merit, the power factor, *P.F.* = $\alpha^2\sigma$, serves as a measure of the electrical performance of thermoelectric materials. As depicted in Figure 7-6, the power factor decreases above 350 K in case of the sulfide-telluride, with values from 3.9 μW·$cm^{-1}K^{-1}$ down to 3.1 μW·$cm^{-1}K^{-1}$ at 590 K, whereas the *P.F.* generally increases with

increasing temperature in case of the selenide, e.g. from 4.8 $\mu W \cdot cm^{-1}K^{-1}$ at 300 K up to 6.1 $\mu W \cdot cm^{-1}K^{-1}$ at 617 K. The latter trend is also present in β-Cu_2Se, with the *P.F.* increasing from 6.7 $\mu W \cdot cm^{-1}K^{-1}$ at 420 K to 9.2 $\mu W \cdot cm^{-1}K^{-1}$ at 600 K (and 11.5 $\mu W \cdot cm^{-1}K^{-1}$ at 1000 K).[20] Thus, the electrical performance of β-Cu_2Se is superior compared to $BaCu_{5.9}SeTe_6$, with the sulfide-telluride being a distant third.

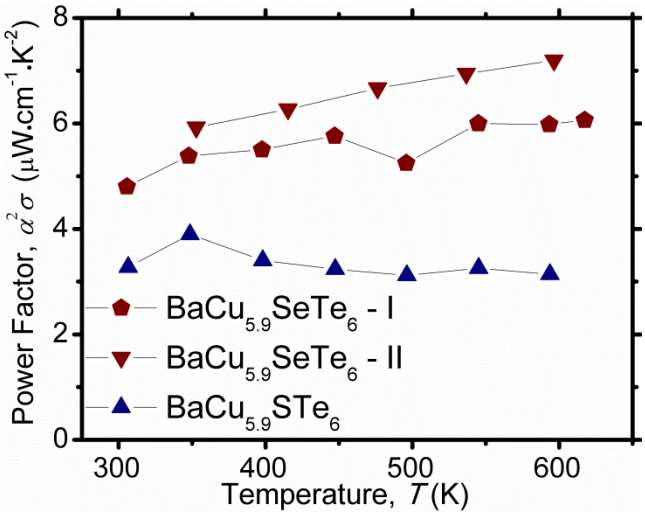

Figure 7-6 Power factor of $BaCu_{5.9}STe_6$ and $BaCu_{5.9}SeTe_6$.

The thermal conductivity, κ, data of the title compounds are presented in Figure 7-7. Overall, the values are very low, consistently below 0.8 $W \cdot m^{-1}K^{-1}$, which is even lower than for β-Cu_2Se (1.04 $W \cdot m^{-1}K^{-1}$ at 420 K; 0.98 $W \cdot m^{-1}K^{-1}$ at 600 K).[20] All values decrease with increasing temperature because of the increase in phonon-phonon scattering, the sulfide exhibiting the lowest values running from 0.62 $W \cdot m^{-1}K^{-1}$ at 330 K to 0.35 $W\ m^{-1}K^{-1}$ at 580 K, and the selenide II exhibiting the highest values, namely from 0.75 $W \cdot m^{-1}K^{-1}$ at 320 K to 0.56 $W \cdot m^{-1}K^{-1}$ at 560 K. With an estimated error of 5%, the selenide I has slightly lower values, e.g. at 320 K 0.66 $W \cdot m^{-1}K^{-1}$ ($\pm$0.03 $W\ m^{-1}K^{-1}$).

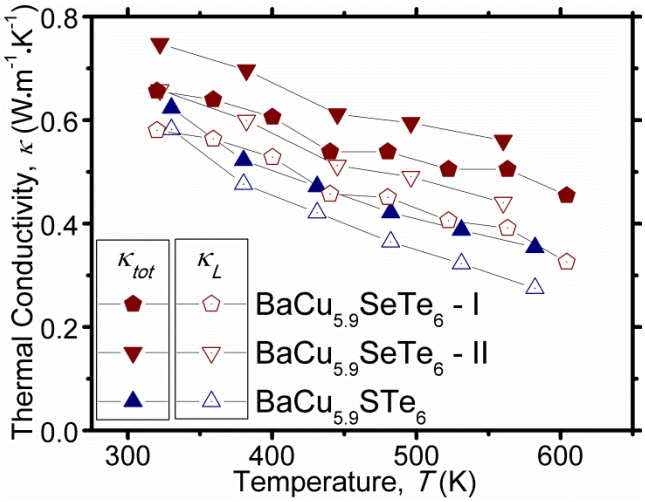

Figure 7-7 Thermal conductivity of $BaCu_{5.9}STe_6$ and $BaCu_{5.9}SeTe_6$. Filled symbols: total thermal conductivity, κ_{tot}; open symbols: lattice thermal conductivity, κ_L.

To analyze whether or not the differences in κ are simply a consequence of the different carrier concentrations, we utilized the Wiedemann-Franz law to estimate the electronic contribution $\kappa_e = L\sigma T$ to the total thermal conductivity. The Lorenz number, L, depends on the material and the temperature, and is typically between 2.44×10^{-8} V^2 K^{-2} (Sommerfeld value; degenerate semiconductors) and 1.5×10^{-8} V^2 K^{-2} (intrinsic semiconductors).[77] We calculated L by utilizing the single parabolic band and elastic carrier scattering assumption from the experimental Seebeck coefficient as described before,[90] assuming acoustic phonon and/or alloying scattering (both resulting in the scattering parameter λ being 0).[91] Subtracting κ_e from the total thermal conductivity yields the lattice thermal conductivity, $\kappa_L = \kappa - \kappa_e$, presented as open symbols in Figure 7-7 and included along with the respective Lorenz numbers in Table 1. While the differences between κ_L are smaller than the differences between κ, the trends remain the same. Therefore, we conclude that the sulfide indeed exhibits the lowest lattice

thermal conductivity here, at least at elevated temperatures, likely a consequence of the larger mass fluctuations in this material. The two selenides exhibit lattice thermal conductivity values that remain equivalent within the estimated errors. In addition to the heavy atoms and the Cu mobility, the large amount of vacancies (two per formula unit and unit cell) is likely to contribute to this very low thermal conductivity as discussed for various Cu-Ga tellurides[101] and $(In_2Te_3)_x(GeTe)_{3-3x}$ samples.[102] Comparable thermal conductivity (κ < 0.8 $W \cdot m^{-1}K^{-1}$) also occurs in some thallium tellurides, where the heavy Tl atoms along with their distorted environment are a major factor for the small κ values,[21,37,94,101] and in $Yb_{14}MnSb_{11}$ with its huge, low symmetry unit cell.[103]

Finally, the thermoelectric figure-of-merit, zT, was computed from the thermal conductivity data and fits to the experimental power factor data that encompass the temperature range of the κ measurements. The data are presented up to 600 K in Figure 7-8 in comparison to β-Cu_2Se.[20] As typical for doped semiconductors, the zT values increase with increasing temperature. The two selenide-telluride samples are the best thermoelectrics here, exhibiting basically equivalent values, ranging from zT = 0.23 at 320 K to 0.81 at 600 K. The sulfide-telluride falls behind, with zT values between 0.20 at 330 K and 0.52 at 580 K, precisely matching the performance of β-Cu_2Se in this temperature range.

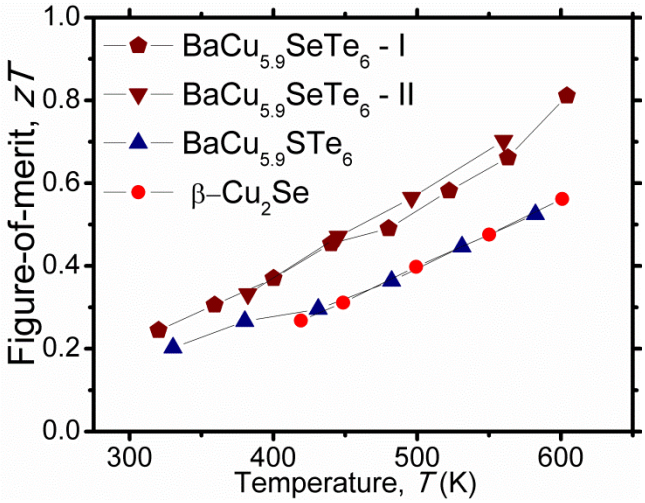

Figure 7-8 Thermoelectric figure-of-merit of $BaCu_{5.9}STe_6$ and $BaCu_{5.9}SeTe_6$ in comparison to β-Cu_2Se.

7.4 Conclusion

The thermoelectric properties of the copper chalcogenides $BaCu_{5.9}STe_6$ and $BaCu_{5.9}SeTe_6$ were presented in comparison to β-Cu_2Se, one of the leading high temperature thermoelectrics. The best feature with regards to the thermoelectric properties is the extraordinarily low thermal conductivity, which, combined with low electrical conductivity and high Seebeck coefficient, results in an outstanding thermoelectric figure-of-merit: the sulfide-telluride exhibits zT values comparable to β-Cu_2Se, while the selenide-telluride has superior properties within the investigated temperature range. On the plus side, the Ba-containing materials appear to not suffer from Cu ion migration, which reflects itself in high stability; on the other hand, these materials decompose upon heating above 720 K.

Based on the relatively high Seebeck coefficient and low electrical conductivity, increasing the charge carrier concentration via hole doping should result in higher zT values. Unfortunately we were unable to produce more Cu-deficient samples. Therefore, we will attempt to raise the hole concentration (lower the electron concentration) via alternative routes in the future, e.g. via a partial substitution of Ba^{2+} with K^+, in order to verify this assumption.

8 Conclusion

A number of compounds were successfully synthesized and hot-pressed to pellets with high relative densities, including: $Tl_4Zr_{1.03}Te_4$, Tl_4HfTe_4, $Ba_3Cu_{16}S_8Te_3$, $Ba_3Cu_{16}S_9Te_2$, $Ba_3Cu_{15.1}S_7Te_4$, $Ba_3Cu_{15.1}S_8Te_3$, $BaCu_{5.9}STe_6$, and $BaCu_{5.9}SeTe_6$. The zT values for the thallium tellurides did not show any improvement over the cold-pressed sample results, where Tl_4HfTe_4 showed the highest zT of 0.08 at ~490 K. However, a positive effect of adding Nb on the thermoelectric properties is demonstrated for the samples of nominal composition "$Tl_4ZrNb_xTe_4$" (x = 0.02, 0.04, 0.06), where higher zT was achieved after adding Nb, with a maximum zT of 0.064 at ~500 K for the "$Tl_4ZrNb_{0.04}Te_4$" sample, compared to 0.042 for the undoped one.

On the other hand, the zT values for hot-pressed barium copper chalcogenides exhibited great improvement over the previously reported cold-pressed samples. A positive effect of doping was demonstrated for $Ba_3Cu_{16}S_8Te_3$ and $Ba_3Cu_{15.1}S_8Te_3$, where $Ba_3Cu_{15.1}S_8Te_3$ showed higher electrical conductivity and greater zT than $Ba_3Cu_{16}S_8Te_3$.The $Ba_3Cu_{16-x}S_{11-y}Te_y$ samples showed a higher power factor for hot-pressed samples, resulting in a higher zT, and a value of 0.78 at ~780 K was achieved for $Ba_3Cu_{15.1}S_8Te_3$. Unfortunately, physical changes of these materials became apparent after repeat measurements, likely due to the migration of Cu ions through 3-D Cu-network in these compounds. The migration of Cu was further investigated and confirmed using EDX measurements, which showed higher Cu concentration at the colder side of the bar. Finally, the thermoelectric properties of $BaCu_{5.9}STe_6$ and $BaCu_{5.9}SeTe_6$ are reported, and these samples show high zT values of 0.52 at 580 K and 0.81 at 600 K for the sulfide and selenide, respectively. These samples also show great reproducibility of property measurements, and no physical change is observed after the measurement, which makes these materials appropriate,

upon further optimization, for thermoelectric application. The zT values for various samples investigated in this report are presented in Figure 9-1 below.

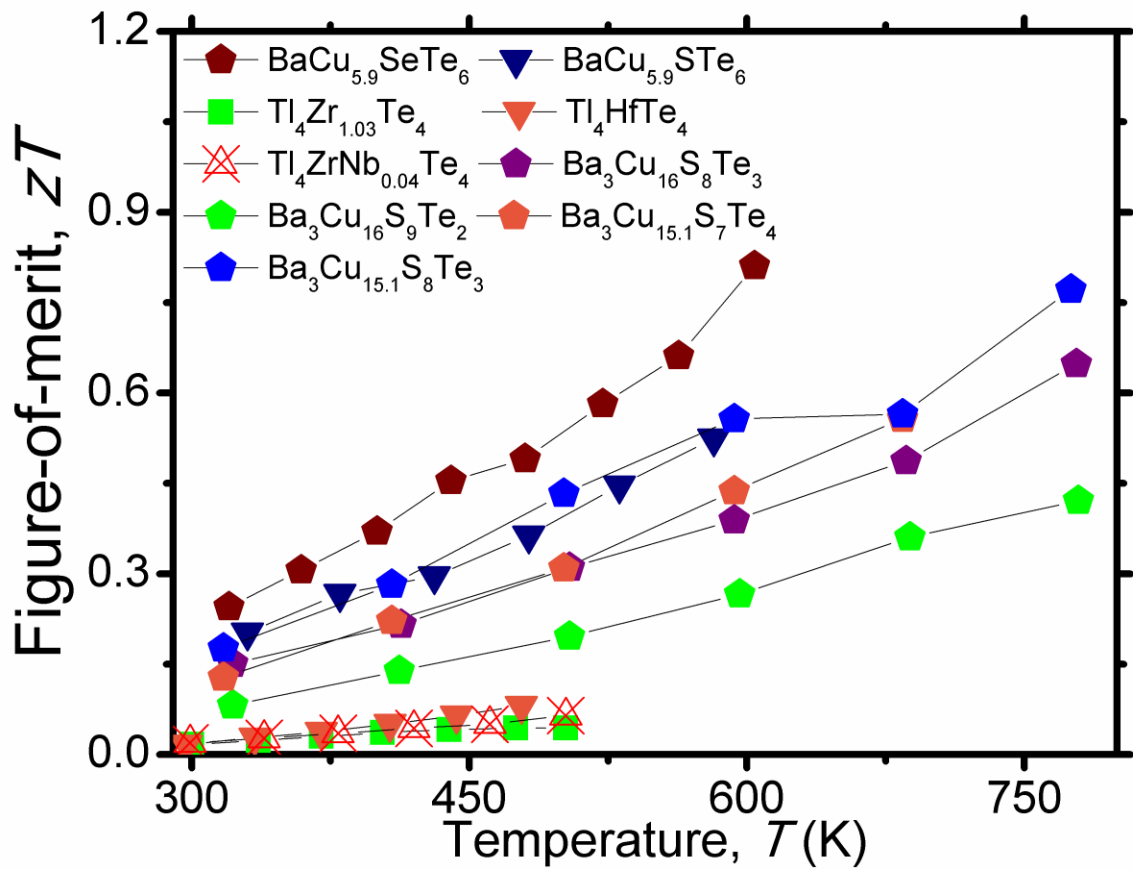

Figure 8-1 Comparison of zT for samples synthesized as part of this thesis

References

(1) Bell, L. E. *Science* **2008**, *321*, 1457.
(2) Kleinke, H. *Chem. Mater.* **2010**, *22*, 604.
(3) DiSalvo, F. J. *Science* **1999**, *285*, 703.
(4) Rowe, D. M. *CRC Handbook of Thermoelectrics*, **1995**.
(5) Peltier, J. C. *Ann. Chem.*; *LVI, 371*, **1834**.
(6) Thomson, W. *Proc. R. Soc. of Edinburgh* **1851**, *3*, 91.
(7) Nemir, D.; Beck, J. *J. Electron. Mater.* **2010**, *39*, 1897.
(8) Janardan Kundu, C. K. S., and P.S. Mallick *Semicond. Phys. Quantum Electron. Optoelectron.* **2007**, *10*, 3.
(9) Snyder, G. J.; Toberer, E. S. *Nat. Mater.* **2008**, *7*, 105.
(10) Szczech, J. R.; Higgins, J. M.; Jin, S. *J. Mater. Chem.* **2011**, *21*, 4037.
(11) Blake, N. P.; Latturner, S.; Bryan, J. D.; Stucky, G. D.; Metiu, H. *J. Chem. Phys.* **2001**, *115*, 8060.
(12) Dyck, J. S.; Chen, W.; Uher, C.; Chen, L.; Tang, X.; Hirai, T. *J. Appl. Phys.* **2002**, *91*, 3698.
(13) Skrabek, E.; Trimmer, D. *CRC Handbook of Thermoelectrics* **1995**, *275*.
(14) Slack, G. A. In *CRC Handbook of Thermoelectrics*; Rowe, D. M., Ed. **1995**, p 407.
(15) Sofo, J. O.; Mahan, G. D. *Phys. Rev. B* **1994**, *49*, 4565.
(16) Chung, D.-Y.; Hogan, T.; Brazis, P.; Rocci-Lane, M.; Kannewurf, C.; Bastea, M.; Uher, C.; Kanatzidis, M. G. *Science* **2000**, *287*, 1024.
(17) Hsu, K. F.; Loo, S.; Guo, F.; Chen, W.; Dyck, J. S.; Uher, C.; Hogan, T.; Polychroniadis, E. K.; Kanatzidis, M. G. *Science* **2004**, *303*, 818.
(18) Brown, S. R.; Kauzlarich, S. M.; Gascoin, F.; Snyder, G. J. *Chem. Mater.* **2006**, *18*, 1873.
(19) Gascoin, F.; Rasmussen, J.; Snyder, G. J. *J. Alloys Compd.* **2007**, *427*, 324.
(20) Liu, H.; Shi, X.; Xu, F.; Zhang, L.; Zhang, W.; Chen, L.; Li, Q.; Uher, C.; Day, T.; Snyder, G. J. *Nat. Mater.* **2012**, *11*, 422.
(21) Guo, Q.; Chan, M. H.; Kuropatwa, B. A.; Kleinke, H. *Chem. Mater.* **2013**, *25*, 4097.
(22) Kurosaki, K.; Kosuga, A.; Muta, H.; Uno, M.; Yamanaka, S. *Appl. Phys. Lett.* **2005**, *87*, 061919.
(23) Yan, X.; Poudel, B.; Ma, Y.; Liu, W.; Joshi, G.; Wang, H.; Lan, Y.; Wang, D.; Chen, G.; Ren, Z. *Nano Lett.* **2010**, *10*, 3373.
(24) Ravich, Y. I.; Efimova, B. A.; Smirnov, I. A. *Semiconducting Lead Chalcogenides*; Plenum Press: New York, **1970**.
(25) Christakudis, G. C.; Plachkova, S. K.; Shelimova, L. E.; Avilov, E. S. In *Eighth International Conference on Thermoelectric Energy Conversion* Nancy, France, **1989**, p 125.
(26) Chung, D.-Y.; Hogan, T. P.; Rocci-Lane, M.; Brazis, P.; Ireland, J. R.; Kannewurf, C. R.; Bastea, M.; Uher, C.; Kanatzidis, M. G. *J. Am. Chem. Soc.* **2004**, *126*, 6414.
(27) Saramat, A.; Svensson, G.; Palmqvist, A. E. C.; Stiewe, C.; Mueller, E.; Platzek, D.; Williams, S. G. K.; Rowe, D. M.; Bryan, J. D.; Stucky, G. D. *J. Appl. Phys.* **2006**, *99*, 023708.
(28) Guo, Q.; Assoud, A.; Kleinke, H. *Adv. Energy Mater.* **2014**.
(29) Sales, B. C.; Mandrus, D.; Williams, R. K. *Science* **1996**, *272*, 1325.
(30) Quarez, E.; Hsu, K.-F.; Pcionek, R.; Frangis, N.; Polychroniadis, E. K.; Kanatzidis, M. G. *J. Am. Chem. Soc.* **2005**, *127*, 9177.
(31) Poudeu, P. F. P.; D'Angelo, J.; Downey, A. D.; Short, J. L.; Hogan, T. P.; Kanatzidis, M. G. *Angew. Chem. Int. Ed.* **2006**, *45*, 3835.
(32) Androulakis, J.; Pcionek, R.; Quarez, E.; Do, J.-H.; Kong, H.; Palchik, O.; Uher, C.; D'Angelo, J. J.; Short, J.; Hogan, T.; Kanatzidis, M. G. *Chem. Mater.* **2006**, *18*, 4719.
(33) Chitroub, M.; Besse, F.; Scherrer, H. *J. Alloys Compd.* **2008**, *460*, 90.

(34) Zhu, G. H.; Lee, H.; Lan, Y. C.; Wang, X. W.; Joshi, G.; Wang, D. Z.; Yang, J.; Vashaee, D.; Guilbert, H.; Pillitteri, A.; Dresselhaus, M. S.; Chen, G.; Ren, Z. F. *Phys. Rev. Lett.* **2009**, *102*, 196803.
(35) Lu, X.; Morelli, D. T.; Xia, Y.; Zhou, F.; Ozolins, V.; Chi, H.; Zhou, X.; Uher, C. *Adv. Energy Mater.* **2013**, *3*, 342.
(36) Xu, J.; Kleinke, H. *J. Comput. Chem.* **2008**, *29*, 2134.
(37) Wölfing, B.; Kloc, C.; Teubner, J.; Bucher, E. *Phys. Rev. Lett.* **2001**, *86*, 4350.
(38) Bux, S. K.; Fleurial, J. P.; Kaner, R. B. *Chem. Commun.* **2010**, *46*, 8311.
(39) Wang, X. W.; Lee, H.; Lan, Y. C.; Zhu, G. H.; Joshi, G.; Wang, D. Z.; Yang, J.; Muto, A. J.; Tang, M. Y.; Klatsky, J.; Song, S.; Dresselhaus, M. S.; Chen, G.; Ren, Z. F. *Appl. Phys. Lett.* **2008**, *93*, 193121.
(40) Bux, S. K.; Blair, R. G.; Gogna, P. K.; Lee, H.; Chen, G.; Dresselhaus, M. S.; Kaner, R. B.; Fleurial, J.-P. *Adv. Funct. Mater.* **2009**, *19*, 2445.
(41) Pei, Y.; LaLonde, A.; Iwanaga, S.; Snyder, G. J. *Energy Environ. Sci.* **2011**, *4*, 2085.
(42) LaLonde, A. D.; Pei, Y.; Snyder, G. J. *Energy Environ. Sci.* **2011**, *4*, 2090.
(43) LaLonde, A. D.; Pei, Y.; Wang, H.; Jeffrey Snyder, G. *Mater. Today* **2011**, *14*, 526.
(44) Iversen, B. B.; Palmqvist, A. E. C.; Cox, D. E.; Nolas, G. S.; Stucky, G. D.; Blake, N. P.; Metiu, H. *J. Solid State Chem.* **2000**, *149*, 455.
(45) Braun, D. J.; Jeitschko, W. *J. Less-Common Met.* **1980**, *72*, 147.
(46) Caillat, T. F., J. P.; Borshchevsky, A. *J. Phys. Chem. Solids* **1997**, *58*, 1119.
(47) Koza, M. M.; Johnson, M. R.; Viennois, R.; Mutka, H.; Girard, L.; Ravot, D. *Nat. Mater.* **2008**, *7*, 805.
(48) Sankar, C. R.; Bangarigadu-Sanasy, S.; Assoud, A.; Kleinke, H. *J. Mater. Chem.* **2010**, *20*, 7485.
(49) Sankar, C. R.; Guch, M.; Assoud, A.; Kleinke, H. *Chem. Mater.* **2011**, *23*, 3886.
(50) Brown, D. R.; Day, T.; Caillat, T.; Snyder, G. J. *J. Electron. Mater.* **2013**, *42*, 2014.
(51) Kuropatwa, B. A.; Assoud, A.; Kleinke, H. *Inorg. Chem.* **2011**, *50*, 7831.
(52) Mayasree, O.; Sankar, C. R.; Cui, Y.; Assoud, A.; Kleinke, H. *Eur. J. Inorg. Chem.* **2011**, *2011*, 4037.
(53) Kuropatwa, B.; Cui, Y.; Assoud, A.; Kleinke, H. *Chem. Mater.* **2009**, *21*, 88.
(54) Giacovazzo, C. *Fundamentals of Crystallography*; Second ed.; Oxford University Press: Oxford, **1992**.
(55) Stout, G. H.; Jensen, L. H. *X-Ray Structure Determination*; Second ed.; Wiley & Sons: New York, **1989**.
(56) Albright, T. A.; Burdett, J. K.; Whangbo, M. H. *Orbital Interactions in Chemistry*; Wiley & Sons: New York, **1984**.
(57) Hoffman, R. *Solids and Surfaces: a Chemist's View of Bonding in Extended Strctures*; VCH, **1988**.
(58) Kuropatwa, B. A., University of Waterloo, **2012**.
(59) Huheey, J. E.; Keiter, E. A.; Keiter, R. L. *Inorganic Chemistry: Principles of Structure and Reactivity*; Fourth ed.; HarperCollins College Publishers: New York, **1993**.
(60) Kittel, C. *Introduction to Solid State Physics*; Wiley & Sons: New York, **1971**.
(61) Hoffmann, R. *Angew. Chem. Int. Ed. Engl.* **1987**, *26*, 846.
(62) Williams, J. M. *Adv. Inorg. Chem. Radiochem.* **1983**, *26*, 235.
(63) Dronskowski, R.; Blöchl, P. E. *J. Phys. Chem.* **1993**, *97*, 8617.
(64) Institute of Inorganic Chemistry Aachen University of Technology; Vol. 2011.
(65) Heremans, J. P.; Jovovic, V.; Toberer, E. S.; Saramat, A.; Kurosaki, K.; Charoenphakdee, A.; Yamanaka, S.; Snyder, G. J. *Science* **2008**, *321*, 554.
(66) Pamplin, B. R. *Crystal Growth*; Pergamon, **1980**.
(67) Merkle, R.; Maier, J. *Z. Anorg. Allg. Chem.* **2005**, *631*, 1163.
(68) West, A. R. *Solid Sate Chemistry and its Applications*; Wiley & Sons: New York, **1984**.

(69) Pecharsky, V. K.; Zavalij, P. Y. *Fundamentals of Powder Diffraction and Structural Characterization of Materials*; 2nd ed.; Springer: New York, **2009**.
(70) Watson, E. S.; O'Neil, M. J.; Co., P.-E., Ed. United States of America, **1962**; Vol. 3,263,484.
(71) *Differential Thermal Analysis*; Mackenzie, R. C., Ed.; Academic Press Inc.: London and New York, **1970**; Vol. 1.
(72) Blumm, J. In *Ceramic Industry* Selb/Bavaria, Germany, **2005**; Vol. 2011.
(73) Group, N. *STA 409 PC Luxx User Manual* Selb, Germany, **1998**.
(74) Höhne, G.; Hemminger, W.; Flammersheim, H.-J. *Differential Scanning Calorimetry: An Introduction for Practitioners*; Springer: Berlin Heidelberg, **1996**.
(75) Rowe, D. M. *Thermoelectrics Handbook: Macro to Nano*; CRC Press, Taylor & Francis Group: Boca Raton, FL, USA, **2006**.
(76) Wang, H.; Porter, W. D.; Böttner, H.; König, J.; Chen, L.; Bai, S.; Tritt, T. M.; Mayolet, A.; Senawiratne, J.; Smith, C.; Harris, F.; Gilbert, P.; Sharp, J.; Lo, J.; Kleinke, H.; Kiss, L. *J. Electron. Mater.* **2013**, *42*, 1073.
(77) Kumar, G. S.; Prasad, G.; Pohl, R. O. *J. Mater. Sci.* **1993**, *28*, 4261.
(78) Pei, Y.; LaLonde, A. D.; Wang, H.; Snyder, G. J. *Energ. Environ. Sci.* **2012**, *5*, 7963.
(79) May, A. F.; Toberer, E. S.; Saramat, A.; Snyder, G. J. *Phys. Rev. B* **2009**, *80*, 125205.
(80) Wang, H.; Porter, W. D.; Böttner, H.; König, J.; Chen, L.; Bai, S.; Tritt, T. M.; Mayolet, A.; Senawiratne, J.; Smith, C.; Harris, F.; Gilbert, P.; Sharp, J. W.; Lo, J.; Kleinke, H.; Kiss, L. *J. Electron. Mater.* **2013**, *42*, 654.
(81) Toberer, E. S.; May, A. F.; Snyder, G. J. *Chem. Mater.* **2010**, *22*, 624.
(82) Kanatzidis, M. G. *Chem. Mater.* **2010**, *22*, 648.
(83) Biswas, K.; He, J.; Blum, I. D.; Wu, C.-I.; Hogan, T. P.; Seidman, D. N.; Dravid, V. P.; Kanatzidis, M. G. *Nature* **2012**, *489*, 414.
(84) Kuropatwa, B. A.; Assoud, A.; Kleinke, H. *J. Alloys Compd.* **2011**, *509*, 6768.
(85) Kurosaki, K.; Kosuga, A.; Yamanaka, S. *J. Alloys Compd.* **2003**, *351*, 279.
(86) Kurosaki, K.; Uneda, H.; Muta, H.; Yamanaka, S. *J. Alloys Compd.* **2004**, *376*, 43.
(87) Wang, C.; Eylem, C.; Hughbanks, T. *Inorg. Chem.* **1998**, *37*, 390.
(88) Assoud, A.; Soheilnia, N.; Kleinke, H. *J. Solid State Chem.* **2006**, *179*, 2707.
(89) Goldsmid, H. J.; Sharp, J. W. *J. Electron. Mater.* **1999**, *28*, 869.
(90) Guo, Q.; Kleinke, H. *J. Solid State Chem.* **2014**, *215*, 253.
(91) Cahill, D. G.; Watson, S. K.; Pohl, R. O. *Phys. Rev. B* **1992**, *46*, 6131.
(92) Mostofi, A. A.; Yates, J. R.; Lee, Y.-S.; Souza, I.; Vanderbilt, D.; Marzari, N. *Comput. Phys. Commun.* **2008**, *178*, 685.
(93) Situmorang, M.; Goldsmid, H. *Phys. Status Solidi B* **1986**, *134*, K83.
(94) Guo, Q.; Assoud, A.; Kleinke, H. *Adv. Energy Mater.* **2014**, *4*, 1400348.
(95) Assoud, A.; Thomas, S.; Sutherland, B.; Zhang, H.; Tritt, T. M.; Kleinke, H. *Chem. Mater.* **2006**, *18*, 3866.
(96) Cui, Y.; Assoud, A.; Xu, J.; Kleinke, H. *Inorg. Chem.* **2007**, *46*, 1215.
(97) Mayasree, O.; Cui, Y. J.; Assoud, A.; Kleinke, H. *Inorg. Chem.* **2010**, *49*, 6518.
(98) Mayasree, O.; Sankar, C. R.; Assoud, A.; Kleinke, H. *Inorg. Chem.* **2011**, *50*, 4580.
(99) Kuropatwa, B. A.; Assoud, A.; Kleinke, H. *Inorg. Chem.* **2012**, *51*, 5299.
(100) Mayasree, O.; Sankar, C. R.; Kleinke, K. M.; Kleinke, H. *Coord. Chem. Rev.* **2012**, *256*, 1377.
(101) Kurosaki, K.; Yamanaka, S. *Phys. Status Solidi* **2013**, *210*, 82.
(102) Sun, H.; Lu, X.; Chi, H.; Morelli, D. T.; Uher, C. *Phys. Chem. Chem. Phys.* **2014**, *16*, 15570.
(103) Cox, C. A.; Toberer, E. S.; Levchenko, A. A.; Brown, S. R.; Snyder, G. J.; Navrotsky, A.; Kauzlarich, S. M. *Chem. Mater.* **2009**, *21*, 1354.